

Adolphe Merkle Institute
University of Fribourg (Switzerland)

ENGINEERING METAL OXIDES FOR UV-STABLE PEROVSKITE SOLAR CELLS

THESIS

presented to the Faculty of Science of the University of Fribourg (Switzerland)
in consideration for the award of the academic grade of
Doctor rerum naturalium

by

Bart Roose

from

Terneuzen, The Netherlands

Thesis No. 2015

Uniprint

2017

Adolphe Merkle Institute
University of Fribourg (Switzerland)

**ENGINEERING METAL OXIDES FOR
UV-STABLE PEROVSKITE SOLAR CELLS**

THESIS

presented to the Faculty of Science of the University of Fribourg (Switzerland)
in consideration for the award of the academic grade of
Doctor rerum naturalium

by

Bart Roose

from

Terneuzen, The Netherlands

Thesis No. 2015

Uniprint

2017

Accepted by the Faculty of Science of the University of Fribourg (Switzerland) upon the recommendation of Dr. Pablo Docampo, Prof. Natalie Banerji, Dr. Antonio Abate, Prof. Barbara Rothen and Prof. Ullrich Steiner

Fribourg, 08.05.2017

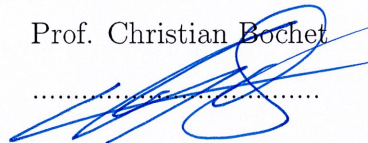
Thesis supervisor

Prof. Ullrich Steiner

.....


Dean

Prof. Christian Bochet

.....


The sun, with all those planets revolving around it and dependent on it, can still ripen a bunch of grapes as if it had nothing else in the universe to do

Galileo Galilei

Acknowledgements

This thesis is the result of work carried out in the Thin Films and Interfaces Group in Cambridge and the Soft Matter Physics Group at the Adolphe Merkle Institute in Fribourg. I would like to take the opportunity here to thank the people who have helped me making my time in Cambridge and Fribourg so tremendously rewarding.

First of all I want to thank my supervisor, Prof. Ullrich Steiner. Ulli is the best supervisor a student can wish for, always acting in the best interest of his students. He gave me the freedom to pursue my own research interest, but was never too busy to give me advice and good council when I needed it.

When I first arrived in Cambridge it was Dr. Sandeep Pathak who introduced me to the field of perovskite solar cells. Karl Gödel has been an amazing friend and colleague and I am forever grateful for all his help throughout this work. A big thanks as well to Jonathan, Raphael, Tobey and Harry for many interesting lunchtime discussions.

Moving to a new country is always difficult and I have to thank Bodo, Michi, Yuan and Manuel for the great company during the first months in Fribourg while we were getting the lab operational. As the group and institute grew I had the pleasure of meeting many more interesting people. Special thanks to Ilja, Karolina, Preston, Mirela, Sandra and Olivia for all the fun times we shared, and to everyone I got to meet in the Soft Matter Physics Group and the AMI in general. The AMI truly is a special place, enabling easy interaction between people working in different disciplines

A special thanks goes out to Dr. Antonio Abate, whose help made my work much more relevant. He taught me a great deal about conducting great science and his drive and ambition have inspired me to always strive to get the best possible out of myself and my research. Through Antonio I had the pleasure of working together with Dr. Juan-Pablo Correa-Baena and Dr. Michael Saliba, who provided many interesting ideas that helped to progress my scientific development.

I also want to thank Dr. Natalie Burrows for her patience and support during these past years, living in different countries has not been easy, but it made the time we did spend together that much more special. Lastly my family, from whom I inherited the curiosity and persistence that have culminated in this thesis, and who have always supported me in my endeavours.

List of Abbreviations

Au	gold
AZO	aluminum-doped zinc oxide
BCP	block-copolymer
CB	conduction band
DSSC	dye-sensitized solar cell
ESL	electron selective layer
ETM	electron transporting material
eV	electron volt
FF	fill factor
FTO	fluorine-doped tin oxide
FWHM	full-width at half-maximum
Ga	gallium
HTM	hole transporting material
IMPS	intensity modulated photocurrent spectroscopy
IMVS	intensity modulated photovoltage spectroscopy
IPCE	incident photon-to-current efficiency
J_{sc}	short circuit current
MPPT	maximum power point tracking
Nd	neodymium
PCE	power conversion efficiency
PDS	photothermal deflection spectroscopy
PSC	perovskite solar cell
SEM	scanning electron microscopy

spiro-OMeTAD	2,2',7,7'-tetrakis (<i>N,N</i> -di- <i>p</i> -methoxyphenyl-amine)-9,9'-spirobifluorene
SnO ₂	tin dioxide
TCO	transparent conducting oxide
TCSPC	time-correlated single-photon counting
TiO ₂	titanium dioxide
UV	ultraviolet
VB	valence band
V _{FB}	flat-band potential
V _{OC}	open circuit potential
XPS	X-ray photoelectron spectroscopy
XRD	X-ray diffraction

Zusammenfassung

Metalloxiden für UV-Stabile Perowskit-Solarzellen

Bart Roose

Diese Arbeit untersucht die Anwendung von Metalloxiden als Elektronentransportmaterial in Perowskit-Solarzellen. Die zentrale Forschungsfrage ist, wie Metalloxide die Stabilität von Perowskit-Solarzellen beeinflussen und wie Metalloxide, beispielsweise durch gezielte Dotierung, modifiziert werden können, um die Stabilität von Solarzellen zu verbessern.

*Die Arbeit beginnt mit vier einleitenden Hintergrundkapiteln. **Kapitel 1** erklärt die zunehmende Notwendigkeit von Solarenergie und den Beitrag von Perowskit-Solarzellen zu einer sauberen Energiezukunft. **Kapitel 2** stellt die Arbeitsprinzipien von Solarzellen vor, während **Kapitel 3** mehr Details über die Geschichte und den Aufbau von Perowskit-Solarzellen enthält. **Kapitel 4** leitet insbesondere das Konzept der Nanostrukturierung von Metalloxiden unter Verwendung einer Blockcopolymerschablone ein. Die für diese Arbeit benutzten experimentellen Methoden werden ausführlich in **Kapitel 5** beschrieben.*

*Diese einleitenden Kapitel dienen als Grundlage für die vier experimentellen Hauptkapitel dieser Arbeit. **Kapitel 6** beschreibt die Verwendung von Neodym-dotiertem TiO_2 in Perowskit-Solarzellen und den Einfluss der Dotierung auf den Wirkungsgrad. **Kapitel 7** und **Kapitel 8** zielen darauf ab den Wirkungsgrad SnO_2 -basierter Perowskit-Solarzellen zu steigern, indem einerseits ein neuartiges Elektrodenmaterial verwendet wird und andererseits SnO_2 mit Gallium dotiert wird. **Kapitel 9** beschreibt die spontane Koaleszenz von kollidalen Perowskit-Kristallen, eine der außergewöhnlichen Eigenschaften von Perowskitmaterialien.*

Summary

Engineering Metal Oxides for UV-Stable Perovskite Solar Cells

Bart Roose

This thesis is a study of the role of the metal oxide electron transporting material in perovskite solar cells. The central research question is how the metal oxide influences the stability of perovskite solar cells and how the metal oxide can be modified to improve the stability.

*The thesis begins by providing four background chapters. **Chapter 1** explains the need for solar energy and what perovskite solar cells can contribute to a clean energy future. **Chapter 2** covers the working principles of solar cells, whereas **Chapter 3** provides more detail about the history and architecture of the perovskite solar cell. **Chapter 4** introduces the concept of nanostructuring metal oxides, using a block-copolymer template. The key experimental techniques and methods used throughout this work are described in **Chapter 5**.*

*These introductory sections serve as the foundation for the four major experimental chapters of the thesis. **Chapter 6** reports on the use of neodymium doped TiO_2 in perovskite solar cells. **Chapter 7** and **Chapter 8** aim to increase the efficiency of SnO_2 based perovskite solar cells, by making use of a novel electrode material and doping SnO_2 with gallium. **Chapter 9** covers the spontaneous coalescence of perovskite crystals, highlighting the extraordinary properties of perovskites.*

Contents

Acknowledgements	ii
List of Abbreviations	iv
Summary	vi
1 Introduction	1
2 Fundamentals of Solar Cells	5
3 Perovskite Solar Cells	13
3.1 Introduction	13
3.2 Architecture of perovskite solar cells	18
3.3 Material properties	23
3.3.1 TiO ₂	23
3.3.2 SnO ₂	29
4 Block-copolymer templated metal-oxides	31
4.1 Block-copolymer self-assembly	31
4.2 Sol-gel chemistry	35
4.3 Combining BCP self-assembly and sol-gel chemistry	37
5 Experimental techniques and methods	41
5.1 Morphological characterisation	41
5.1.1 Scanning electron microscopy	41
5.1.2 X-ray diffraction	42
5.1.3 Cyclic voltammetry	43

Contents

5.2	Material characterisation	45
5.2.1	X-ray photoelectron spectroscopy	45
5.2.2	UV/Vis spectroscopy	46
5.2.3	Photothermal deflection spectroscopy	46
5.2.4	Mott-Schottky analysis	47
5.2.5	Time-correlated single-photon counting	49
5.3	Solar cell fabrication	51
5.3.1	Perovskite solar cell device assembly	51
5.3.2	Dye sensitized solar cell device assembly	54
5.4	Solar cell characterisation	55
5.4.1	Current-Voltage characteristics	55
5.4.2	Incident photon-to-current efficiency	55
5.4.3	Intensity Modulated Photocurrent Spectroscopy	56
5.4.4	Intensity Modulated Photovoltage Spectroscopy	57
5.4.5	Charge extraction	58
6	Neodymium doping of m-TiO₂ in perovskite solar cells	59
6.1	Introduction	59
6.2	Experimental methods	62
6.2.1	Material characterization	62
6.2.2	Solar cell preparation	62
6.2.3	Solar cell characterisation	62
6.3	Results and Discussion	63
6.3.1	Characterization of m-TiO ₂	63
6.3.2	Photovoltaic Performance	68
6.4	Conclusion	77

7	Stability of m-SnO₂ based PSCs and the role of the TCO	79
7.1	Introduction	79
7.2	Experimental methods	82
7.2.1	Material characterization	82
7.2.2	Solar cell preparation	82
7.2.3	Solar cell characterisation	82
7.3	Results and Discussion	83
7.3.1	Characterization of compact SnO ₂	83
7.3.2	Characterization of m-SnO ₂	88
7.3.3	Photovoltaic performance	88
7.3.4	Stability of PSCs	91
7.4	Conclusion	95
 8	 Highly efficient m-SnO₂ PSCs through Gallium doping	 97
8.1	Introduction	97
8.2	Experimental methods	100
8.2.1	Material characterization	100
8.2.2	Solar cell preparation	100
8.2.3	Solar cell characterisation	100
8.3	Results and Discussion	101
8.3.1	Characterization of Ga-doped SnO ₂	101
8.3.2	Solar Cell Characterization	104
8.4	Conclusion	112
 9	 Coalescence of perovskite crystals	 113
9.1	Introduction	113

Contents

9.2	Experimental methods	115
9.2.1	Material characterization	115
9.2.2	Solar cell preparation	115
9.2.3	Solar cell characterisation	115
9.3	Results and Discussion	116
9.3.1	Photovoltaic performance	116
9.3.2	Optoelectronic Characterization	118
9.3.3	Film Morphology	120
9.3.4	Thermodynamics of Coalescence	123
9.4	Conclusion	126
10	Conclusions	127
11	Outlook	129
References		131
12	Curriculum Vitae	147
13	Related Publications	149

1 Introduction

Supplying the world with clean and renewable energy is one of the main challenges mankind is facing at the start of the 21st century. The annual world energy consumption has risen from 118.000 terawatt hours (TWh) at the start of the century to 156.000 TWh in 2012. Because of increasing populations and the rapid industrialisation of the developing world, this figure is predicted to increase further to 327.000 TWh by 2050. At present, 89.9% of this energy is supplied by fossil fuels and nuclear energy [1]. However, there are significant drawbacks in the use of these energy sources. Greenhouse gases released during the consumption of fossil fuels are believed to play an important role in the global climate change, while other pollutants released during fossil fuel consumption are reported to cause an estimated 3 million premature deaths annually [2]. Additionally, fossil fuel reserves are finite, estimated to run out within the next 100 years [3]. Nuclear energy is an unattractive alternative due to the processing and long-term storage of nuclear waste [4].

Renewable resources on the other hand are clean and abundant. Although hydro and biofuels are currently the largest suppliers of renewable energy, solar energy is the fastest growing technology [5]. Considering the huge potential of solar energy this is no surprise; with 885 million TWh reaching the earth annually, this is enough to meet the global annual demand for energy 5000 times over [6]. What remains is the technological challenge to convert this solar energy in a cheap and efficient way. Although the price of solar energy has dropped 200 fold since it's introduction forty years ago [7], solar energy is still 10-50 times more expensive than energy generated from fossil fuels [8].

The main type of commercial solar cell is the monocrystalline silicon solar cell. The drawback of this technology is the high initial cost due to the high price of silicon feed stock and the high energy consumption of the processes needed to purify the material to solar cell standards. To overcome this problem, a number of new technologies are being investigated, which employ cheap and abundant materials that can be easily processed in large quantities [9]. Amongst these technologies perovskite solar cells (PSCs) are a relative newcomer. However, in the span of only five years, lab-scale efficiencies of PSCs have rapidly become comparable to established monocrystalline silicon technology. The success of PSCs can be attributed to a high light absorption coefficient, large charge diffusion lengths and the benefit of being able to profit from twenty years of research done on the closely related dye sensitized solar cells (DSSCs). Besides the up-scaling from lab-scale fabrication to module production, the long term stability of these devices has become the most important impediment to commercial application. As a result, the PSC field is shifting from trying to further improve the efficiency of PSCs, to enhancing the long term stability [10, 11].

The hole blocking layer and mesoporous electron transporting layer are two key components of the PSC, usually consisting of the same metal oxide semiconductor. This thesis aims to explore the influence of the metal oxide on the performance and stability of PSCs. The thesis will begin with the fundamental working mechanisms underlying solar cells in *Chapter 2*, followed by an overview of the field of PSCs in *Chapter 3*. The architecture of a PSC will be described, as well as the properties of the materials used to construct these devices. The desired mesoporous structure of metal oxides described in this thesis is achieved by making use of the self-assembly behaviour of block-copolymers. In *Chapter 4* this technique will be described in

detail. *Chapter 5* covers the experimental techniques and methods used throughout this thesis.

Chapter 6 describes the synthesis of neodymium (Nd) doped mesoporous titanium dioxide (TiO_2) and the application of this material in PSCs. Electron microscopy and X-ray diffraction are used to study the impact of Nd-doping on TiO_2 morphology. Several spectroscopic techniques are used to investigate the impact of Nd-doping on the electronic properties of TiO_2 and the performance of PSCs employing Nd-doped TiO_2 as electron transporting layer. Nd-doping is also shown to reduce UV-induced degradation. *Chapter 7* goes on to explore mesoporous tin dioxide (SnO_2) as a more stable substitute to TiO_2 , due to the larger band gap, and addresses fluorine migration from the FTO electrode to the SnO_2 hole blocking layer, a process that is shown to have been limiting device performance of SnO_2 based PSCs. *Chapter 8* goes on to further improve the efficiency of SnO_2 based PSCs by doping with gallium (Ga), achieving similar efficiencies to TiO_2 based devices, but with improved UV-stability, paving the way for more stable PSCs.

Chapter 9 investigates the mechanism behind the spontaneous increase of device performance upon storage of PSCs in a dark and dry environment at room temperature. It is found that perovskite crystals can spontaneously coalesce, thereby improving charge transport, leading to an overall increase of device performance.

2 Fundamentals of Solar Cells

A solar cell is a device that directly converts the energy carried by light into electricity. Light is electromagnetic radiation, consisting of particles called photons. The energy (E) a photon carries depends on the wavelength (periodicity or frequency) (Figure 1) and is given by,

$$E = \frac{hc}{\lambda}, \quad (1)$$

h is Planck's constant, c is the speed of the light in a vacuum and λ is the wavelength of the photon. For solar cells, only the radiation emitted by the sun is of interest. The sun emits radiation ranging from the ultraviolet (UV) into the infrared (IR) part of the spectrum, corresponding to wavelengths ranging from 250 to 2500 nm. However, not all radiation emitted by the sun reaches the surface of the earth, a substantial part is absorbed by the atmosphere (Figure 2) and can not

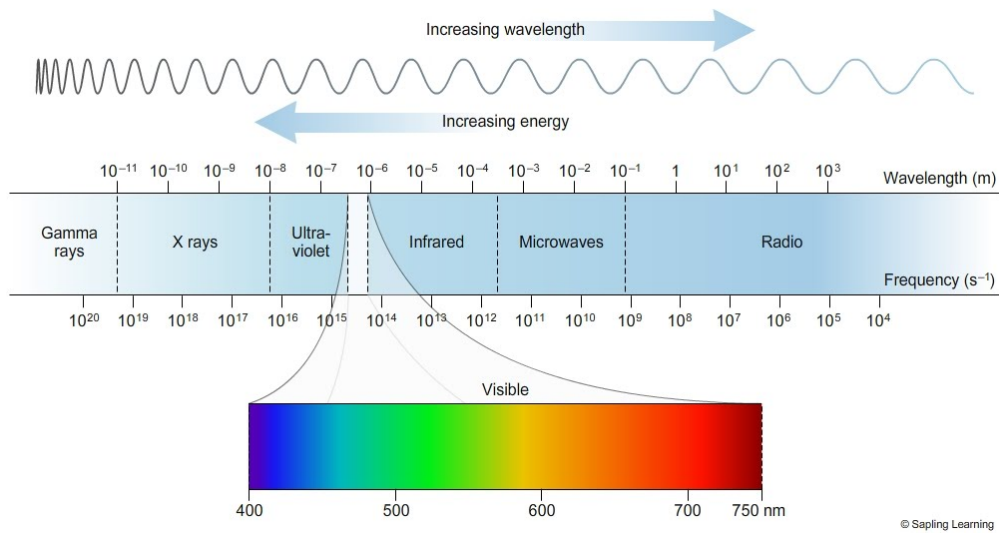


Figure 1: The electromagnetic spectrum; the energy carried by a photon decreases with increasing wavelength. Adapted from [12].

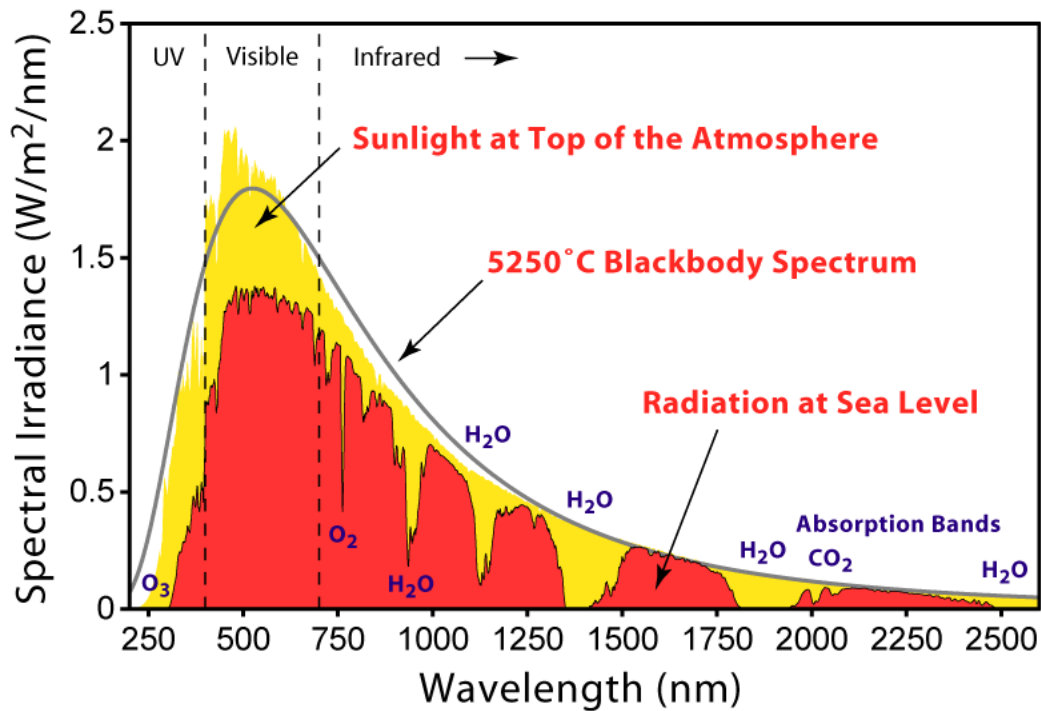


Figure 2: Spectrum of the electromagnetic radiation emitted by the sun, at the top of the atmosphere (yellow) and at the surface of the earth (red). A substantial part of the radiation is absorbed in the atmosphere before it reaches the surface of the earth. Adapted from [13].

be used for electricity generation. Solar cells strive to capture as much as possible of the remaining energy by absorbing photons and converting them into electricity.

Semiconductors are a special class of materials that have an energy gap between their highest filled energy band (valence band, VB) and lowest empty energy band (conduction band, CB). This property makes semiconductors well suited for solar cell applications. When light is absorbed by a semiconductor, photons excite electrons from the VB into the CB, leaving a so-called hole in the VB. Because of the

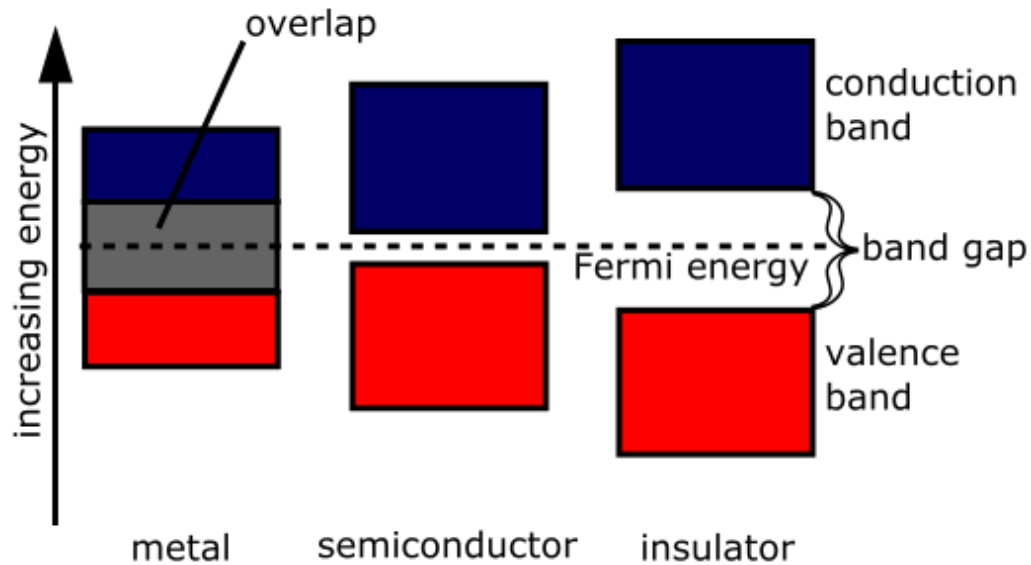


Figure 3: Schematic representation of the band structure of a conductor (metal), a semiconductor and an insulator. Adapted from [15].

energy gap, electrons can not readily relax back to their initial energy state and can diffuse away from the hole. This generates an electric field, driving the electrons through an external circuit to do electrical work [14]. When the VB and CB overlap, such as in metals, electrons relax back to their initial energy state before they can diffuse, preventing the build up of an electric field and the extraction of electrons. Materials having a bandgap that is so large it can not be overcome by the energy provided by photons, is called an insulator (Figure 3). In order to effectively exploit the excitation of electrons and achieve a high conversion efficiency from solar to electrical energy, several physical processes need to be considered, i) the absorption of photons to generate charge carriers (electrons and holes), ii) the subsequent separation of charge carriers of opposite type and iii) transport of the charge carriers to their respective electrodes.

It was established earlier that the absorbing material needs a bandgap to separate charges that are generated upon absorption of a photon. For this to occur, the bandgap energy needs to be smaller than the energy of the absorbed photon. Photons with energies larger than the bandgap excite electrons to states above the CB edge (the lowest CB energy), which subsequently relax to the CB edge. The energy that can be harvested is therefore given by the bandgap and the surplus energy of the photon above the bandgap is lost by these relaxation processes. The ideal choice of the bandgap is therefore a compromise between two considerations: a large bandgap provides a high energy that can be harvested, but reduces the part of the solar spectrum that can be absorbed. On the other hand, a small bandgap allows the absorption of a larger portion of the solar spectrum, but more energy is lost for high energy photons. William Shockley and Hans-Joachim Queisser calculated the ideal bandgap by taking into account these two considerations (Figure 2). They found that a maximum of 33.7% of the sun's energy can be turned into electricity for a 925 nm (1.34 eV) bandgap (Figure 4) [16].

The material needs to absorb as much as possible of the light that has an energy greater than the bandgap. This can be achieved by applying a thick layer of the absorbing material, however the charge collection will become less efficient with increasing thickness due to defects in the material, as defects can trap charges that can then no longer contribute to the current. The optimum thickness is thus a compromise between high absorption while maintaining good charge transport.

To separate charges of opposite type the absorbing material should be contacted in such a way that the charges experience a spatial asymmetry. This can be achieved by an electric field or a gradient in electron density. Usually, a junction is formed

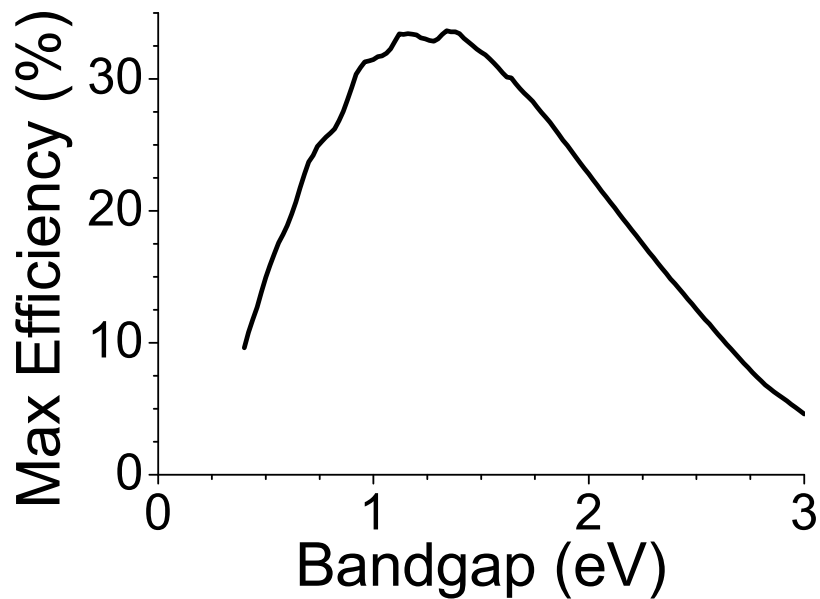


Figure 4: The Shockley-Queisser limit for the efficiency of a solar cell, using the solar spectrum as shown in Figure 2. Adapted from [17].

between the absorber and an electron transporting material (ETM) and/or hole transporting material (HTM). These junctions are of key importance as the charges should lose as less of their electrical potential energy as possible, while still being efficiently injected into the respective transporting layer. Note that in an ideal (lossless) semiconductor such a diode structure is not necessary because electrons and holes can diffuse to the right electrode. However, this process is too slow in non-ideal semiconductors and charges would recombine before reaching the electrode.

Lastly, to efficiently transport the charges to an external circuit, the materials comprising the solar cell have to be good electrical conductors. Charges should not recombine or lose energy due to resistances while being transported [14].

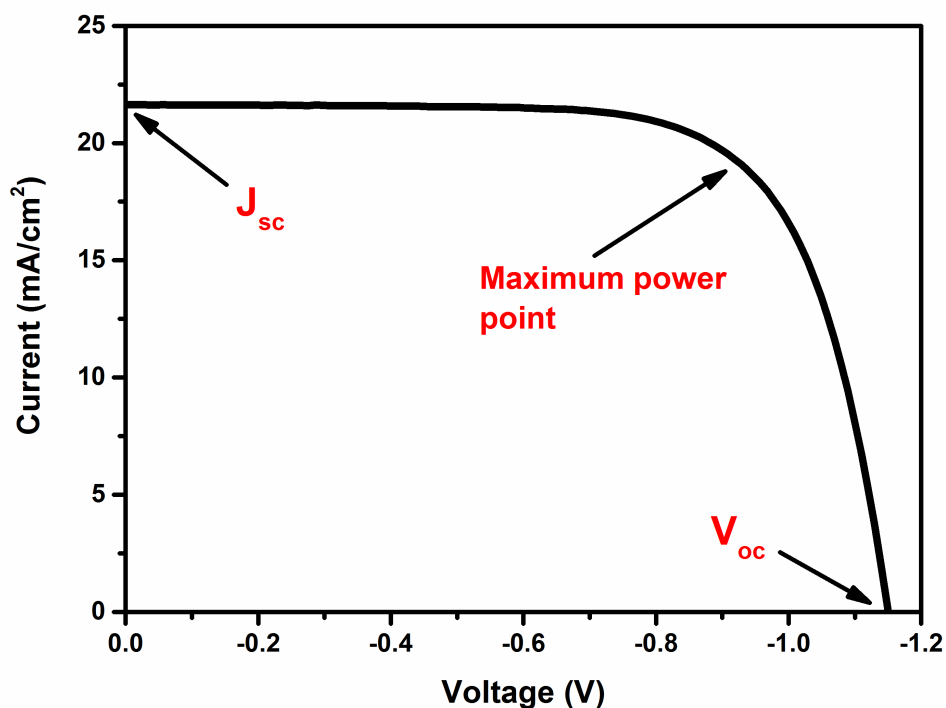


Figure 5: A characteristic J - V -curve of a solar cell. Maximum power point, V_{OC} and J_{SC} are indicated for clarity.

Several techniques can be used to assess how well a solar cell performs. The most simple and widely used method is the current-voltage (J - V) scan (Figure 5), in which the voltage is scanned, while recording the current response under illumination. The three important quantities governing the efficiency of a solar cell are the short circuit current J_{SC} , the open circuit voltage V_{OC} and the fill factor FF . J_{SC} is the current through the device in the absence of a net voltage, that is, in a short-circuited device. It is highly dependent on light absorption and charge collection efficiency. V_{OC} is the voltage across the device in the absence of a net current. It depends on the energy difference between the VB of the HTM, CB of the ETM, bandgap of the absorber and on recombination processes. The fill factor quantifies

the maximum power that can be delivered by the device. It is defined by dividing the maximum power output of the device (which is the maximum of $J \times V$) by $J_{SC} \times V_{OC}$ (which is the theoretical maximum power). Its magnitude depends on series and shunt resistances in the device. A low series resistance and high shunt resistance minimize internal losses, thereby maximizing the power output of the device [18].

This chapter discussed solar cells in general, the next chapter will introduce and explain in more detail the perovskite solar cell. A relatively new, but extremely promising technology.

3 Perovskite Solar Cells

This chapter will give an introduction to PSCs and the evolution and current state of the field, followed by a description of the working principles of PSCs. Because the focus of this thesis is on the ETM of the PSC, the properties of TiO_2 and SnO_2 will be discussed in more detail.

3.1 Introduction

Perovskites are a class of materials with the chemical formula ABX_3 , A and B are cations of different sizes, with A being larger than B and X is an anion [19]. The crystal structure is shown in Figure 6. The first such described material was calcium titanium oxide, which was discovered by Gustav Rose in 1839 and named after the Russian mineralogist Lev Perovski. In 1958 Christian Møller discovered that cesium lead halides had a perovskite structure with the chemical formula CsPbX_3 . He also noted that the compounds were intensely coloured and photoconductive [20]. The first organic-inorganic hybrid perovskite was synthesized in 1978 by replacing cesium with methylammonium (CH_3NH_3) [21].

Despite the promising properties of this perovskite, it was not implemented in solar cells until 2009, when Kojima *et al.* demonstrated the use of $\text{CH}_3\text{NH}_3\text{PbI}_3$ and $\text{CH}_3\text{NH}_3\text{PbBr}_3$ in a liquid-electrolyte-based DSSC. The efficiency reached a humble 3.8 % and due to the rapid dissolution of the perovskite in the liquid electrolyte stability was very poor [22]. Im *et al.* improved the performance to 6.5 % by changing

Parts of this Chapter have been published in
Roose, B., Pathak, S., Steiner, U., "Doping of TiO_2 for sensitized solar cells" *Chemical Society Reviews*, **44**, 8326-8349 (2015)

the method of deposition [23]. The liquid-electrolyte was subsequently replaced by a solid-state hole transporting material (2,2',7,7'-tetrakis (*N,N*-di-*p*-methoxyphenylamine)-9,9'-spirobifluorene (spiro-OMeTAD)) [24,25], marking a big step in performance and stability, which brought perovskites to the attention of the scientific community. Especially the work of Lee *et al.* was revolutionary, as it showed that perovskite does not need a conducting mesoporous scaffold, instead perovskite itself transports electrons to the anode. In addition, the perovskite was shown to also be an excellent hole conductor [26]. This set perovskite apart from DSSCs, as charge transport can occur in the perovskite itself, the absorber is no longer limited to being applied as a monolayer. This in turn sparked a new device design in which the perovskite fully infiltrates the metal oxide scaffold and forms a capping layer on top (Figure 7), allowing for much thinner devices [27]. Modifying the perovskite composition proved to allow further enhancement of device performance and stability, as methylammonium was (partly) replaced by formamidinium [28], guanidinium [29], cesium [30] or rubidium [11]. The method of perovskite deposition is equally as important, with two-step deposition [31], thermal evaporation [32] and anti-solvent dripping [33] (a process where a solvent in which the perovskite does not dissolve is dripped onto the perovskite precursor film to initiate crystallisation), all showed significant improvements. The method of deposition mainly affects the morphology of the perovskite film, where a pinhole-free film with large crystallites is required to obtain high efficiencies. These advances have led to PSCs now reaching efficiencies exceeding 22%, rivalling the efficiency of commercial solar cells [9].

The biggest remaining challenge is now to extend the lifetime of PSCs [34–36], although other issues, such as the use of toxic lead [37] and up scaling [38] can not be ignored either. Established solar cell technologies retain more than 80% of

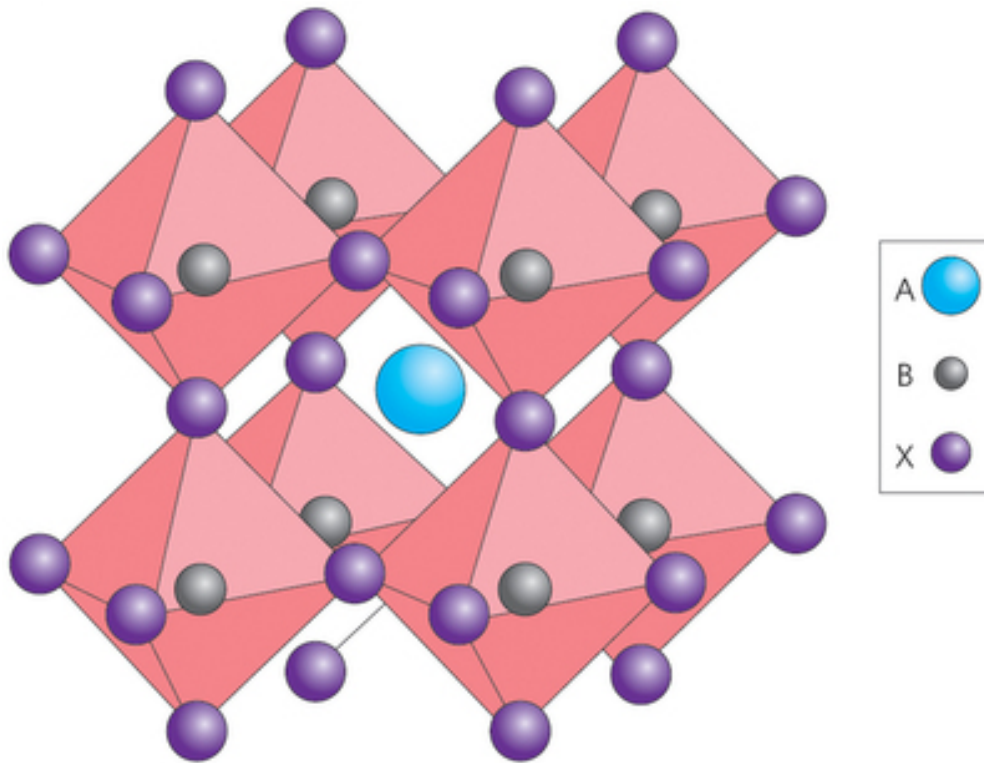


Figure 6: Perovskite crystal structure. For perovskites used in solar cells, the large cation A is usually cesium, or a small organic cation like methylammonium (CH_3NH_3) or formamidinium ($\text{CH}(\text{NH}_2)_2$), the small cation B is Pb or Sn and the anion X is a halide (I, Br or Cl). reprinted by permission from Macmillan Publishers Ltd: Nature Photonics [19], copyright (2014)

the initial efficiency after 25 years of operation [39]. First reports on PSC stability showed devices degraded within the first days to weeks after preparation [40–42]. Major degradation pathways include moisture [36, 43, 44], oxygen [45], heat [46, 47], light-soaking [48] and UV-light induced degradation [41], as well as the migration of mobile species in the device [49, 50]. Although the effect of many of these phenomena can be limited by encapsulating the device [51], they may still play a role

on a 25 year time-scale and extensive work has been done to increase PSC resilience.

TiO₂ is the default ETM in PSCs, the instability of TiO₂ towards UV-light is however a major cause of performance loss [41]. The instability has a dual cause, upon exposure to UV-light, oxygen desorbs from TiO₂, exposing deep traps that increase recombination [52]. Additionally, TiO₂ is a known photocatalyst [53] and can degrade organic compounds (such as the organic cation in perovskite). This instability can be limited by doping [52], or prevented by using larger band-gap materials such as SnO₂ [54], which absorb less UV-light and are less likely to be affected by light induced (performance) degradation pathways. Additionally, it was found that a mesoporous ETM provided increased stability over both planar ETM and an inert mesoporous scaffold due to the combined effects of a better perovskite morphology with less pinholes [55] and rapid extraction of electrons [56].

The stability of perovskite was found to be increased by substituting some of the iodide by bromide [40], chloride [57] or thiocyanite [58], or by substituting the organic cation with formamidinium [28], cesium [30] or rubidium [11].

The HTM was found to play an important role in long term stability as well. Spiro-OMeTAD is the most commonly used HTM in conventional PSCs, which needs to be doped to achieve high conductivity and charge mobility. Lithium-bis(trifluoromethane)sulfonamide (Li-TFSI) has been extensively used for this purpose. This dopant is however highly hygroscopic and increases moisture and oxygen induced degradation [36]. TFSI salts with less hygroscopic cations were found to significantly increase device lifetime [59, 60]. Another strategy is to replace Spiro-OMeTAD with more stable alternatives such as poly(3-hexylthiophene) (P3HT)

[61], tetrathiafulvalene derivative (TTF) [62] or copper iodide (CuI) [63].

Lastly, the choice of back electrode can play an important role. Silver (Ag) is easily corroded [36] and gold (Au) can migrate into the device under the influence of the electric field. The deposition of a thin layer of chromium (Cr) has been shown to be quite effective to stop Au migration [50]. Carbon-based electrodes have attracted great attention as well due to their excellent stability [64].

These advances have extended the lifetime of PSCs to more than 6 months [10]. This thesis attempts to contribute to extend this lifetime to 25 years by investigating the role of the ETM and reduce the effect of the ETM on device degradation.

3.2 Architecture of perovskite solar cells

PSCs have the advantage of a high absorption coefficient, needing just ~ 500 nm thick films to absorb most of the incident photons [65]. In comparison, silicon solar cells need an absorbing layer that is tens to hundreds of μm thick, implying the requirement of a much more pure and thus more expensive material [14]. Excitons in perovskites have a low binding energy, making it easy to separate holes and electrons [66] and excellent charge transport was measured within perovskites for both electrons and holes, with carrier diffusion lengths exceeding $1 \mu\text{m}$ [66]. This allows for very thin devices, the architecture of which is discussed below and shown in Figure 7.

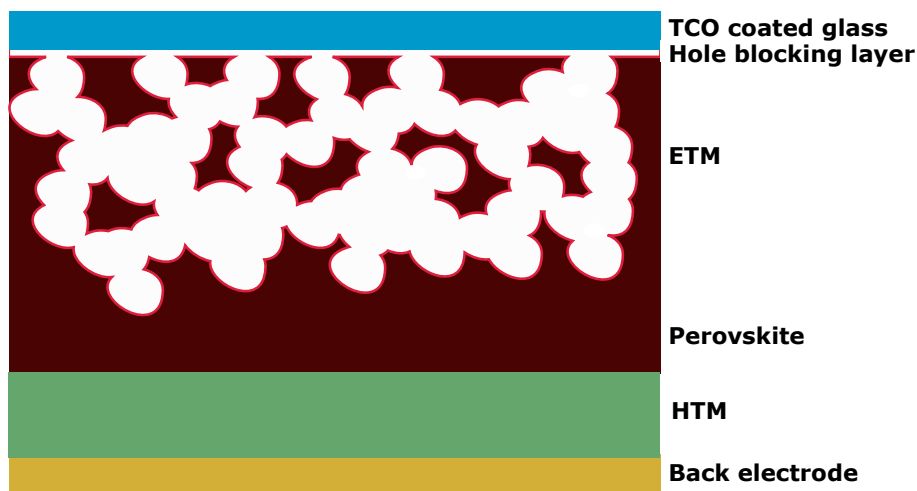


Figure 7: Perovskite solar cell architecture (from top to bottom): glass panel coated with a TCO; hole blocking layer and mesoporous electron transporting layer, typically titanium dioxide (TiO_2) or tin oxide (SnO_2); a perovskite layer infiltrating the porous electron transporting layer and forming a thick capping layer; hole transporting layer and back electrode.

PSCs are build up using the following components

- Front contact, consisting of a transparent conducting oxide (TCO) deposited on top of a glass panel. Common TCOs are indium tin oxide (ITO), fluorine doped tin oxide (FTO) and aluminum doped zinc oxide (AZO).
- Hole blocking / electron selective layer, a thin conformal coating on top of the TCO, separating the TCO from the rest of the device to prevent recombination and shunting.

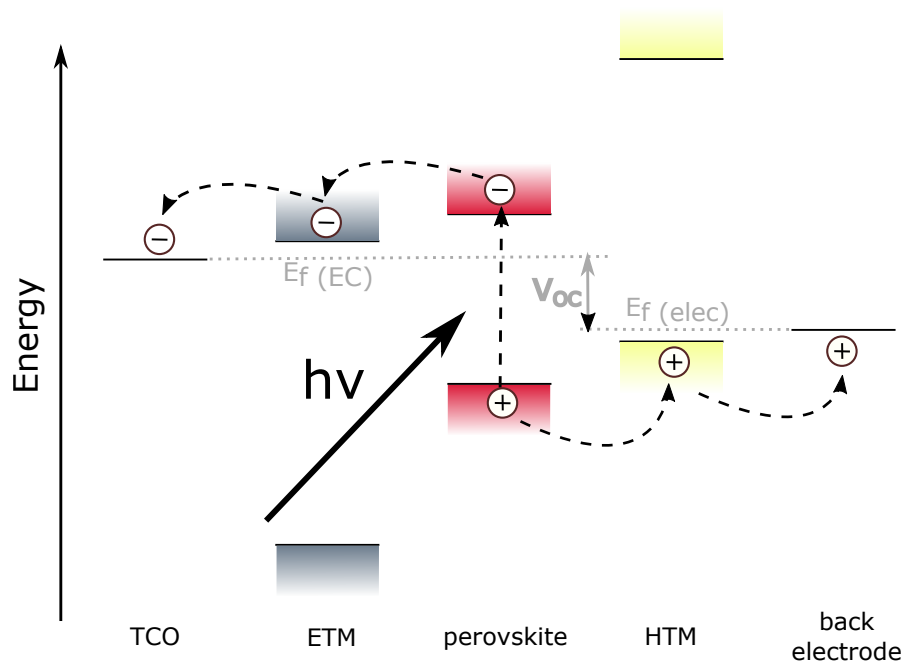


Figure 8: Perovskite solar cell band-diagram, showing the relative energy levels of the TCO, ETM, perovskite, HTM and back electrode. Also shown is the charge transport upon excitation of an electron from the VB to the CB of the perovskite.

- Electron transporting material (ETM); the function of the ETM is to accept electrons from the perovskite and the subsequent transport of the electrons to the front contact. Although highly efficient PSCs have been fabricated without ETM [67], most PSCs do employ an ETM to improve the perovskite morphology [56], charge separation [68] and stability [69].
- Perovskite, infiltrating the ETM and forming a thick capping layer; this layer is responsible for the absorption of light.
- Hole transporting material (HTM), which transports holes to the back contact.
- Back electrode, usually gold, but other highly conductive materials, such as carbon, have been employed as well [64].

The band-diagram of a PSC is shown in Figure 8. Upon absorption of an incident photon ($h\nu$) by the perovskite, an electron is excited from the VB to the CB. This electron is then injected into the ETM and transported to the front electrode. Meanwhile, the hole that is left in the VB of perovskite is transferred to the HTM and from there to the back electrode. By connecting the electrodes to an external circuit the system can perform electrical work.

To obtain high efficiencies, it is important to match the CB of the ETM to the CB of the perovskite so that the potential difference is sufficiently large for electron injection, while keeping the difference between the CB of the ETM and the VB of the HTM as large as possible to maximize V_{OC} [18] In DSSCs the maximum V_{OC} is roughly the energy difference between the VB of the HTM and the CB of the ETM. However, in PSCs band bending occurs at the interfaces, resulting in larger obtainable V_{OC} from perovskite absorbers with larger bandgaps.

Although a J - V scan such as in Figure 5 can give a good indication, typically more measurements need to be done to establish the performance of a PSC. The direction in which the J - V scan is performed (either from open circuit to short circuit, or from short circuit to open circuit conditions) can greatly influence the shape of the curve (Figure 9a) [70]. This phenomenon is called hysteresis and has been attributed to capacitive currents, trapping and detrapping processes, ferroelectric polarization, ion migration and charge accumulation at interfaces, although recent studies seem to indicate that a combination of ion migration and charge accumulation at the interfaces is the most likely cause [71,72]. A better technique to obtain the device efficiency is maximum power point tracking (MPPT). For MPPT the device is kept at the voltage for which the power is at maximum for a prolonged amount of time (Figure 9b). During this period, the voltage of the maximum power point is ascertained by small variations around the maximum power point. This way a value can be extracted that closely resembles the efficiency under real working conditions [73].

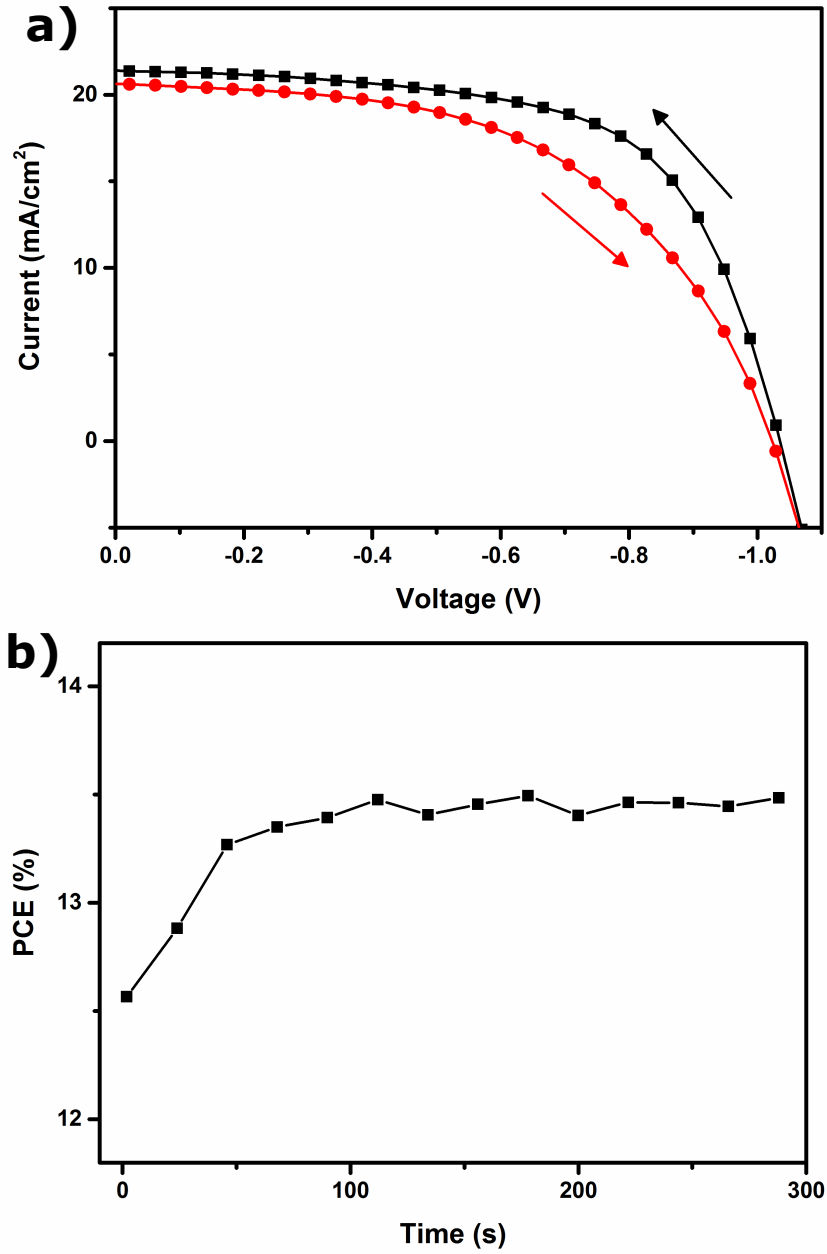


Figure 9: Establishing the efficiency of PSCs; a) J - V scans from open circuit to short circuit conditions (black) and from short circuit to open circuit conditions (red), clearly illustrating the hysteresis effect and b) maximum power point tracking.

3.3 Material properties

This section will expand on the material properties of TiO_2 and SnO_2 , two of the most used electron transporting materials in PSCs.

3.3.1 TiO_2

The large band gap, suitable band edge levels for charge injection and extraction, the long lifetime of excited electrons, exceptional resistance to photo corrosion, non-toxicity and low cost have made TiO_2 a popular material for solar energy applications [74–76].

TiO_2 occurs naturally in three crystalline forms; anatase (tetragonal), rutile (tetragonal) and brookite (orthorhombic). For PSCs, anatase is the most commonly used phase due to its superior charge transport. The tetragonal anatase crystal structure is made up of a chain of distorted TiO_6 octahedrons, which results in a unit cell containing four Ti atoms (at positions $[0,0,0]$, $[\frac{1}{2},\frac{1}{2},\frac{1}{2}]$, $[0,\frac{1}{2},\frac{1}{4}]$ and $[\frac{1}{2},0,\frac{3}{4}]$) and eight O atoms. The lattice parameters a and c are 3.7845 Å and 9.5143 Å respectively [77–79] (Figure 10).

TiO_2 prepared by sol-gel processes is amorphous and annealing at elevated temperatures is required to achieve the desired crystal structure. The crystallization temperature is limited by the anatase-rutile transition. Since rutile is the thermodynamically most stable polymorph of TiO_2 at all temperatures, the anatase to rutile transition temperature depends sensitively on preparation conditions. Because of their different band structures, mixed phases of anatase and rutile generally cause the trapping of charge carriers and promote recombination processes. They are

mostly undesirable in TiO_2 electrodes, although there are some studies suggesting a small amount of rutile nanoparticles can enhance device performance [80–82]. Devices employing rutile TiO_2 generally suffer from a lower CB compared to anatase, leading to a lower V_{OC} . In addition, reduced charge transport lowers the obtainable J_{SC} and FF , especially affecting the latter [83–85]. Because of these complications, rutile is not frequently used in PSCs.

The band gap of n-type semiconducting single-crystal anatase TiO_2 is approximately 3.2 eV, the resistivity is $\sim 10^{15} \Omega\text{cm}$ [86] and the mobility is $<1 \text{ cm}^2\text{V}^{-1}\text{S}^{-1}$

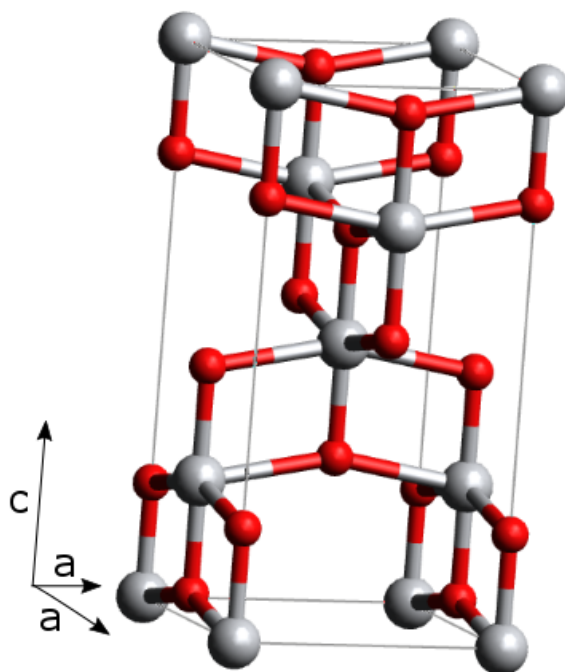


Figure 10: The anatase unit cell; titanium atoms are grey, oxygen atoms are red. Oxygen atoms form a distorted octahedron with a titanium atom at the center, which is clearly illustrated for the central titanium atom.

[87]. The lower edge of the CB is made up of vacant Ti^{4+} 3d bands and the upper edge of the VB is made up of filled O^{2-} 2p bands [88]. Bulk oxygen vacancies, titanium interstitials and reduced crystal surfaces generate shallow electron traps that can enhance the conductivity of TiO_2 as a result of the trapping-detrapping transport mechanism of electrons [89], as described below. Of particular interest here is the occurrence of Ti^{3+} species, which form a band roughly 0.5 eV below the TiO_2 CB. These defects act as n-type dopants, increasing the number of free electrons in the TiO_2 and hence the conductivity and current. At the same time defects can act as charge trap and are therefore recombination centers, having a negative effect on device performance [86, 90].

The number of defects can be influenced by moderately heating the device or by placing it in an inert atmosphere [91]. Furthermore, it was discovered that the number of traps can be reversibly changed by oxygen exposure or deprivation, indicating oxygen can adsorb onto TiO_2 defects and by doing so passivate trap states. A further remarkable observation is that UV irradiation causes the desorption of oxygen from these defects. Under exposure to air, oxygen release is counterbalanced by oxygen adsorption from the atmosphere. PSCs are however typically protected from degradation by air-free encapsulation. The lack of oxygen inside the encapsulated device upsets the desorption-adsorption balance, leading to an increase in trap states and deterioration of device properties. This again is reversible upon breaking the seal and exposure to oxygen [41, 52, 92].

Because of its many defects and the resulting sub-band gap states in TiO_2 (Figure 11a), electron transport is complex and hard to investigate. In devices, this is particularly difficult because parameters relating to one device property can not be stud-

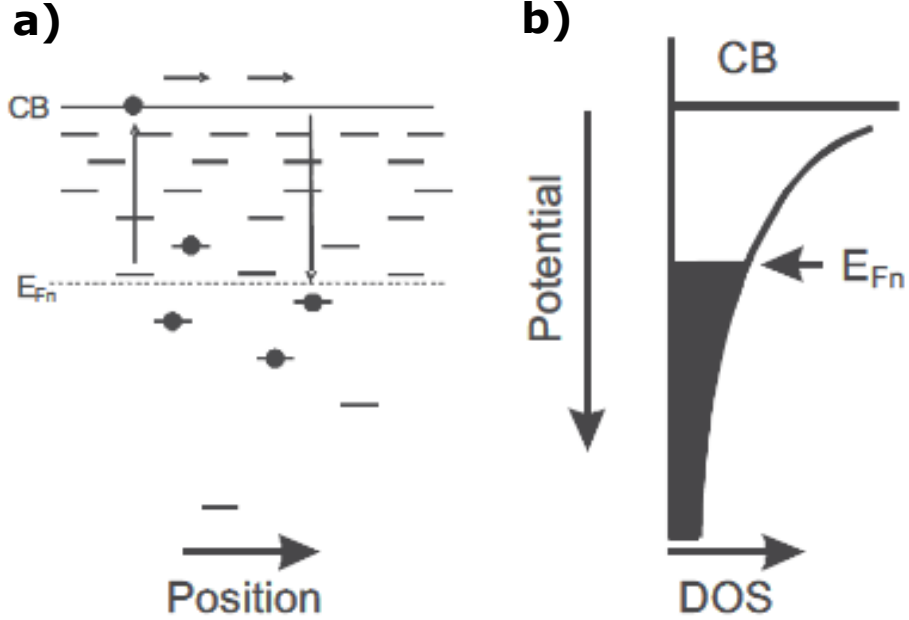


Figure 11: a) Schematic illustration of the trap distribution and trapping-detrapping process occurring in TiO_2 . The dotted line represents E_{Fn} in the TiO_2 , the long dashes represent vacant sub-bandgap sites and the filled circles represent electrons, vertical arrows represent trapping and detrapping and horizontal arrows represent transport. b) Illustration of the DOS distribution in solid films. The dark region below the E_{Fn} represents states with a probability greater than 50% of being filled. Reprinted with permission from [89].

ied individually without significantly changing other material properties. There is however strong theoretical and experimental evidence indicating that charge transport in TiO_2 proceeds by detrapping from sub-band gap states (Figure 11a). These states lie deep in the tail of the density of states (DOS, number of available states at a certain energy, Figure 11b), from which electrons can be detrapped into the CB, according to the multiple-trapping model for charge transport [89]. The occu-

pation of sub-band gap states at energy E_A can be found through the Fermi-Dirac distribution function

$$F(E_A - E_{Fn}) = \frac{1}{1 + e^{(E_A - E_{Fn})/k_b T}} \quad (2)$$

and the density of carriers at the energy E_A is $n_A = N_A F_A$, where N_A is the total number of available trap sites at this energy. From this, the density of electrons in the CB (n_{CB}) can be derived as a function of the position of the quasi-Fermi level for electrons (E_{Fn} , the quasi-Fermi level is the Fermi level of electrons in the CB, the Fermi level can be considered to be a hypothetical energy level of an electron, such that at thermodynamic equilibrium this energy level would have a 50% probability of being occupied at any given time, Figure 11),

$$n_{CB} = N_{CB} e^{(E_{Fn} - E_{CB})/k_b T} \quad (3)$$

Considering electron transport takes place only in the CB, the conductivity of the film is given by

$$\sigma = n_{CB} e \mu, \quad (4)$$

where μ is the electron mobility. Generally, a higher TiO_2 conductivity means a higher current output from the device. From the equations above it is apparent that the conductivity of the film is determined by the probability of the electrons being in the CB, which increases as the quasi-Fermi level approaches the CB. This means that any modification that eliminates deep trap states will increase the conductivity of the film [89].

To be able to effectively modify the trap states it is important to know where the traps are located. Different studies have suggested traps are located either in the bulk [93], at inter-particle grain boundaries [94] or at the surface of the particles [95, 96]. Bulk defects do not seem to play a major role [97] and it should be

noted that charge recombination is an interfacial process [98]. But because of the difficulty to experimentally distinguish between boundary or surface defects it is still unclear where exactly the traps are located [89], although there is strong evidence that traps are predominantly found at grain boundaries in block-copolymer templated metal oxides [99], such as the ones used in this thesis. Furthermore the synthesis method heavily affects defect locations and type. This makes it difficult to effectively modify the TiO_2 structure. It is understood that weakly reducing synthesis conditions and low annealing temperatures favor the formation of oxygen vacancies, whereas more reducing synthesis conditions and high annealing temperatures favor titanium interstitials as main defects [77, 86].

This combination of factors leads to the complex situation where shallow traps are essential for charge transport and can actually improve conductivity, but at the same time, deep traps lower the quasi-Fermi level, making it harder to detrapp electrons, decreasing conductivity and enhancing recombination. The V_{OC} of the device, which depends on the energy difference between the CB of TiO_2 and the VB of the HTM (Figure 8) and the bandgap of the perovskite absorber, is also affected by the trap states, with less deep traps resulting in a higher V_{OC} . Furthermore, traps can act as recombination sites for electrons and holes [77], which leads to a decrease in both current and voltage.

At the interface between TiO_2 and perovskite, band bending occurs due to the formation of a space charge region, implying that the CB in the bulk and at the surface do not have the same energy. The space charge region provides an electric field that separates electrons and holes. An external voltage can cancel out band bending and eliminate the space charge region. This specific voltage is called the

flat-band potential (V_{FB}) [100]. Because trap states are predominantly located on the TiO_2 surface they have a large influence on V_{FB} and thereby on the separation efficiency of electrons and holes. When V_{FB} is negatively shifted (indicating an upward shift of the CB and the Fermi level), the injection of electrons from the perovskite into TiO_2 will become less efficient and a loss in current occurs. The reverse is also true and some defects make injection more efficient by positively shifting V_{FB} , causing a downward shift of the CB and Fermi level. With so many interconnected processes it is clear that devising a method to improve the electronic properties of TiO_2 is not trivial.

3.3.2 SnO_2

Tin oxide (SnO_2) is often cited as a promising alternative to TiO_2 due to the high electron mobility ($\sim 250 \text{ cm}^2\text{V}^{-1}\text{S}^{-1}$) of SnO_2 [101] compared to TiO_2 ($< 1 \text{ cm}^2\text{V}^{-1}\text{S}^{-1}$) [87]. Additionally, the $\sim 3.6 \text{ eV}$ band-gap makes SnO_2 more robust

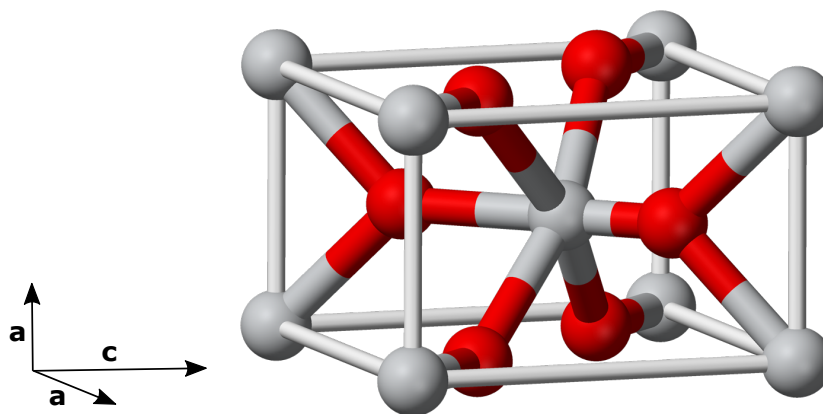


Figure 12: The rutile unit cell; tin atoms are grey, oxygen atoms are red. Oxygen atoms form an octahedron with a tin atom at the centre, which is clearly illustrated for the central tin atom.

and less photo catalytically active under UV-light than TiO_2 [102]. However, the major drawback of SnO_2 is the low CB (~ 0.3 eV lower than TiO_2), leading to a large overpotential at the perovskite/ SnO_2 interface and thus a loss of V_{OC} , and higher recombination, further limiting V_{OC} and FF [102, 103]. To address these issues, SnO_2 has been doped with a wide variety of metals such as Al, Mg, Ga and Zn [104–107], resulting in a higher CB and decreased recombination. Alternatively, core-shell structures have been synthesized to suppress recombination [108].

SnO_2 has a rutile (tetragonal) crystal structure, where each Sn atom is at the centre of an octahedron surrounded by six oxygen atoms, with a unit cell containing two Sn atoms (at positions $[0,0,0]$ and $[\frac{1}{2}, \frac{1}{2}, \frac{1}{2}]$) and four O atoms [109] (Figure 12). The lattice parameters a and c are 4.737 \AA and 3.185 \AA respectively [101]. The lower edge of the CB of SnO_2 is formed by the hybridization of O-2p and Sn-5s states. The upper edge of the VB consists of filled O-2p and Sn-4d states [110]. Bulk oxygen vacancies, tin interstitials, hydrogen interstitials and reduced crystal surfaces can enhance the conductivity of SnO_2 by acting as n-type dopants, increasing the number of free electrons [111, 112]. At the same time defects can act as charge traps and are therefore recombination centers, having a negative effect on device performance. Oxygen vacancies have been shown to form shallow trap states $0.15\text{-}0.30$ eV below the CB [113], indicating that reducing the number of oxygen vacancies may be an effective method to reduce recombination in SnO_2 based PSCs.

Due to the limited use of SnO_2 in DSSCs and PSCs, its properties have not been investigated as intensively as TiO_2 . However, there is strong evidence that electron transport in SnO_2 occurs *via* a similar trapping-detrapping mechanism as in TiO_2 [114] and traps play an equally ambivalent role in SnO_2 as in TiO_2 .

4 Block-copolymer templated metal-oxides

This chapter will introduce the concepts of block-copolymer self assembly and sol-gel chemistry and how a combination of the two can be used to synthesize mesoporous metal oxides, which can be used as ETM in perovskite solar cells.

4.1 Block-copolymer self-assembly

A block-copolymer (BCP) is a type of macromolecule consisting of two or more linear blocks of covalently linked monomers of chemically different moieties. The most simple variety is the diblock copolymer, consisting of a block of A and a block of B moieties, commonly denoted as poly(A-*block*-B). It is possible to link blocks with vastly different chemical properties, for example a hydrophilic and a hydrophobic block. Thermodynamically it is favourable for these blocks to demix, but because they are covalently linked only a partial demixing can be achieved. This leads to a segregation of the blocks in the range of 5-100 nm, depending on the length of the blocks [115].

Three parameters determine BCP morphology: (1) the overall degree of polymer-

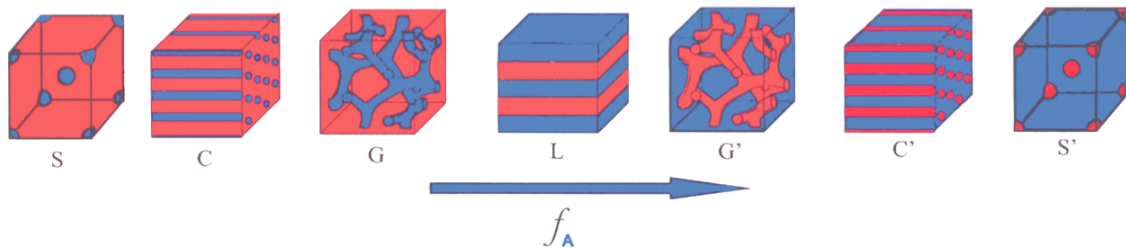


Figure 13: Different morphologies of BCPs, depending on the volume fraction f_A : spheres (S), cylinders (C), gyroid (G) and lamellar (L). Reprinted from [116].

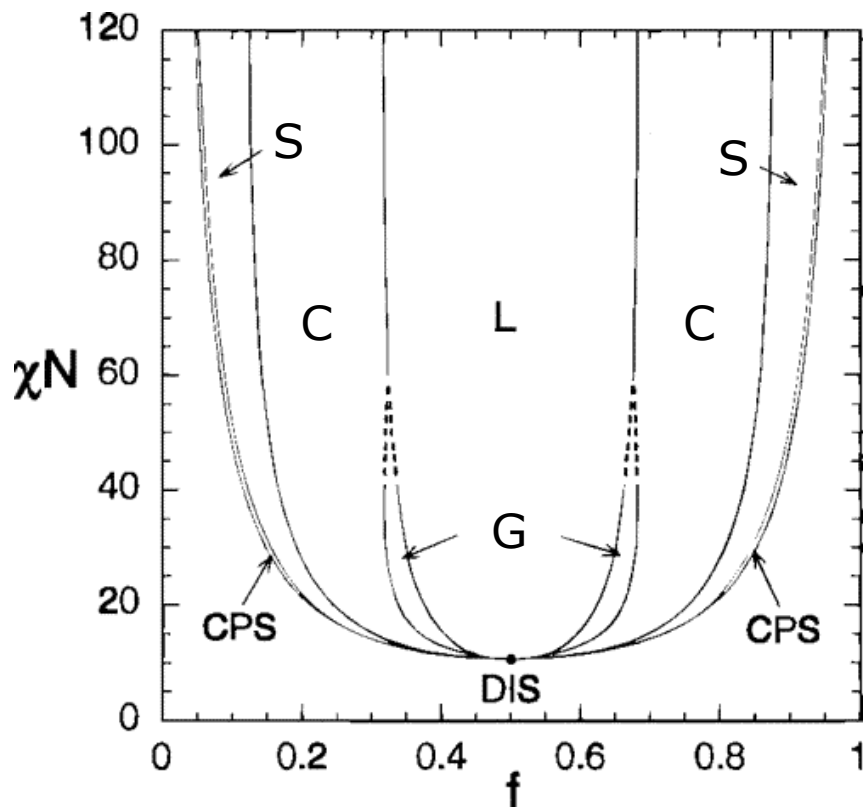


Figure 14: Phase diagram of a BCP, morphology depends on χ, N and f . Phases are labelled: disordered (DIS), close packed spheres (CPS), spheres (S), cylinders (C), gyroid (G) and lamellae (L). Adapted with permission from [117]. Copyright (1996) American Chemical Society.

ization N , which is the total number of monomers per polymer chain, (2) the volume fractions of the A and B blocks (f_A and f_B) and (3) the Flory-Huggins parameter, χ_{AB} . The χ -parameter specifies the incompatibility of the A and B blocks, which drives the phase separation [118]. The most common morphologies are spheres (S), cylinders (C), gyroid (G) and lamellae (L). A symmetric BCP ($f_A = f_B$) will adopt

a lamellar morphology, as optimal demixing at this volume fraction is achieved for planar interfaces. As the volume fraction asymmetry increases, these planar interfaces become less favourable and the system goes to a series of morphologies with increased interface curvature, starting from the gyroid, to cylinders and spheres, before becoming disordered. The dependence of the morphology on χ , N and f is shown in Figure 14. The degree of microphase separation depends on the segregation product χN . Because the incompatibility between the constituent blocks generally decreases with increasing temperature, χ is positive and varies inversely with temperature. This is reflected in the order-to-disorder transition (ODT), the temperature at which the copolymers become disordered [118].

The phase behaviour of BCPs in bulk is both theoretically and experimentally well understood [119]. However, the systems in this thesis are deposited from solution, increasing the level of complexity as the affinity of the separate blocks with the solvent has to be taken into account. In addition, the use of sol-gel chemistry (Section 4.2) in combination with BCP self-assembly makes it next to impossible to alter the morphology after deposition with solvent or temperature annealing.

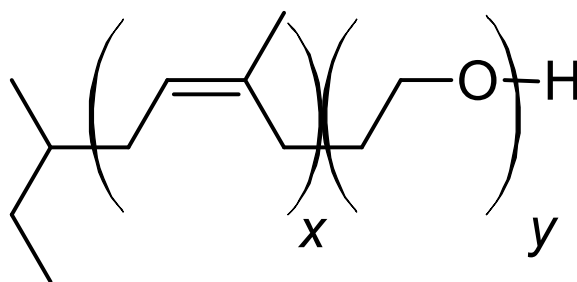


Figure 15: Chemical structure of PI-*b*-PEO, x and y can be varied independently to influence the morphology of the BCP.

In solution, amphiphilic (having a hydrophobic and a hydrophilic block) BCPs are known to form aggregates, including spherical micelles, rods and vesicles [120]. The BCP used in this thesis is the fully organic poly(1,4-isoprene-*b*-ethylene oxide) (PI-*b*-PEO, Figure 15) with $f_{PI} \approx 0.25$. In a polar solvent this BCP self-assembles into spherical micelles, with isoprene cores, encapsulated by a shell of ethylene oxide. When a thin film is cast from solution, the solvent will quickly evaporate, pushing the micelles close together, to form a densely packed assembly. How this morphology can be transformed into a porous metal oxide ETM, that can be used in PSCs, is explored in the next section.

4.2 Sol-gel chemistry

The sol-gel process is an important method for the fabrication of metal oxides from small molecules. In the process, reagents are molecularly mixed and the randomness of the solution state is trapped by rapidly quenching the system. This makes it possible to produce inorganic materials such as metal oxides at relatively low temperatures and short synthesis times [121]. The sol-gel process involves the conversion of metal oxide precursors from solution into a colloidal solution (sol) and finally into a network structure called a gel [122,123]. Typical precursors are metal alkoxides and metal chlorides. The morphology of the solid phase ranges from discrete colloidal particles to a continuous chain-like polymer network [124]. The sol-gel process can be summarized in the following key steps [122], corresponding to the numbers in Figure 16:

1. Synthesis of the "sol" through hydrolysis and partial condensation of alkoxides or chlorides.
2. Formation of the gel *via* polycondensation to form metal-oxo-metal or metal-hydroxy-metal bonds.
3. Aging; condensation continues within the gel network, often shrinking it and resulting in expulsion of solvent.
4. Drying the gel either to form a dense "xerogel" *via* collapse of the porous network or an aerogel for example through supercritical drying.
5. Removal of surface M-OH groups through calcination at high temperatures.

Complete hydrolysis often requires an excess of water and the use of an acid or base as hydrolysis catalyst [126].

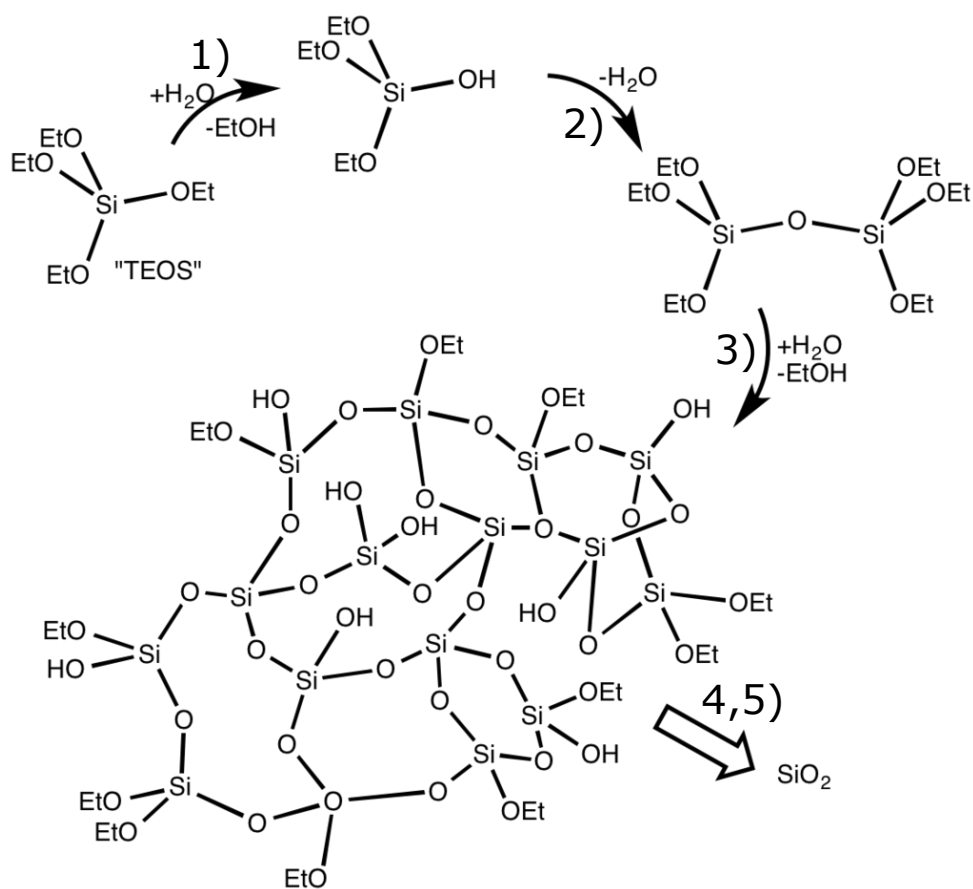


Figure 16: Sol-gel reaction of tetraethyl orthosilicate to form SiO_2 . The reaction proceeds the same way for any metal alkoxide or metal chloride. Adapted from [125].

This type of chemistry can be used to synthesize a wide variety of metal oxides, including TiO_2 and SnO_2 , from suitable precursors.

4.3 Combining BCP self-assembly and sol-gel chemistry

The self-assembly of BCPs can be used to direct the nanoscale assembly of metal oxides. Subsequently the polymer can be removed by heat treatment or etching, leaving behind the metal oxide, which now resembles the morphology of the structure directing polymer. Early work showed micellar structures with pore sizes up to 10 nm can be achieved by using surfactants in combination with silicate sol-gel chemistry [127]. By using BCPs the pore size could be increased and additional morphologies such as lamellae and cylinders were achieved [128]. In order for this approach to be successful, several conditions have to be met:

- The metal oxide sol has to be selectively incorporated in one of the BCP blocks. This is usually achieved by Coulombic interactions or hydrogen bonding [129].
- Particles in the sol have to be relatively small compared to the radius of gyration of the polymer chain to allow incorporation of the guest material, without strongly disturbing the chain conformation of the polymer [130].
- Self-assembly of the BCP needs to happen on a significantly faster time-scale than the gelation process of the metal oxide, to prevent particles from becoming too big to incorporate in the guest material [131].
- The solvent system has to dissolve both the BCP and the metal oxide precursors and allow uniform evaporation of the volatile species [132].
- Upon removal of the BCP, the metal oxide morphology has to be stable enough to support itself. To fulfil this last requirement a high metal-oxide precursor loading is needed [133].

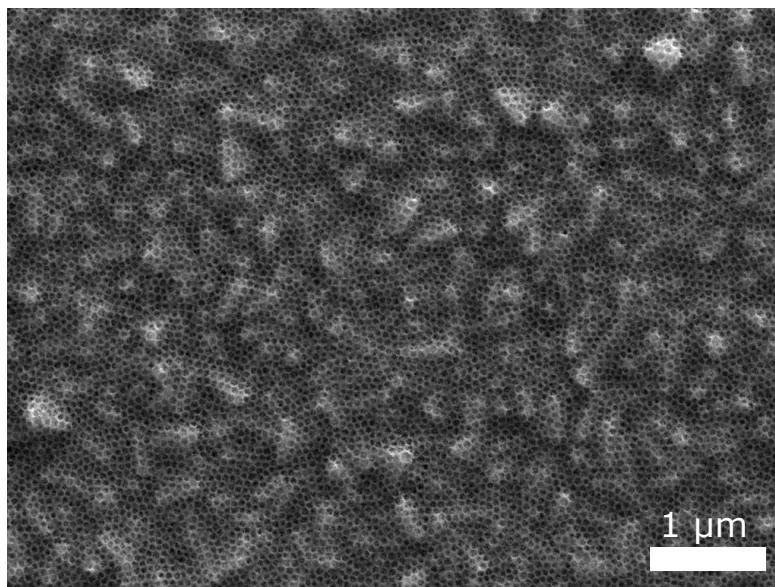


Figure 17: Example of the inverse micelle morphology of a porous metal oxide film, achieved by the BCP self-assembly directed synthesis method.

Metal oxides with different morphologies such as gyroids [134] cylinders and inverted micelles [135] have been employed as electron transporting material in solar cells, but the device performance seems to be affected more by the porosity of the morphology than by the morphology itself [135]. This allows the use of the inverted micellar morphology, which is achieved readily by spincoating of a precursor solution and subsequent heat treatment [136] and yields a highly porous structure such as the one shown in Figure 17.

An additional advantage of this method over conventional nanoparticle synthesis is the tight control over morphology. In doping studies, the dopant often influences the size of the nanoparticles and thus the morphology [123]. However, by using the BCP method, the morphology can be kept identical, excluding morphological influences from the study.

This Chapter has detailed how the combination of block-copolymer self-assembly and sol-gel chemistry can yield ETMs with identical morphology. This makes ETMs synthesized through this method extremely interesting for studying the role of metal oxides in PSCs, as is described throughout Chapters 6-8.

5 Experimental techniques and methods

This chapter will give an overview of the experimental techniques and methods used in this thesis, as well as a concise description of the working principles of some of the less straight-forward techniques.

5.1 Morphological characterisation

Two key methods for analysing the morphology of materials are scanning electron microscopy (SEM) and X-ray diffraction (XRD). Where SEM can be used to image the surface of a sample, XRD can be used to extract crystal structure, crystal size and lattice spacing.

5.1.1 Scanning electron microscopy

A scanning electron microscope produces images by scanning a sample with a focused beam of electrons. The electrons interact with atoms in the sample, which produces various signals that can be used to reconstruct an image revealing the topography and composition of the sample. The relevant signal used in this thesis are secondary electrons. These electrons are ejected from the sample by inelastic beam scattering interactions with beam electrons and are collected by a detector. By correlating the amount of secondary electrons with the beam position an image can be reconstructed with a resolution of up to 0.5 nm.

SEM was carried out on a Tescan MIRA 3 LMH with a field emission source operated at an acceleration voltage of 10 kV. ImageJ 1.48v was used to extract pore sizes and crystal sizes from SEM micrographs.

5.1.2 X-ray diffraction

XRD is a precise method to determine crystal structures. It is routinely used to determine the crystal structure and the presence of impurity phases. The Rietveld refinement method allows a detailed analysis of XRD spectra by using a least squares fit to approximate the measured diffractogram [137]. This way it is possible to determine the average crystallite size D by using the Scherrer formula [138, 139]

$$D = \frac{K\lambda}{\beta \cos \theta}, \quad (5)$$

where K is a dimensionless shape factor which is dependent on the shape of the particles (0.9 for spherical particles), λ is the wavelength of the X-rays, β is the full width half-maximum (FWHM) after subtracting the instrumental line broadening and θ is the Bragg angle. It is important to note that β and θ are in radians, whereas the instrumental output is usually in degrees. Furthermore, the inter-planar spacing d_{hkl} can be calculated with Bragg's law [140]

$$d = \frac{\lambda}{2 \sin \theta} \quad (6)$$

and using this interplanar spacing the lattice parameters a and c can be calculated for TiO_2 and SnO_2 using the Bragg formula for a tetragonal ($a = b$) lattice [141]

$$\frac{1}{d^2} = \frac{h^2 + k^2}{a^2} + \frac{l^2}{c^2}. \quad (7)$$

In this study XRD was measured using a Bruker D8 θ/θ (fixed sample) spectrometer with a LynxEye position sensitive detector and a standard SC detector with auto-absorber and graphite 2^{nd} beam monochromator. The spectrometer uses a Bragg Brentano parafocusing geometry and operates in reflection mode. Samples were deposited on Si-wafers and the (100) Si peak was used to calibrate the obtained spectra.

5.1.3 Cyclic voltammetry

Electrochemistry studies the relationship between electricity and chemical change. More specifically, reactions involving the movement of electric charges between electrodes and an electrolyte. These include reduction-oxidation (redox) reactions, in which a molecule or ion changes its oxidation state. Reduction and oxidation always occurs in a paired fashion, one species is oxidized when another is reduced.

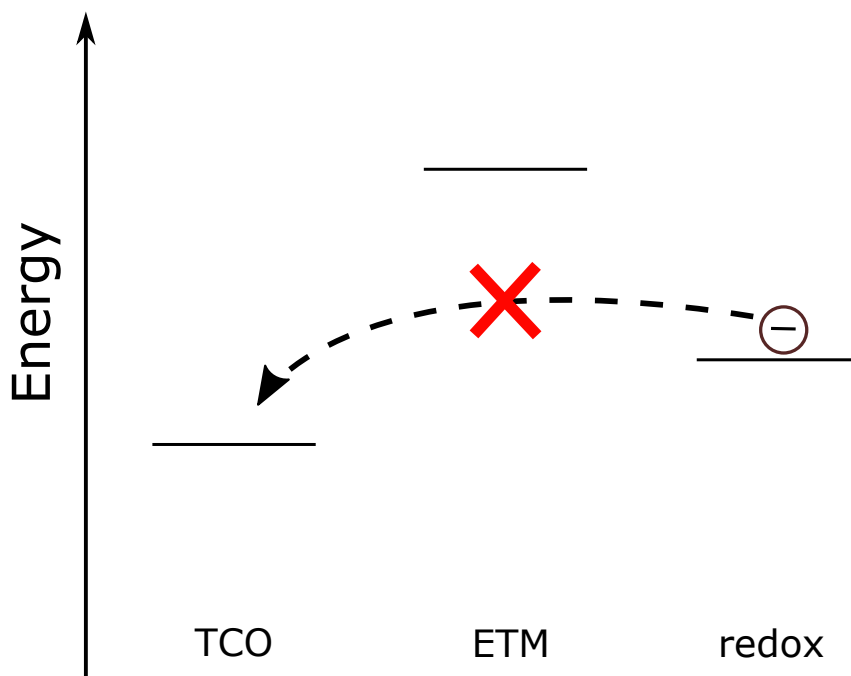


Figure 18: Simplified band-diagram of a redox reaction at the surface of a conducting substrate. Shown are the work function of the transparent conducting oxide (TCO) substrate, the CB of the ETM and the redox potential of the redox couple. Without an ETM, the reaction is allowed to occur freely, but in the presence of an ETM the reaction is (partially) blocked, as depicted by the red cross.

Redox reactions can be used to determine the effective coverage of a material on a conductive substrate. In order to do so, the redox-potential has to lie below the CB of the material covering the substrate, while still being able to transfer electrons to the substrate (Figure 18). If the material fully covers the substrate, the redox reaction will be completely suppressed and no current will be recorded. However, incomplete surface coverage, such as caused by cracks or pinholes, will result in a current. By comparing this current to the current collected for the bare substrate, an effective surface coverage can be calculated.

Electrochemical experiments were carried out using a Metrohm PGSTAT302N Autolab. SnO_2 ETMs were deposited on FTO and AZO electrodes through spray pyrolysis, as described in Section 5.3. A Ag/AgCl reference electrode was used in an aqueous electrolyte solution containing 0.5 M KCl (0.5 M), $\text{K}_4\text{Fe}(\text{CN})_6$ (0.5 mM) and $\text{K}_3\text{Fe}(\text{CN})_6$ (0.5 mM) [142]. Cyclic voltammograms were collected at a scan rate of 50 mV/s. The electrolyte solution was degassed of oxygen by purging with nitrogen before the measurement.

5.2 Material characterisation

Several techniques are employed to investigate material properties. X-ray photoelectron spectroscopy (XPS) is used to investigate material composition, UV/Vis spectroscopy to probe changes in the bandgap and photothermal deflection spectroscopy (PDS) to detect sub-bandgap states. Mott-Schottky analysis is a powerful tool to determine the CB edge and charge carrier density. Time-correlated single-photon counting (TCSPC) can be employed to probe recombination behaviour.

5.2.1 X-ray photoelectron spectroscopy

XPS is a quantitative technique that measures the elemental composition of a material, as well as the chemical and electronic state of the elements within the material. The sample is irradiated by a beam of X-rays, while simultaneously the kinetic energy and number of electrons escaping the sample are measured. As electrons in the bulk of the material have a higher chance of being trapped, the obtained signal originates mainly from the surface of the material. Each element produces a characteristic set of XPS peaks that can be used to identify the elements present in the sample. Each peak corresponds to the binding energy of an electron from one of the electron shells ($1s$, $2s$, $2p$, *etc.*). The atomic ratios of the constituent elements can be found by the relative intensity of the XPS signal (corrected by a relative sensitivity factor). In addition, the local bonding environment can instigate small shifts in the XPS signal, the so-called chemical shift. This chemical shift is dependent on the oxidation state of the atom in question and the interactions with the nearest neighbours and can thus give more detailed information about the local chemical environment of the elements in the sample.

5.2.2 UV/Vis spectroscopy

UV/Vis spectroscopy is used to determine the absorbance and bandgap of a material. In UV/Vis spectroscopy the intensity of light passing through a sample (I) is compared to the intensity of light before it passes through the sample (I_0). The transmittance (T) is defined as I/I_0 and the absorbance is given by

$$A = -\log(T). \quad (8)$$

Absorbance is usually plotted against the wavelength of the incoming light, clearly illustrating which part of the spectrum is absorbed by the material. For semiconductors the bandgap energy can be estimated from the absorption onset.

UV-vis absorption in films was measured using a Varian Cary 300 UV-Vis spectrophotometer.

5.2.3 Photothermal deflection spectroscopy

PDS is an ultra-sensitive absorption technique that can detect absorbance values as low as 10^{-5} [143]. This allows to detect sub-bandgap states, which play an important role in the electronic properties of semiconductors. For PDS measurements a sample (deposited on quartz) is submersed in an inert, non-absorbing material (typically a perfluorocarbon). A pump beam passes through the sample, heating up the sample and the surrounding liquid as it is absorbed, causing a refractive index gradient. A probe beam passes parallel to the sample and will be deflected proportional to the temperature gradient of the liquid near the sample. From this deflection the amount of absorbed radiation can be precisely determined.

PDS was measured with a Light Support MKII 100 W Xenon arc source coupled

with a CVI DK240 monochromator. The probe beam comes from a Qioptiq 670 nm fiber-coupled diode laser. [144]

5.2.4 Mott-Schottky analysis

Upon contacting an n-type semiconductor and an electrolyte solution containing a redox couple, the system will equilibrate by transferring electrons from the semiconductor to the redox couple, so that the Fermi levels (E_F) of the semiconductor and the redox couple are equal. This induces band bending and generates a space charge region in the semiconductor, which is positively charged, counterbalanced by a negatively charged region in the electrolyte. Changing the voltage of the semiconductor by using a potentiostat pushes the Fermi levels apart, resulting in a change

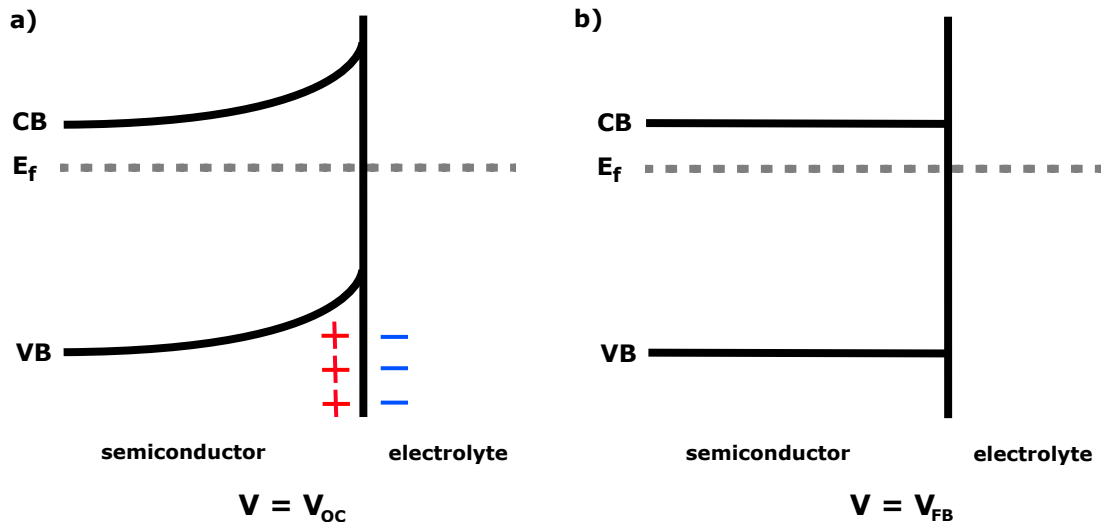


Figure 19: a) semiconductor in contact with an electrolyte with no applied voltage, the system equilibrates by transferring electrons from the semiconductor to the electrolyte and causing band bending. b) By applying a voltage equal to V_{fb} , there is no band bending.

of the amount of charges at the interface. When the applied voltage is such that there is no charge the semiconductor is at its flat-band potential (V_{FB})(Figure 19). The Mott-Schottky equation can be used to determine V_{FB} ,

$$\frac{1}{C^2} = \frac{2}{\varepsilon\varepsilon_0 A^2 e N_D} \left(V - V_{FB} - \frac{k_B T}{e} \right), \quad (9)$$

where C is the interfacial capacitance, ε is the dielectric constant of the semiconductor, ε_0 the permittivity of free space, A the interfacial area, N_D the number of donors, V the applied voltage, k_B is Boltzmann's constant, T the absolute temper-

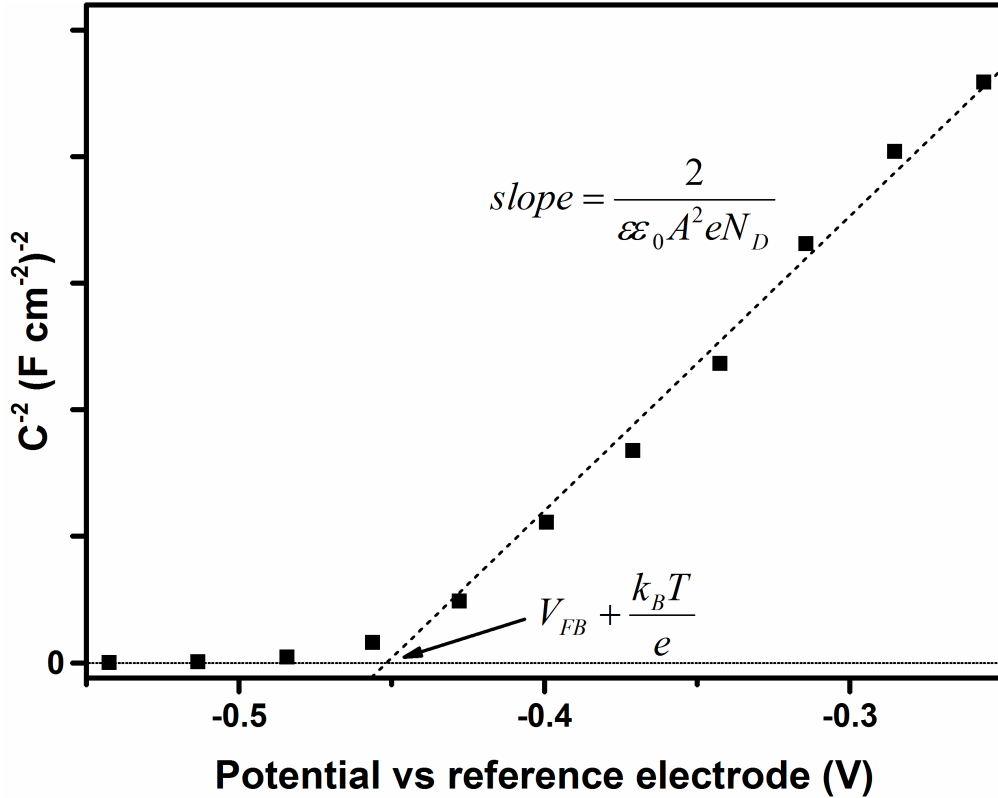


Figure 20: Mott-Schottky plot for a semiconductor, the relation between the intercept of the straight line with the V -axis and V_{FB} , and between the slope and N_D are indicated.

ature and e is the electronic charge. A plot of $1/C^2$ against V yields a straight line, from which V_{FB} can be determined from the intercept with the V -axis and N_D from the slope of the line (Figure 20). By referencing V_{fb} to a standardized electrode the relative CB position can be found [145].

In this thesis Mott-Schottky analysis was performed using a Metrohm PGSTAT302N Autolab. SnO_2 ETMs were deposited on FTO and AZO electrodes through spray pyrolysis, as described in Section 5.3. A Ag/AgCl reference electrode was used in an aqueous electrolyte solution containing 0.5 M KCl (0.5 M), $\text{K}_4\text{Fe}(\text{CN})_6$ (0.5 mM) and $\text{K}_3\text{Fe}(\text{CN})_6$ (0.5 mM). The electrolyte solution was degassed of oxygen by purging with nitrogen before the measurement. Electrochemical impedance data was collected at ~ 1 kHz to find the capacitance.

5.2.5 Time-correlated single-photon counting

The principle of TCSPC is the detection of single photons and the measurement of their arrival times with respect to a reference signal, such as a laser pulse. This way, it is possible to measure a radiative decay, such as fluorescence, as a function of time. This data can then be fitted and a charge lifetime can be extracted from the decay profile.

Fluorescence lifetime data was collected using a Florolog 322 spectrofluorometer (Horiba Jobin Yvon Ltd). A NanoLED-405LH (Horiba) laser diode (406 nm) (operated at a 400 kHz repetition rate) was used for excitation. The samples were mounted at 60° and the emission collected at 90° from the incident beam path. The emission monochromator was set to 760 nm with a 14 mm slit width and the photoluminescence was recorded using a picosecond photodetection module (TBX-

04, Horiba Scientific).

5.3 Solar cell fabrication

This section will give a layer-by-layer experimental description of the fabrication of PSCs and DSSCs.

5.3.1 Perovskite solar cell device assembly

Several different PSC architectures have been investigated for this thesis. This section describes the fabrication of each individual layer. The experimental sections of Chapters 6-9 will detail which particular device configuration was used.

TiO₂ compact layer

Nippon Sheet Glass with an FTO coating (10/□) was cleaned by sonication in a 2% Hellmanex solution for 30 minutes. After rinsing with deionised water and ethanol, the substrates were treated with UV-ozone for 15 minutes. A 30 nm TiO₂ compact layer was deposited via spray pyrolysis at 450 °C from a precursor solution of titanium diisopropoxide bis(acetylacetonate) in anhydrous ethanol.

SnO₂ compact layer

Fluorine doped tin oxide coated glass slides (Sigma-Aldrich, 7/□) and aluminum doped zinc oxide coated glass slides (Zhuhai Kaivo Optoelectronic Technology Co., <10/□) were cleaned by sonication in a 2% Hellmanex soap solution for 15 minutes. After rinsing with deionized water and ethanol, the substrates were again sonicated with isopropanol and rinsed with acetone. The substrates were treated with UV-ozone for 5 minutes and a 30 nm thick SnO₂ ESL was deposited by spray pyrolysis at 450°C from a precursor solution of butyltin trichloride (250 mM) in anhydrous ethanol [146]. Alternatively, a 15 nm thick SnO₂ compact layer was deposited by

atomic layer deposition (ALD) [147].

Mesoporous TiO₂ layer

Mesostructured TiO₂ electrodes were synthesised using a structure directing BCP [136], as described in Chapter 4. A titanium precursor sol was prepared by adding 50 µl of HCl (37 %) to 150 µl of titanium(IV) isopropoxide (TTIP) (Sigma-Aldrich, 99.999 %) and stirred for 10 minutes. For the doped samples, neodymium(III) isopropoxide (Sigma-Aldrich, 99.8 %) was dissolved in TTIP before the addition of HCl. The doping concentrations are given in terms of the Nd:Ti ratio. Subsequently, polyisoprene-*block*-polyethyleneoxide (PI-*b*-PEO) (50 mg, molar mass Mn= 34.4 kg mol⁻¹, 28wt % PEO) was dissolved in 1 ml of azeotrope (72.84wt % toluene and 27.16wt % 1-butanol) and added to the precursor sol. After 20 h, the resulting solution was spin-coated (4000 rpm, 20 s) onto the FTO substrate. The films were annealed on a programmable hotplate (2000 W, Harry Gestigkeit GmbH) using a linear 2 hour ramp to 600 °C followed by a dwell time of 1 hour to remove the BCP template and crystallise TiO₂.

Mesoporous SnO₂ layer

Mesostructured SnO₂ electrodes were synthesized using a structure directing BCP [136], as described in Chapter 4. A tin oxide precursor sol was prepared by dissolving poly(1,4-isoprene-*b*-ethylene oxide) (25 mg, Polymer Source, Mn: PI(50000)-PEO(12000), M_w/M_n: 1.05) in tetrahydrofuran (1 ml), after which tin(IV) chloride pentahydrate was added (80 mg) and stirred for 30 minutes. For the doped samples, gallium(III) acetylacetonate (Sigma-Aldrich, 99.99 %) was added to the solution. The doping concentrations are given in terms of the Ga:Ti ratio. The mixture was stirred for 30 minutes and then spin-coated (4000 rpm, 10 s) onto the substrate and

immediately transferred to a preheated hotplate (150 °C). The films were annealed on a programmable hotplate (2000 W, Harry Gestigkeit GmbH) using a 45 minute ramp to 450 °C followed by a dwell time of 30 minutes to remove the BCP template and crystallize SnO₂.

DT perovskite

A precursor solution containing formamidinium iodide (FAI) (1 M), lead iodide (PbI₂) (1.1 M), methylammonium bromide (MABr) (0.2 M) and lead bromide (PbBr₂) (0.2 M) in anhydrous DMF:DMSO 4:1 (v:v) was spin-coated in a two-step program at 1000 and 4000 rpm for 10 and 30 s respectively, to form a film of FA/MA mixed cation lead I/Br mixed halide perovskite, hereafter referred to as "DT" perovskite. During the second step, 100 µl of chlorobenzene was poured onto the spinning substrate 15 seconds prior the end of the program. The substrates were then annealed at 100 °C for 1 hour in a nitrogen glove box [148].

CDT perovskite

Cesium containing DT perovskite ("CDT") precursor solution was synthesized by adding 5 vol. % of cesium iodide (CsI) solution (1.5 M in DMSO) to a DT perovskite precursor solution. The perovskite solution was spin-coated in a two-step program at 1000 and 4000 rpm for 10 and 20 s respectively. During the second step, 100 µl of chlorobenzene was poured onto the spinning substrate 15 seconds prior the end of the program. The substrates were then annealed at 100 °C for 1 hour in a nitrogen glove box [30].

Hole transporting layer

Subsequently, the substrates were cooled down for a few minutes and a spiro-OMeTAD (Merck) solution (70 mM in chlorobenzene) doped with bis(trifluoromethylsulfonyl)imide lithium salt (Li-TFSI, Aldrich), tris(2-(1H-pyrazol-1-yl)-4-tert-butylpyridine)-cobalt(III)tris(bis(trifluoromethylsulfonyl)imide) (FK209, Dyenamo) and 4-tert-butylpyridine (TBP, Aldrich) was spun at 4000 rpm for 20 s. The molar ratio of additives for spiro-OMeTAD was: 0.5, 0.03 and 3.3 for Li-TFSI, FK209 and TBP, respectively. [149]

Gold electrode

70 nm of gold was thermally evaporated under high vacuum on top of the device.

5.3.2 Dye sensitized solar cell device assembly

Due to the overlap of the IMPS and IMVS signals of perovskite and metal oxides [150], DSSCs were used to perform these measurements instead.

Compact and mesoporous layers were fabricated as described above. m-TiO₂ electrodes were then immersed in a Y123-dye solution (acetonitrile/1-butanol, 50/50 *v/v* %) for one hour [151]. m-SnO₂ electrodes were immersed in a Z907-dye solution (acetonitrile/1-butanol, 50/50 *v/v* %) overnight [146]. Electrodes were rinsed with acetonitrile before the deposition of the hole transporting layer and gold electrode as described above.

5.4 Solar cell characterisation

Current-Voltage (J - V) characteristics were measured to obtain device performance.

5.4.1 Current-Voltage characteristics

For photovoltaic measurements, a solar simulator from ABET Technologies (Model 11016 Sun 2000) with a xenon arc lamp was used and the solar cell response was recorded using a Metrohm PGSTAT302N Autolab. The intensity of the solar simulator was calibrated to 100 mW/cm^2 using a silicon reference cell from ReRa Solutions (KG5 filtered). J - V -curves were measured in reverse bias (from high to low voltages), at a scan rate of 10 mV/s . The cells were masked to define the active area (0.09 cm^2) and were measured two days after their preparation. The voltage at the maximum power output was extracted from the J - V -curves, the device was then held at this voltage to obtain the variation of the stabilised power output efficiency with time.

5.4.2 Incident photon-to-current efficiency

The incident photon-to-current efficiency (IPCE) gives the efficiency of the conversion of incoming light to collected current, as a function of the wavelength of the incoming light. The area under the curve represents the current collected under the full spectrum white light and is thus equivalent to J_{SC} .

In this thesis, monochromatic light was derived from a 250 W tungsten halogen white light source (Newport, Model 66881) using a Oriel Cornerstone 130 monochromator. The light beam was split into two beams using a semi-transparent mirror. One beam is directed towards a reference photodiode (Thorlabs SM05PD1A), the

second beam illuminated the optoelectronic device under investigation. The current response was measured using a Keithley 2635 sourcemeter. Prior to the actual measurement, the reference diode was calibrated using a second diode (also Thorlabs SM05PD1A) with known spectral responsivity. The measurement was controlled with a LabView program.

5.4.3 Intensity Modulated Photocurrent Spectroscopy

For Intensity Modulated Photocurrent Spectroscopy (IMPS), the dynamic response of the solar cell to a small amplitude sinusoidal modulation of the incident light intensity is measured as a function of the angular modulation frequency ω . The incident photon flux Φ consists of a monochromatic modulated part (AC) superimposed on a constant background (DC). By measuring the photocurrent as a variation of the photon flux, a so-called transfer function can be constructed

$$H_{\text{IMPS}} = \frac{\Delta i}{\Delta \Phi} e^{i\varphi}, \quad (10)$$

where Δi is the variation of the current, $\Delta \Phi$ the variation of the photon flux and φ is the phase angle. In the case of single step one-electron charge transfer reactions, the frequency of the maximum imaginary part of the IMPS response, ω_{max} , corresponds to the sum of the charge transport and recombination rate constants. By performing the measurement at short circuit conditions the recombination rate becomes negligible compared to the transport rate and the electron transport time, τ_{tr} , is given by

$$\tau_{tr} = \frac{1}{2\pi\omega_{max}}. \quad (11)$$

τ_{tr} can be considered to be the mean arrival time of photogenerated electrons at the electrode [152, 153] and as such can be used to evaluate the conductivity of the electron transporting material.

IMPS was performed according to the procedure described in literature, using a 625 nm LED driver at different light intensities and a Metrohm PGSTAT302N Autolab. [153]

5.4.4 Intensity Modulated Photovoltage Spectroscopy

Intensity Modulated Photovoltage Spectroscopy (IMVS) is based on the same principle as IMPS, with the exception that the dynamic excitation of the incident photon flux is now related to the photovoltage, which is further related to the charge density. The corresponding transfer function is

$$H_{\text{IMVS}} = \frac{\Delta V}{\Delta \Phi} e^{i\varphi}, \quad (12)$$

where ΔV is the variation of the current, $\Delta \Phi$ the variation of the photon flux and φ is the phase angle. The frequency of the maximum imaginary part of the IMVS response, ω_{max} , again corresponds to the sum of the charge transport and recombination rate constants. This time, by performing the measurement at open circuit conditions, the transport rate becomes negligible compared to the recombination rate and the electron recombination time is given by

$$\tau_{\text{rec}} = \frac{1}{2\pi\omega_{\text{max}}}. \quad (13)$$

τ_{rec} can be considered to be the mean life-time of photogenerated electrons before they recombine [152].

IMVS was performed according to the procedure described in literature, using a 625 nm LED driver at different light intensities and a Metrohm PGSTAT302N Autolab. [153]

5.4.5 Charge extraction

Charge extraction is used to estimate the concentration of excess charge carriers in a device under operating conditions. It allows the concentration of electrons trapped in the device to be estimated as a function of potential [154]. For this measurement, the device is illuminated while being kept at open circuit at the start of the measurement. The illumination is then switched off and the voltage is allowed to decay simultaneously. After a set amount of time, or when a certain voltage is reached, the device is switched to short circuit conditions and all the remaining charge is collected. The amount of charge collected corresponds to the amount of filled energy states at this voltage. Because these energy states are well below the CB, they can act as electron traps. Charge extraction can thus be used to probe the trap state density of a device.

6 Neodymium doping of m-TiO₂ in perovskite solar cells

The aim of this chapter is to study the effect of doping TiO₂ with neodymium (Nd) on the performance and stability of perovskite solar cells (PSCs). The chapter describes the fabrication of mesoporous TiO₂ (m-TiO₂) electron transporting layers using BCP assisted assembly. The influence of Nd-doping on material properties of m-TiO₂ is described, as well as the influence on performance and stability of PSCs employing Nd-doped m-TiO₂.

6.1 Introduction

As described in Chapter 1, solar energy is one of the leading candidates to meet the ever increasing demand for energy. The costs for solar energy production are however currently higher than other conventional and renewable energy sources. [38] Potential low cost alternatives to the currently used Si and GaAs based solar technologies [9] include solar cells that make use of m-TiO₂ electrodes to collect and transport the electronic charges generated in metal-organic dyes (dye sensitised solar cells (DSSCs)), first demonstrated by O'Regan and Graetzel [155] and the subsequent introduction of organic-inorganic perovskites as light absorber, which combine high light absorption with good charge transport. [22,24,25,28,30–33] The high perovskite conductivity enabled the exploration of new device architectures

This chapter has been published as:

Roose, B., Gödel K. C., Pathak, S., Sadhanala, A., Correa Baena, J. P., Wilts, B. D., Snaith, H. J., Wiesner, U., Grätzel, M., Steiner, U., Abate, A., "Enhanced Efficiency and Stability of Perovskite Solar Cells through Nd-doping of Mesostructured TiO₂" *Advanced Energy Materials*, **6** (2), 1501868 (2016)

spanning from a perovskite-sensitized mesoporous TiO₂ to TiO₂-free planar heterojunction solar cells. [156] Currently, the best performing perovskite-based solar cells (PSCs), with a certified power conversion efficiency of more than 22%, employ a thin m-TiO₂ layer as electron selective contact in combination with a thick solid perovskite absorber capping layer.[2]

Due to the favourable position of its CB, a large band gap, long electron lifetimes and low fabrication costs, TiO₂ is the choice electron transporting layer for PSCs. [18] Nevertheless, the relatively high density of electronic trap states below the CB are a significant drawback for the application of TiO₂ electrodes in solar cells. [89] Indeed, trap states may have a large influence on charge recombination and charge transport, which in turn influence the solar cell voltage and current (see Section 3.3). [86, 90, 157] One method to reduce the trap states in TiO₂ is doping. A wide range of doping elements have been investigated for mesoporous TiO₂ electrodes in DSSCs and PSCs [18]. Some dopants reduce the charge recombination [158] or increase electron transport [159] by reducing trap states below the CB. In addition to changes in the density of trap states, doping may induce a complex interplay of other effects that impact the device performance; for example the TiO₂ nanoparticle size and distribution and thereby the morphology of the mesostructured film, leading to a changed TiO₂-absorber interface area in DSSCs. [160] Furthermore, lowering the CB energy of TiO₂ by doping can increase electron injection from the absorber into TiO₂ [161], thereby increasing J_{SC} , or increase V_{OC} by shifting the CB upwards. [162] These two effects however often adversely affect each other. Another observed effect of doping is the stabilization of the power output of PSCs [52] and a reduction of the hysteresis of the device current-voltage characteristic. [163]

In a previous study we showed that aluminium (Al) doping increases stability in DSSCs by passivating oxygen defects in the TiO₂ lattice. [52] We demonstrated that oxygen defects not only limit electron transport within the TiO₂, but are also the cause of fast deterioration of solar cell performance upon UV irradiation. Therefore, DSSCs prepared with Al-doped TiO₂ were significantly more stable to UV exposure. However, the short-circuit current was significantly lowered as a result of a reduced charge injection from the dye into the TiO₂, instigated by an upward CB shift.

In this study, the stability and the performance of PSCs was improved by Nd doping of the m-TiO₂ ETL. The Nd electron states are expected to have a negligible effect on the CB of TiO₂, [164] thus preventing the loss of photocurrent that was observed for Al doping. To study the electronic properties of the material independent of the film morphology, we use the BCP templated solution based method described in Chapter 4, which allows the preparation of identical mesoporous films irrespective of the Nd doping concentration. This way, we are able to demonstrate that Nd doping reduces the density of deep traps in the TiO₂ lattice, leading to reduced electron recombination, increased electron transport and increased stability in PSCs. Nd-doped TiO₂ PSCs with a stabilized power output of more than 18% were manufactured.

6.2 Experimental methods

6.2.1 Material characterization

SEM, XRD, PDS, XPS and UV/Vis spectroscopy were performed according to Sections 5.1 and 5.2.

6.2.2 Solar cell preparation

PSCs employing TiO₂ and DT perovskite and DSSCs employing TiO₂ and Y123-dye were prepared according to Section 5.3.

6.2.3 Solar cell characterisation

PSCs were characterised according to Section 5.4, using current-voltage scans and maximum power point tracking. DSSCs were characterised according to Section 5.4, using IMPS and IMVS.

6.3 Results and Discussion

6.3.1 Characterization of m-TiO₂

Scanning Electron Microscopy

A frequently observed phenomenon in doping studies is a decrease of the average TiO₂ particle size for doped samples, [123] leading to an increased TiO₂-absorber interface area, which results in improved performance. This however complicates the study of electronic properties of the materials as a function of dopant concentration. To exclude these morphological factors, we used the self-assembly of the

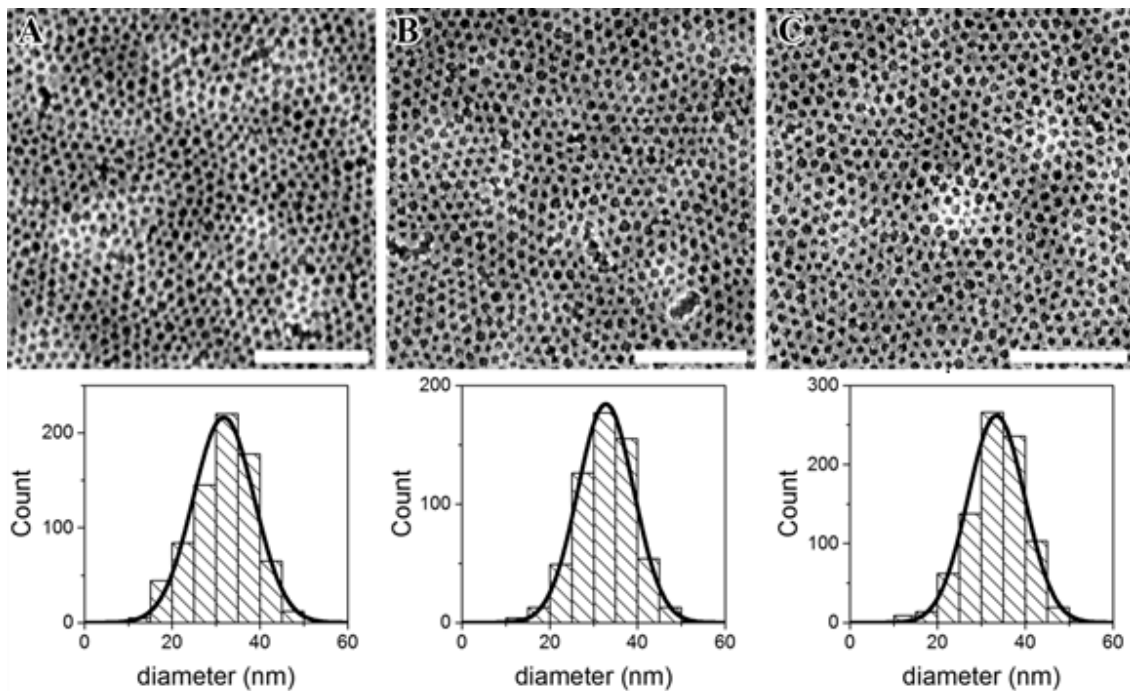


Figure 21: SEM micrographs of BCP self-assembly templated interconnected networks of a) TiO₂, b) 0.3% Nd-doped TiO₂ and c) 0.5% Nd-doped TiO₂. Scale bars are 500 nm.

Nd (%)	D_p (nm)	D_c (nm)	a (Å)	c (Å)
0	33 ± 6	25.9 ± 0.5	3.763 ± 0.001	9.431 ± 0.002
0.3	33 ± 6	26.2 ± 0.9	3.766 ± 0.001	9.439 ± 0.002
0.5	34 ± 6	23.5 ± 0.8	3.766 ± 0.001	9.437 ± 0.002

Table 1: Dopants and their main contribution to the improvement of DSSCs.

amphiphilic BCP polyisoprene-block-polyethyleneoxide (PI-b-PEO) to control the pore morphology during TiO₂ synthesis. The TiO₂ precursor complexes with the PEO block, yielding a porous network that is determined by the self-assembly of the polymer upon sample drying, calcination and removal of the polymer. [136] The pore morphology is dictated by the molecular weight of the BCP and the polymer-precursor concentration ratio, while the confinement of TiO₂ within the self-assembled morphology dictates the crystal size within the polycrystalline TiO₂ network. An inverse micelle inter-connected network with high porosity and surface area is formed during TiO₂ synthesis, where the pores are defined by the coil-size of the polyisoprene. Micrographs and corresponding pore size distribution (D_p) of samples for undoped (Figure 21a), 0.3% Nd-doped (Figure 21b) and 0.5% Nd-doped (Figure 21c) TiO₂ show very similar morphologies with pore sizes of approximately 33 nm (Table 1).

Crystal Structure

XRD was used to confirm the formation of anatase TiO₂. Figure 22 shows the spectra for pristine, 0.3% and 0.5% Nd-doped TiO₂, all peaks can be assigned to anatase TiO₂.

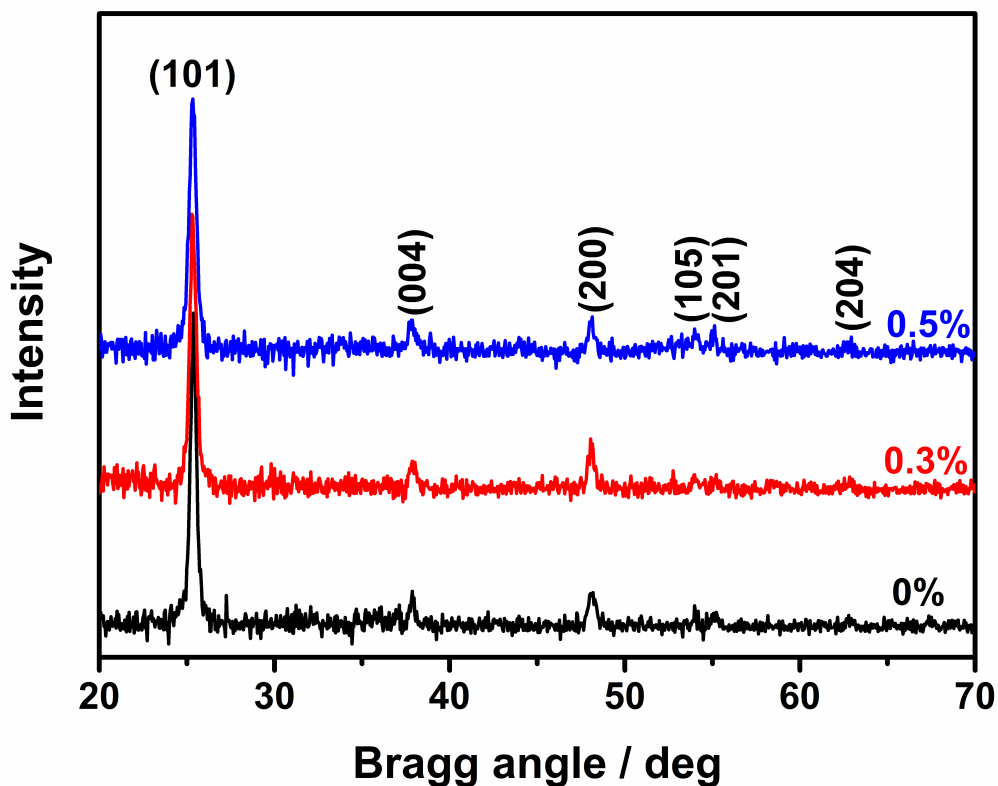


Figure 22: XRD diffractograms of mesoporous films of undoped, 0.3 and 0.5 % Nd-doped TiO₂. All peaks can be assigned to anatase TiO₂, indicating that Nd is incorporated into the TiO₂ lattice.

Because of the large difference in ionic radius between Nd³⁺ and Ti⁴⁺ (98 pm and 61 pm respectively [165]), the TiO₂ lattice expands upon substitutional incorporation of Nd³⁺, resulting in a peak-shift to smaller angles in the XRD diffractogram. Interstitial doping has a much smaller effect on the lattice spacing. [166] Due to the large size of the Nd ion it is likely to be incorporated near the surface of TiO₂ crystallites. Lattice parameters and particle sizes were calculated according to equations reported in Section 4.1.2. The values for the average size of crystallites (D_c) of the polycrystalline assembly and lattice parameters a and c are given in Table 1. D_p and

D_c are similar (~ 33 nm and ~ 25 nm respectively) for all doping concentrations, thus confirming that the BCP templating not only preserves the morphology for the different doping levels, but also confines the crystallisation, preserving the crystal size. The lattice parameters for the doped samples show a unilateral increase from 3.763 to 3.766 Å for a and from 9.431 to 9.439 Å for c . The initial increase in lattice parameters suggests substitutional incorporation is dominant for 0.3% Nd-doped TiO₂. For 0.5% Nd, the lattice expansion is very similar to 0.3% doping, suggesting additional Nd is incorporated interstitially or at the surface, where it may form an insulating coating.

Electronic Properties

PDS [167] was used to probe sub-band gap states in undoped and doped TiO₂ as reported elsewhere. [143] Figure 23 shows the PDS spectrum for TiO₂ with increasing Nd-doping concentration. The intra-bandgap state at 2.1 eV is attributed to the 4f transitions of Nd. [168] The peak intensity correlates with the doping concentration, indicating Nd is indeed increasingly incorporated into the TiO₂ lattice. Because the UV/Vis spectra (Figure 27) do not show a significant change in absorbance, a variation in the thickness of the films can be excluded as a possible cause for the observed change in intensity. Lanthanide induced intra-bandgap states are often associated with the up-conversion of low energy photons, making it possible to absorb photons that are otherwise lost. [169] Because of the low density of the intra-band gap states and the low quantum efficiency of up-conversion processes it seems however unlikely that up-conversion contributes significantly to light absorption.

The band gap of TiO₂ is ~ 3.2 eV, the energy levels of surface traps typically lie 0.5-0.7 eV below the CB (grey shading in Figure 23). [170, 171] In Figure 23, the

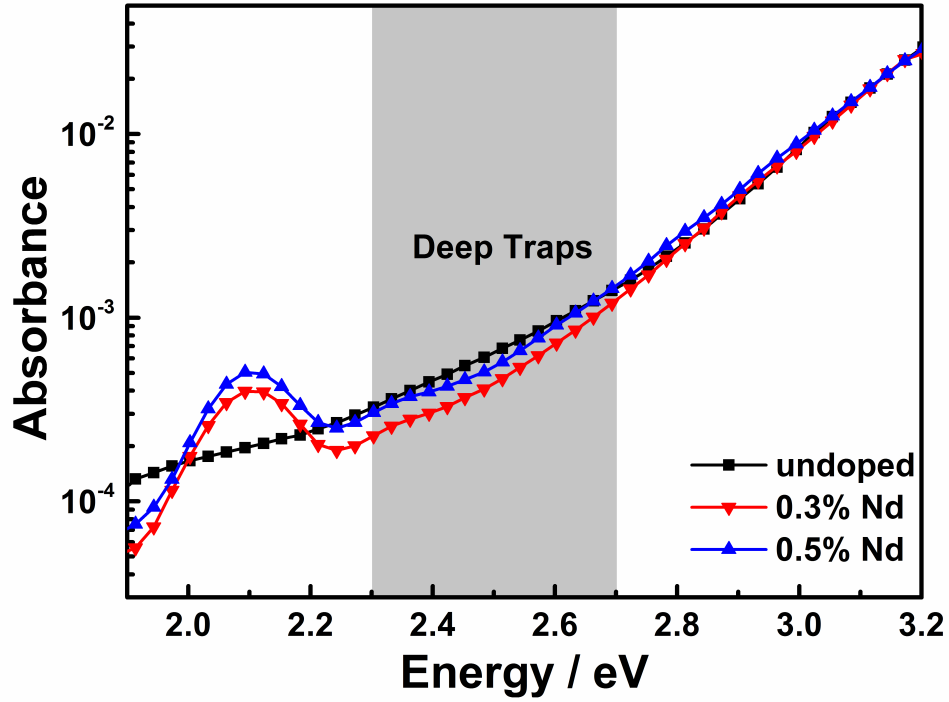


Figure 23: PDS spectrum of undoped, 0.3 % and 0.5 % Nd-doped TiO₂. Deep trap state energies are marked in grey. PDS is an ultrasensitive absorption technique that allows detecting absorbance values as low as 10⁻⁵.

trap state density in this energy range is lowest for 0.3 % Nd-doped TiO₂. Because deep traps can act as recombination centers it is expected that the recombination rate for 0.3 % Nd-doped TiO₂ is lower than that of pristine TiO₂. [89] For 0.5 % Nd-doped TiO₂ the trap state density increases again, presumably because interstitial Nd ions act as trap states, which is expected to lead to an increase in recombination and a loss in device performance.

Nd (%)	V_{OC} (mV)	J_{SC} (mA/cm ²)	FF (%)	PCE (%)
0	961	17.3	71.4	12.1
0.1	989	17.0	71.8	12.2
0.2	976	17.9	72.6	12.8
0.3	969	18.1	74.7	13.1
0.4	1003	17.2	72.0	12.6
0.5	1007	16.5	73.3	12.1

Table 2: Photovoltaic parameters of Nd-doped TiO₂: open-circuit voltage (V_{OC}), short circuit current (J_{SC}), fill factor (FF), power conversion efficiency (PCE). The J - V characteristics were recorded at reverse bias at a scan rate of 10 mV/s across a 0.16 cm² aperture active area.

6.3.2 Photovoltaic Performance

An initial doping concentration optimisation in the range of 0% to 0.5% Nd showed an increase in device performance up to 0.3% doping, after which the performance decreased. The results of this optimisation can be found in Table 2.

Undoped, 0.3% and 0.5% devices were further optimised and studied in more detail to find the reason for the increase and subsequent decrease in device performance. The results of this optimization can be found in Table 3. The SEM micrograph in Figure 24 shows the cross section of a photovoltaic device employing a ~150 nm thick mesoporous layer of TiO₂.

The photocurrent-voltage (J - V) curves of the PSCs measured under AM1.5 simulated solar light (100 mW/cm²) illumination are shown in Figure 25. The photo-

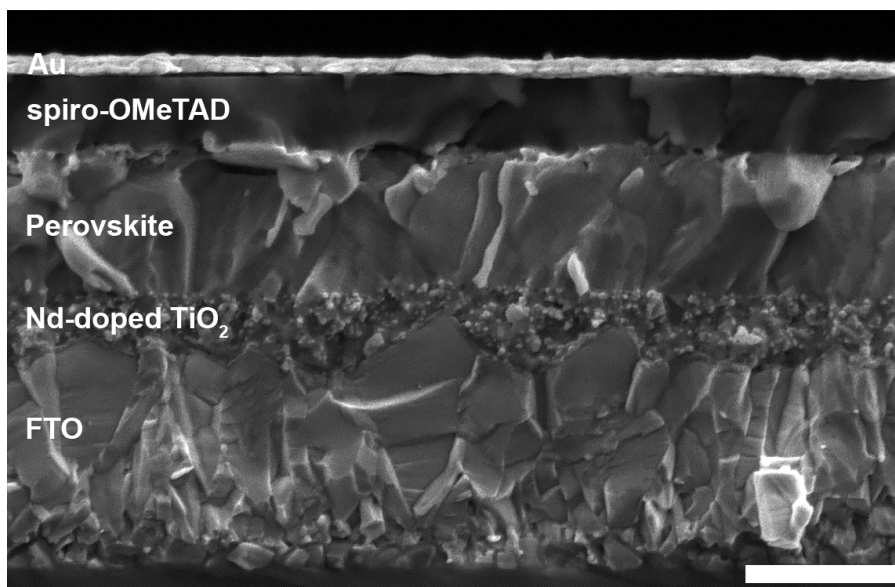


Figure 24: SEM cross-section of a photovoltaic device, scale bar is 500 nm; FTO transparent conductive electrode, compact TiO₂ electron blocking layer, 150-200 nm Nd-doped mesoporous TiO₂, perovskite capping layer, spiro-OMeTAD hole conducting layer and gold back contact.

voltaic parameters extracted from the J - V -curves, the open-circuit potential (V_{OC}), short-circuit current (J_{SC}), fill factor (FF), power conversion efficiency (PCE), and the stabilised power output efficiency after 30 s and 200 s are shown in Table 3. The maximum PCE is achieved for 0.3% Nd doped TiO₂, mainly through the improvement of the fill factor. In contrast to the earlier study employing Al doping in DSSCs, [52] no loss in J_{SC} was observed. This can be correlated with the fact that the Nd doping does not affect the TiO₂ band gap, as evidenced by identical UV/Vis spectra for all doping concentrations (Figure 27), showing also that the CB position is unaffected, a change of which would lead to a decrease in electron injection and a loss of J_{SC} .

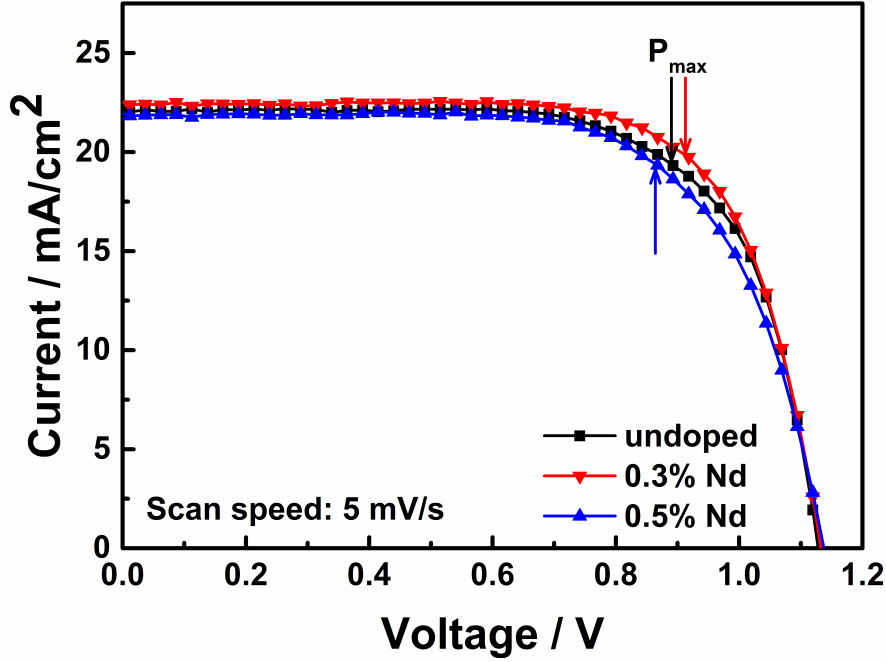


Figure 25: (J - V -curves for PSCs employing TiO₂, 0.3% Nd-doped TiO₂ and 0.5% Nd-doped TiO₂. The J - V -curves were measured from forward bias to short circuit condition at the scan rate of 5 mV/s under AM1.5 simulated solar light (100 mW/cm²) illumination. The cells were masked (0.16 cm²) and characterized two days after their preparation. Table 3 lists the photovoltaic parameters for the three curves.

Because the obtained efficiency in PSCs is dependent on the way the device is measured (preconditioning bias (light and voltage), voltage scan speed and direction) additional measurements are needed to verify the obtained PCE for device operation under realistic conditions. By determining the maximum power point and keeping the system at the corresponding voltage for extended periods of time, a realistic PCE value can be determined. [73] Figure 26 shows the PCE at the maximum power point for the first 200 seconds, which demonstrates that steady-state

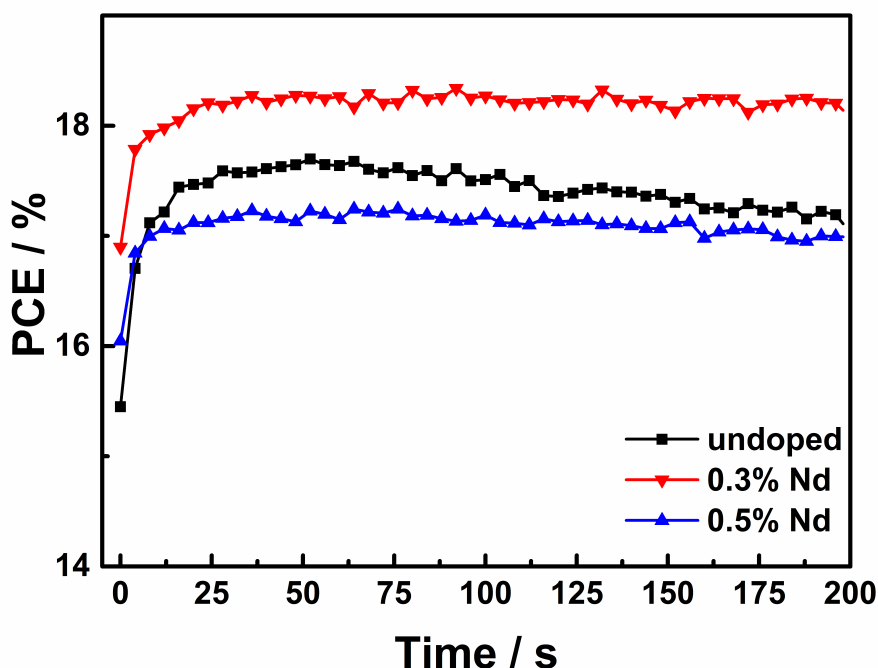


Figure 26: (Stabilized PCE of undoped, 0.3 % Nd-doped and 0.5 % Nd-doped TiO₂ PSCs. The voltage at the maximum power output was extracted from the J - V -curves, the device was held at this voltage for 200 s to obtain the stabilized power output efficiency.

conditions are achieved after approximately 30 seconds. We note that, regardless the doping level of TiO₂, the steady-state PCE is nearly identical to the PCE extracted from the J - V -curves measured at 5 mV/s. These data confirm that the highest PCE is achieved for 0.3 % Nd-doped TiO₂. A striking difference between the undoped and doped devices is the rapid decay of the device power output. For the undoped devices, the PCE initially increases and reaches a maximum after device operation for \sim 50s, followed by a rapid decrease in the PCE. The 0.3 % and 0.5 % doped PSCs, on the other hand, remained stable for 200s after the initial PCE increase. A three hour stability test is shown in Figure 28, here the initial

Nd (%)	V_{OC} (mV)	J_{SC} (mA/cm ²)	FF (%)	PCE (%)	Stab. PCE after 30s (%)	Stab. PCE after 200s (%)
0	1129 ± 6	22.0 ± 0.1	68.9 ± 1.4	17.1 ± 0.3	17.5 ± 0.2	17.1 ± 0.1
0.3	1133 ± 6	22.3 ± 0.3	70.5 ± 1.9	17.7 ± 0.6	18.1 ± 0.3	17.9 ± 0.4
0.5	1137 ± 2	21.9 ± 0.5	67.4 ± 0.3	16.6 ± 0.3	16.9 ± 0.4	16.8 ± 0.3

Table 3: Photovoltaic parameters of Nd-doped TiO₂ averaged over 3 devices: open-circuit voltage (V_{OC}), short circuit current (J_{SC}), fill factor (FF), power conversion efficiency (PCE) and stabilized power conversion efficiency (Stab. PCE) after 30 and 200 seconds, extracted from Figure 26. The J - V characteristics were recorded at reverse bias at a scan rate of 5 mV/s across a 0.16 cm² aperture active area. The voltage at the maximum power output was extracted from the J - V -curves and devices were then held at this voltage to determine the variation of the power output efficiency with time.

rapid drop in PCE for undoped devices is again clearly shown, while it is absent for the doped devices. Such rapid losses in performance can be attributed to the UV-induced desorption of O₂ from oxygen vacancies in TiO₂, which exposes deep trap states in TiO₂, leading to a marked decrease in electronic properties. [41] This phenomenon typically occurs within the first hours of operation, which justifies the relatively short testing period. [52] On longer time scales other processes such as gold migration [50], ion migration [172] or perovskite degradation [48] start to play a role. Trivalent dopants, such as Al and Nd, have been shown to reduce the density of oxygen defects, thus inhibiting the PCE decay upon UV irradiation. [52]

In order to study the electronic properties of TiO₂ electrodes upon doping with Nd,

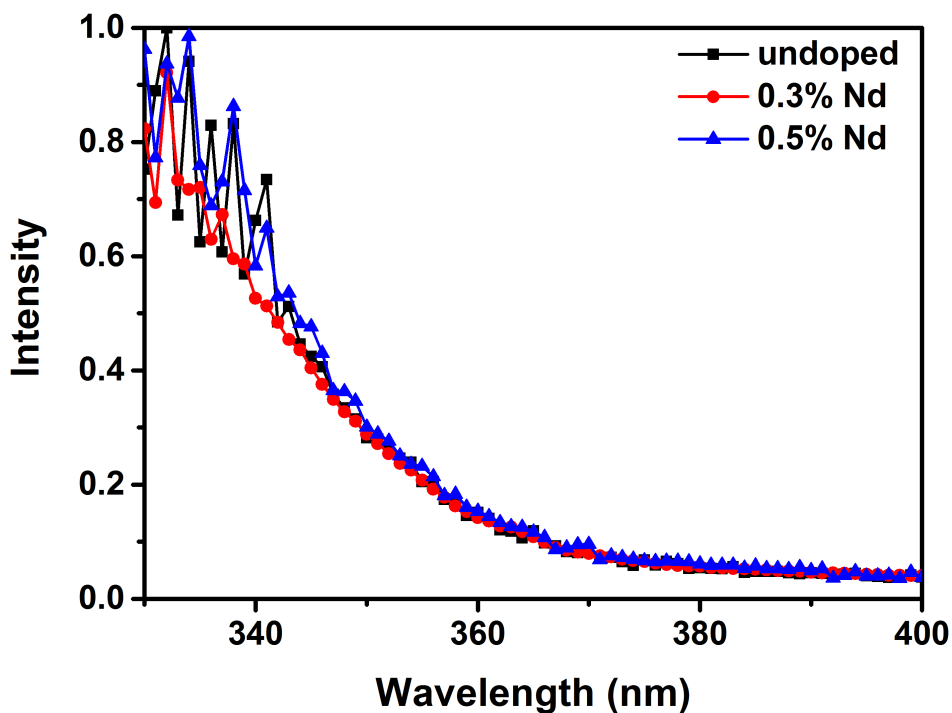


Figure 27: UV/Vis absorption spectrum of undoped, 0.3 and 0.5 % Nd-doped TiO₂.

we used IMPS [173] and IMVS. [154] In PSCs the frequency overlap for charge transport in TiO₂ and perovskite may complicate the data interpretation. In order to circumvent this problem we prepared a set of solid state DSSCs, sensitizing the Nd-doped and undoped m-TiO₂ films with Y123-dye [151] and using spiro-OMeTAD as the hole transporting material, according to a method we reported previously. [174] Electron transport lifetimes for undoped, 0.3 % Nd-doped and 0.5 % Nd-doped samples are plotted against the short circuit current in Figure 29a. A single exponential fit shows the transport lifetime evolution with the short circuit current (J_{SC}). Electron transport is faster in the doped samples compared to the undoped analogues. This is in agreement with the increased performance of 0.3 % Nd-doped devices. Faster charge transport leads to a lower series resistance, which in turn gives rise to

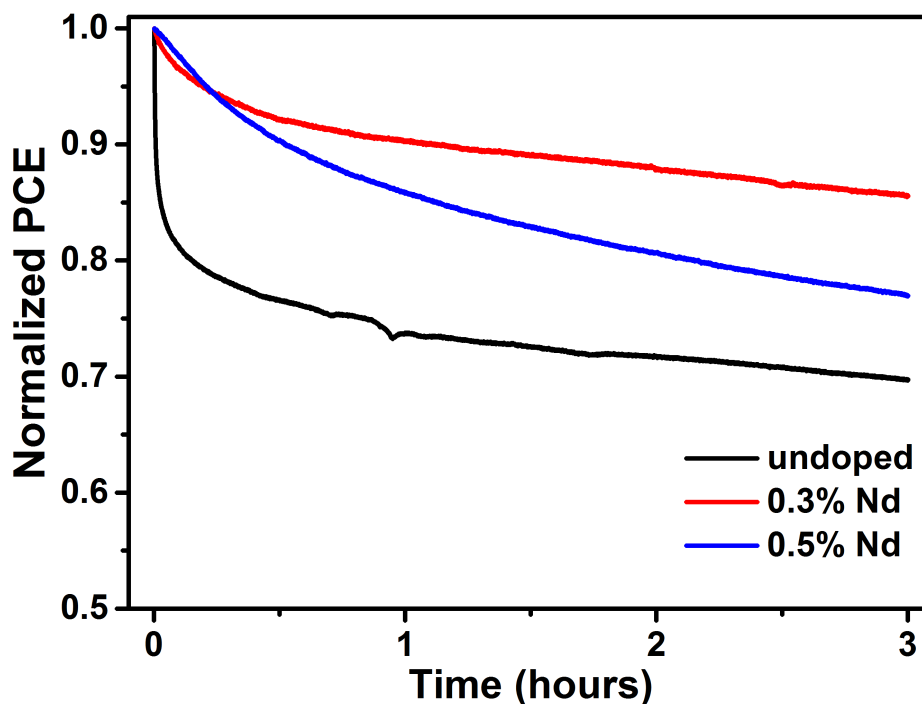


Figure 28: Stability test of undoped, 0.3% and 0.5% Nd-doped TiO₂ PSCs. The voltage at the maximum power output was extracted from the J - V -curves in Figure 25, the device was held at this voltage for 3 hours in which the PCE was determined every second. After completion of the measurement a second J - V -curve was taken to confirm that the maximum power point had not significantly changed.

the increase in the fill factor of Table 3. The effect is larger for low light intensities, again indicating a larger difference between the Nd-doped and undoped TiO₂ in deep trap state density, as deep trap states are filled at higher light intensities and contribute less to charge transport. [175] In Figure 29b, electron lifetimes are plotted against the open circuit voltage (V_{OC}) for undoped, 0.3% and 0.5% Nd-doped TiO₂ samples. Electron lifetime is increased for the doped samples, indicating that charge recombination is reduced through the elimination of deep traps, resulting

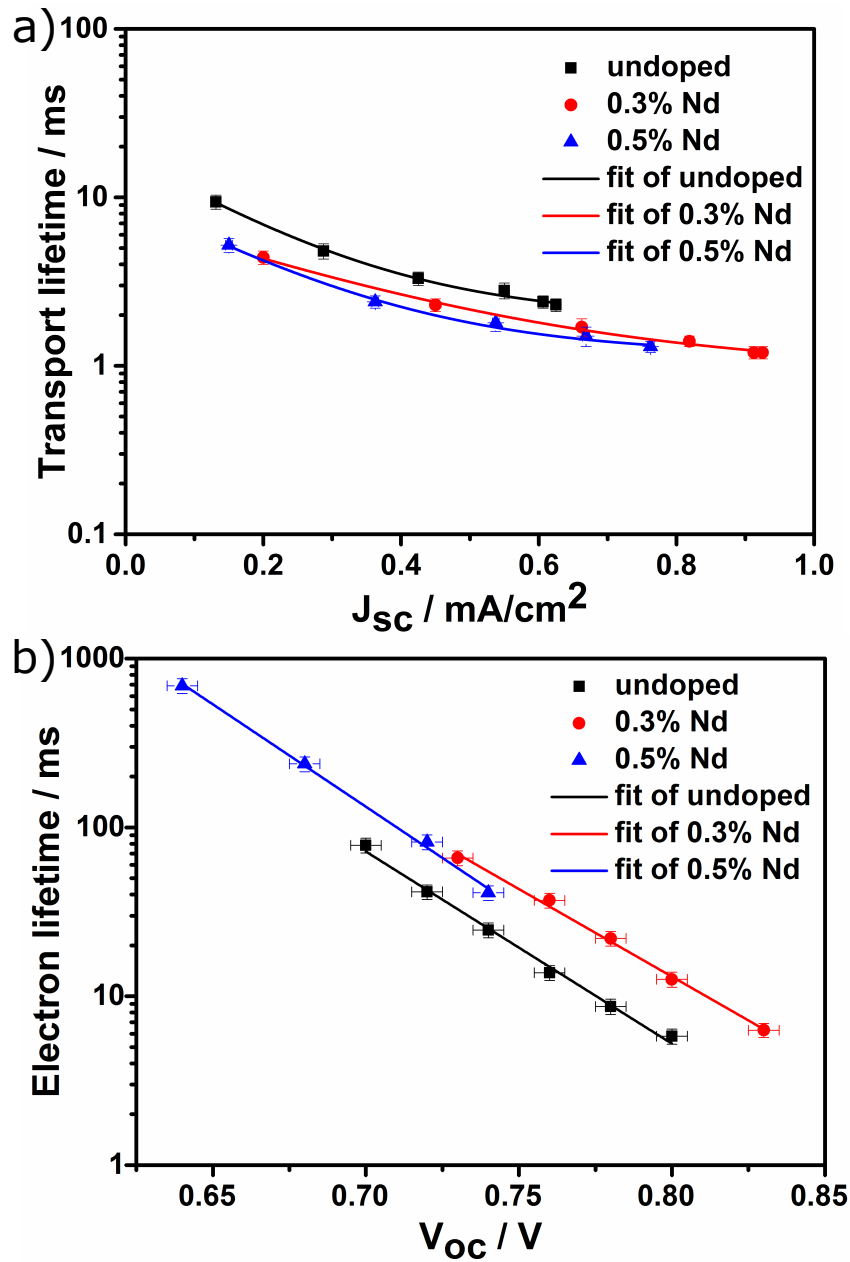


Figure 29: a) Electron transport lifetimes as a function of J_{SC} , obtained through IMPS and b) electron lifetimes as a function of V_{OC} , obtained through IMVS, for undoped, 0.3% and 0.5% Nd-doped TiO₂ in solid state DSSCs. [154,173]

in an increase of V_{OC} . For 0.5% Nd-doped samples the electron lifetime is shorter than that of 0.3% Nd-doped samples. This indicates that the interstitially incorporated Nd sites can act as recombination centres, leading to a decreased device performance. The formation of an insulating layer on the surface of TiO₂, which could not be excluded from XRD data, is unlikely as such insulating layers are usually accompanied by an increase in FF [176] and a large increase in V_{OC} , which is contrary to what is observed here.

6.4 Conclusion

Polymer assisted sol-gel chemistry was used to prepare mesoporous Nd-doped TiO₂ electrodes. SEM, XRD and PDS were employed to compare the resulting doped and undoped materials. Both interstitial and substitutional incorporation of Nd within the TiO₂ crystal lattice were observed. For 0.3% Nd content, substitutional doping was dominant. Upon increasing the doping concentration, the additional Nd ions were incorporated into interstitial sites. This was directly reflected in the PSC performance, which reached a maximum in power conversion efficiency for 0.3% Nd-doped mesoporous TiO₂ electrodes, mainly caused by an increase in the FF, and deteriorated with higher doping levels. PDS, IMPS and IMVS analysis elucidated this result by demonstrating the largest decrease in deep trap states, improved electron transport and reduced charge recombination for 0.3% Nd-doping. For 0.5% Nd-doping the deep trap state density increases again, leading to increased charge recombination and a drop in device performance. Furthermore, device power conversion efficiency was maintained under continuous illumination. PSCs prepared with Nd-doped TiO₂ electrodes have higher early-time stability compared to undoped PSCs. Indeed, the optimised doping concentration of 0.3% Nd enabled 18% stabilized power conversion efficiency for 200 s in air, while undoped devices started to show a drop in performance after reaching a maximum around 50 s. The better lifetime of the doped devices is attributed to Nd passivation of oxygen defects, which in sealed devices play an important role in PSC degradation. In difference to earlier studies of Al-doping of TiO₂, Nd-doping increased the stability of PSCs without adversely affecting the short-circuit current of the devices.

7 Stability of m-SnO₂ based PSCs and the role of the TCO

This chapter aims to investigate the stability of m-SnO₂ based PSCs compared to m-TiO₂ and planar SnO₂ PSCs. In addition, the influence of the transparent conducting oxide (TCO) on m-SnO₂ based PSCs is studied. Although m-SnO₂ has great potential as electron selective contact in PSCs, to date no devices have been shown to be able to match the efficiency achieved with m-TiO₂. This chapter investigates one possible reason for the lack in performance. Fluorine doped tin oxide (FTO) is commonly used as front electrode, but fluorine may migrate from FTO into the SnO₂ compact layer. This greatly reduces the electron selectivity of the compact layer. By replacing FTO with aluminum doped zinc oxide (AZO), this problem can be circumvented.

7.1 Introduction

The power conversion efficiency (PCE) of perovskite solar cells (PSCs) has in recent years rapidly increased from 3.8 % [22, 24, 25] to more than 22 %, now rivaling the efficiency of market reference silicon solar cells [9]. Having passed this first hurdle, it is now becoming more important to increase the stability of PSCs to pass the industry standards, i.e. a PCE loss of less than 0.5 % per year over a life span of 25 years [6]. More robust perovskites [177], metal contacts [50] and hole transporting materials [174] have been demonstrated to be quite effective to enhance the

This chapter has been published as:

Roose, B., Correa Baena, J. P., Gödel K. C., Grätzel, M., Hagfeldt, A., Steiner, U., Abate, A., "Mesoporous SnO₂ electron selective contact enables UV-stable perovskite solar cells" *Nano Energy*, **30**, 517-522 (2016)

lifetime of PSCs, even though device stability is still far from industrial standards. A major loss in PCE was found to be caused by a rapid degradation in the performance of TiO₂-based devices caused by the exposure to UV light [41], which is the most common device configuration in state-of-the-art PSCs. This performance degradation arises from the desorption of O₂⁻ that passivates deep electronic traps caused by oxygen vacancies in the TiO₂ lattice [41]. Although this effect can be significantly reduced by doping [52,150], attempts have been made to replace TiO₂ altogether [178,179]. One promising alternative inorganic material for electron selective layers (ESL) is SnO₂.

Due to the wider band-gap, SnO₂ absorbs less UV light and is thus more robust than TiO₂ under full sunlight [146]. In addition, the bulk electron mobility in SnO₂ is two orders of magnitude higher than that of TiO₂ [101], and electron injection from perovskite into SnO₂ has been shown to be more efficient than into TiO₂ [147]. SnO₂ has been successfully implemented on lab scale as ESL in low-temperature processed planar PCSs, yielding a stabilized PCE of more than 20.5 % [67,147,180]. However, the rapid and poorly controlled perovskite crystallization makes it difficult to scale up planar PSCs for industrial application. A porous ESL can overcome this problem by changing the surface wettability [181] to achieve uniform perovskite coverage over large areas [69,182]. A porous ESL has also been shown to be beneficial for electron extraction [68]. It is thus of interest to develop a mesoporous SnO₂ (m-SnO₂) ESL for the industrial production of stable and efficient PSCs. So far, the highest reported PCE for solution processed, high temperature sintered m-SnO₂ based PSCs has only been 6.5 % (not-stabilized) [183]. PSCs employing low temperature m-SnO₂ deposition have, however, reached a PCE of 12 % (not-stabilized) [69]. The deposition of a thin conformal coating of TiO₂ onto high

temperature sintered m-SnO₂ has been reported to increase the PCE to 11.9% (not-stabilized) [184]. The addition of TiO₂, however, defeats the purpose of using SnO₂ as a potentially more stable alternative.

In this study we show that m-SnO₂ PSCs are more stable than planar SnO₂ and m-TiO₂ PSCs during maximum power point tracking under continuous full sunlight illumination (no UV filtering) in an inert atmosphere. A significant hurdle, however, is the low open circuit voltage (V_{OC}) and fill factor (FF) of m-SnO₂ compared to planar SnO₂ and m-TiO₂ PSCs. We show that the origin of this behavior is the poor electron selectivity of m-SnO₂ when processed atop of fluorine doped tin oxide (FTO) as transparent conductive oxide (TCO) electrode. We have investigated two possible causes; cracking of the ESL upon heating, or fluorine migration [185]. Our data suggests that, at high temperatures, fluorine migrates from FTO into SnO₂, doping the ESL to an extent where charge selectivity is compromised and recombination is increased. To circumvent this problem we prepared m-SnO₂ PSCs using aluminum doped zinc oxide (AZO) as TCO. Moreover, AZO has good conductivity (sheet resistance $<10/\square$) and is low-cost, composed of abundant materials, easy to etch and has a high transmittance in the near-IR region [186]. Using this alternative TCO, a strong increase in PCE and a remarkable stability of m-SnO₂ based PSCs were achieved.

7.2 Experimental methods

7.2.1 Material characterization

SEM, XRD and cyclic voltammetry were performed according to Section 5.1.

7.2.2 Solar cell preparation

PSCs employing SnO₂ and CDT perovskite and DSSCs employing SnO₂ and Z907-dye were prepared according to Section 5.3.

7.2.3 Solar cell characterisation

PSCs were characterised according to Section 5.4, using current-voltage scans, maximum power point tracking and IPCE measurements. DSSCs were characterised according to Section 5.4, using IMVS.

7.3 Results and Discussion

7.3.1 Characterization of compact SnO₂

Scanning Electron Microscopy

AZO (Figure 30a) and FTO (Figure 30b) electrodes were coated with a thin compact ESL of SnO₂ by spray pyrolysis at 450 °C. On AZO, the ESL, consisting of densely packed particles, is clearly visible and therefore it is likely that this layer grows heteroepitaxially (Figure 30c). In contrast, the ESL appears to have grown epitaxially on FTO and no distinct layer can be distinguished (Figure 30d).

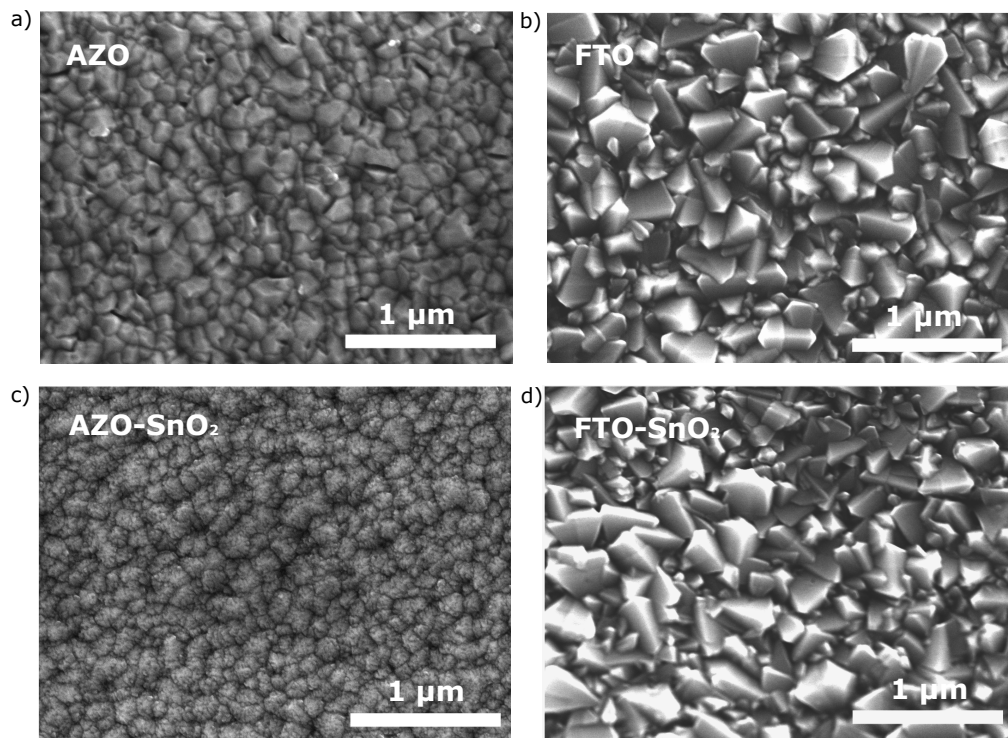


Figure 30: SEM micrographs of (a) AZO, (b) FTO, (c) SnO₂ ESL on AZO and (d) SnO₂ ESL on FTO.

Cyclic Voltammetry

To test the surface coverage and rectifying behavior of the SnO₂ ESL, cyclic voltammetry was performed in an aqueous solution of Fe(CN)₆^{3-/4-} for both FTO (Figure 31a) and AZO (Figure 31b) substrates, onto which a SnO₂ ESL was deposited by spray pyrolysis at 450 °C. The work function of the TCOs FTO and AZO are -4.7 [187] and -4.73 eV [188] respectively. The CB energy of SnO₂ is -4.25 eV [187] and the redox potential of the Fe(CN)₆^{3-/4-} redox couple is -4.68 eV [142]. As a result, SnO₂ behaves like an electrochemically silent dielectric material against the Fe(CN)₆^{3-/4-} redox couple [142](Figure 18). The charge-transfer reaction is therefore assumed to occur exclusively at the bare TCO surface. The effective TCO surface area in contact with the electrolyte can be determined by dividing the peak current of the ESL covered substrate by the peak current of the bare TCO substrate [142], yielding an effective uncovered FTO area of 60%. In contrast, the ESL covered AZO substrate exhibited an effective uncovered AZO area of <1%.

The poor apparent effective coverage of the SnO₂ ESL on FTO may have two causes; (i) thermal stresses could cause cracks/pores upon cooling and/or heating, (ii) fluorine migration from FTO to the SnO₂ ESL, making the two layers electronically equivalent. The first option is highly unlikely since the FTO and SnO₂ lattice constants match, while the wurtzite/cassiterite interface of the AZO/SnO₂ junction has a much higher lattice mismatch, which should cause a much larger strain [189]. This implies that SnO₂ on AZO should be more prone to cracking than SnO₂ on FTO, in contrast to our observation. Indeed, SEM micrographs show a conformal SnO₂ ESL on FTO and no evidence of cracking (Figure 30). Fluorine migration in SnO₂ has however been previously shown at annealing temperatures similar to this study [185, 190], which would explain the observed effects, since fluorine mi-

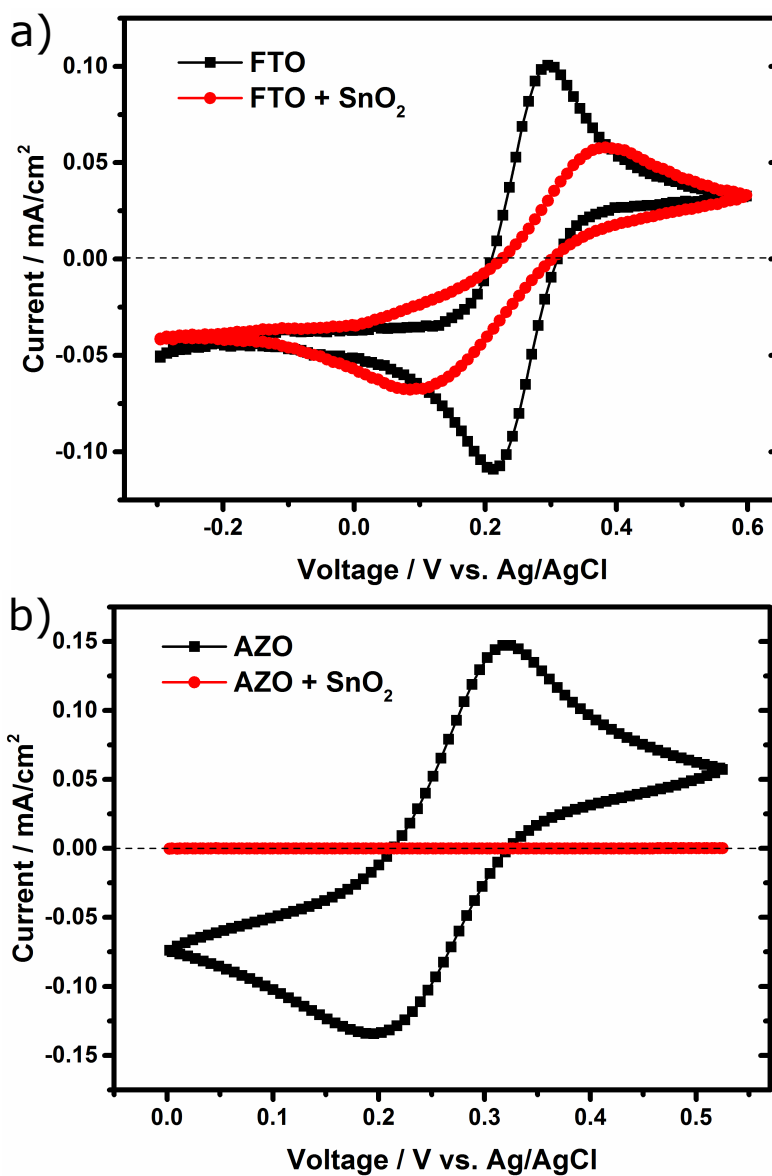


Figure 31: Cyclic voltammograms of (a) a bare FTO electrode and FTO covered by a spray coated SnO₂ ESL, (b) a bare AZO electrode and AZO covered by a spray coated SnO₂ ESL. The scan rate was 50 mV/s and the electrolyte solution consisted of 0.5 mM K₄Fe(CN)₆ + 0.5 mM K₃Fe(CN)₆ in 0.5 M aqueous KCl.

gration renders SnO₂ electronically equivalent to FTO and thereby results in a loss in electron selectivity.

Dark Current-Voltage Scan

The poor electron selectivity of SnO₂ on FTO also becomes clear from the current-voltage scan under dark conditions of a complete PSC. The presence of a large dark current is an indication that the ESL is not effectively preventing the TCO from contacting the photoactive or hole transporting layers. Figure 32 shows the minimal and maximal dark currents for a single batch of PSCs (8 devices). AZO based PSCs show a narrow dark-current distribution and overall low dark currents.

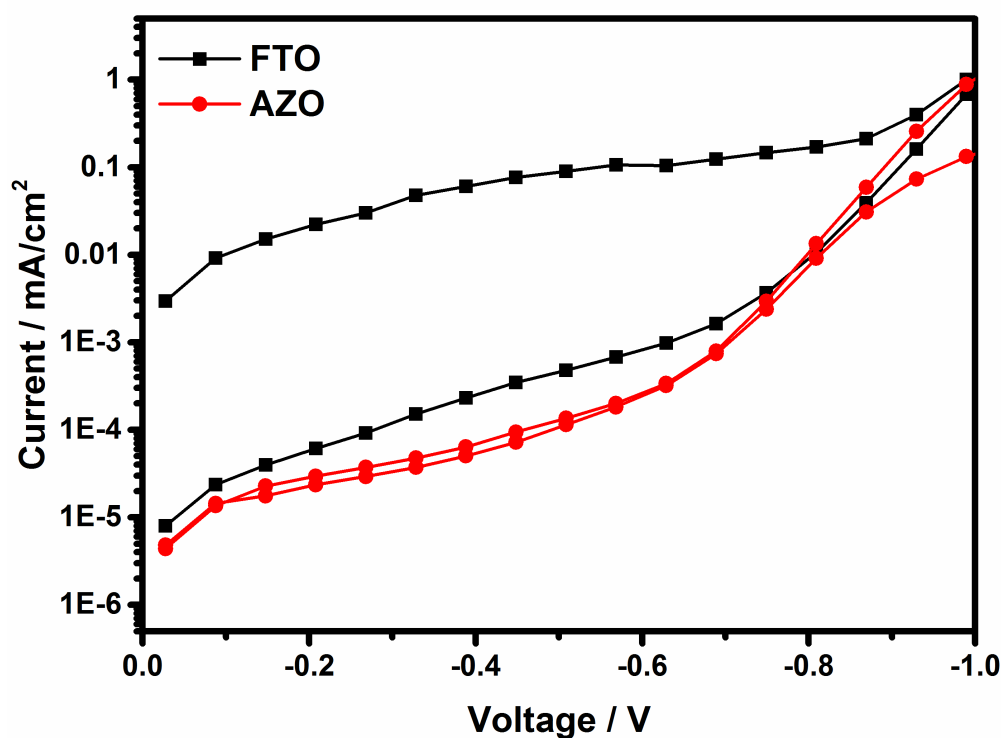


Figure 32: The minimal and maximal dark current of one batch (8 devices) of FTO and AZO based PSCs.

On the other hand, FTO based PSCs exhibit a large variation in the dark current, with high overall values.

Intensity Modulated Photovoltage Spectroscopy

The effect of the electron selectivity of SnO₂ coated TCO can be investigated by IMVS (Figure 33). Because of the overlap of the perovskite and metal oxide signals [150], dye sensitized solar cells (DSSCs) were used instead. From this measurement it becomes apparent that electron lifetimes are 2-3 times longer for DSSCs employing AZO as TCO, compared to DSSCs employing FTO as TCO, showing that recombination can be reduced by using AZO instead of FTO.

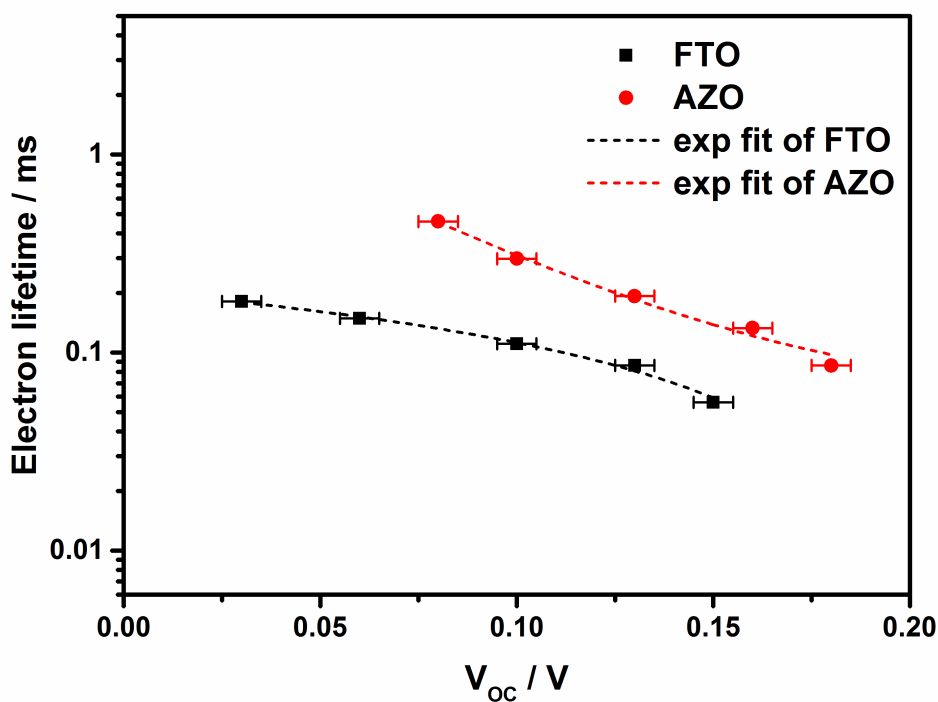


Figure 33: Electron lifetimes of DSSCs employing FTO and AZO as TCO as determined by IMVS.

7.3.2 Characterization of m-SnO₂

m-SnO₂ electrodes were synthesized via BCP assisted self-assembly [136]. The resulting films show a homogeneous coverage of the electrode by mesoporous material with a pore size of approximately 60 nm (Figure 34a). XRD showed the formation of rutile SnO₂ (Figure 34b). The average particle size was 10.9 ± 1.0 nm, calculated using the Scherrer equation [18].

7.3.3 Photovoltaic performance

The SEM micrograph in Figure 35a shows the cross section of a photovoltaic device employing AZO as the TCO, a thin SnO₂ hole blocking layer, a ~ 100 nm thick m-SnO₂ layer infiltrated and capped by the perovskite absorber, spiro-OMeTAD HTM and gold back electrode. The photocurrent-voltage (J - V) curves of the PSCs measured under AM1.5 simulated solar light (100 mW/cm^2) illumination are shown in Figure 35b. The photovoltaic parameters extracted from the J - V -curves; the open-circuit potential (V_{OC}), short-circuit current (J_{SC}), fill factor (FF), power conversion efficiency of the backward scan (PCE BW) and the stabilized power output efficiency after 300 s are shown in Table 4. IPCE spectra are shown in Figure 36. The J_{SC} values are in good agreement with those extracted from J - V curves. Since the PCE of PSCs is dependent on the way the device is measured (light and bias preconditioning, voltage scan speed and direction), additional measurements are required to verify the obtained PCE for device operation under realistic conditions [73]. By performing maximum power point tracking, a PCE value can be determined that accurately represents the efficiency of a device under real-world conditions. Device parameters clearly show a superior performance for AZO based devices owing to a higher V_{OC} and FF, resulting in an increase in stabilized PCE from 8.7% for FTO to 11.6% for AZO based PSCs (averages of 8 devices). An increase in V_{OC}

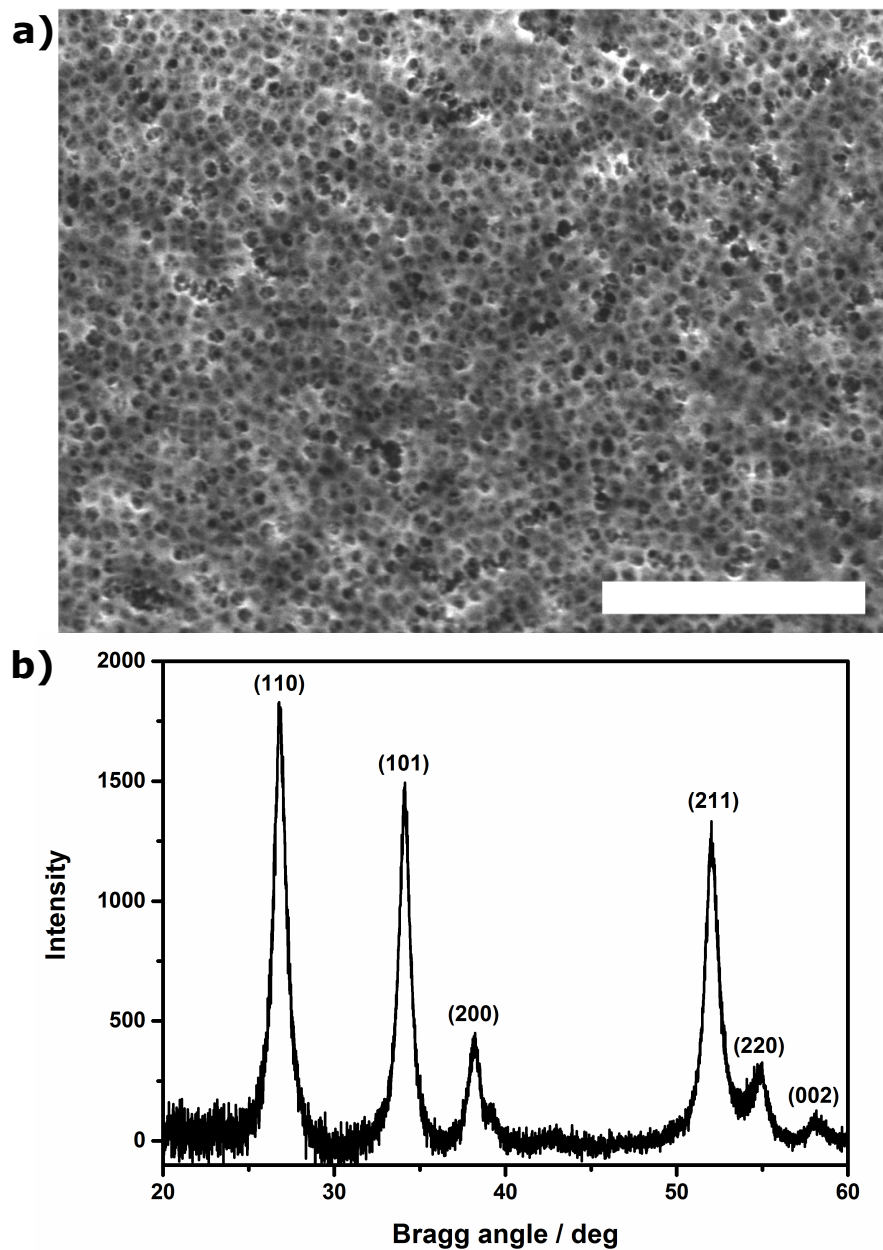


Figure 34: (a) SEM micrograph of a mesoporous SnO₂ electrode synthesized by a solution deposition process in which pore formation was controlled by the self-assembly of a BCP. (b) XRD spectrum of the mesoporous SnO₂. All peaks can be assigned to rutile SnO₂ (indexed).

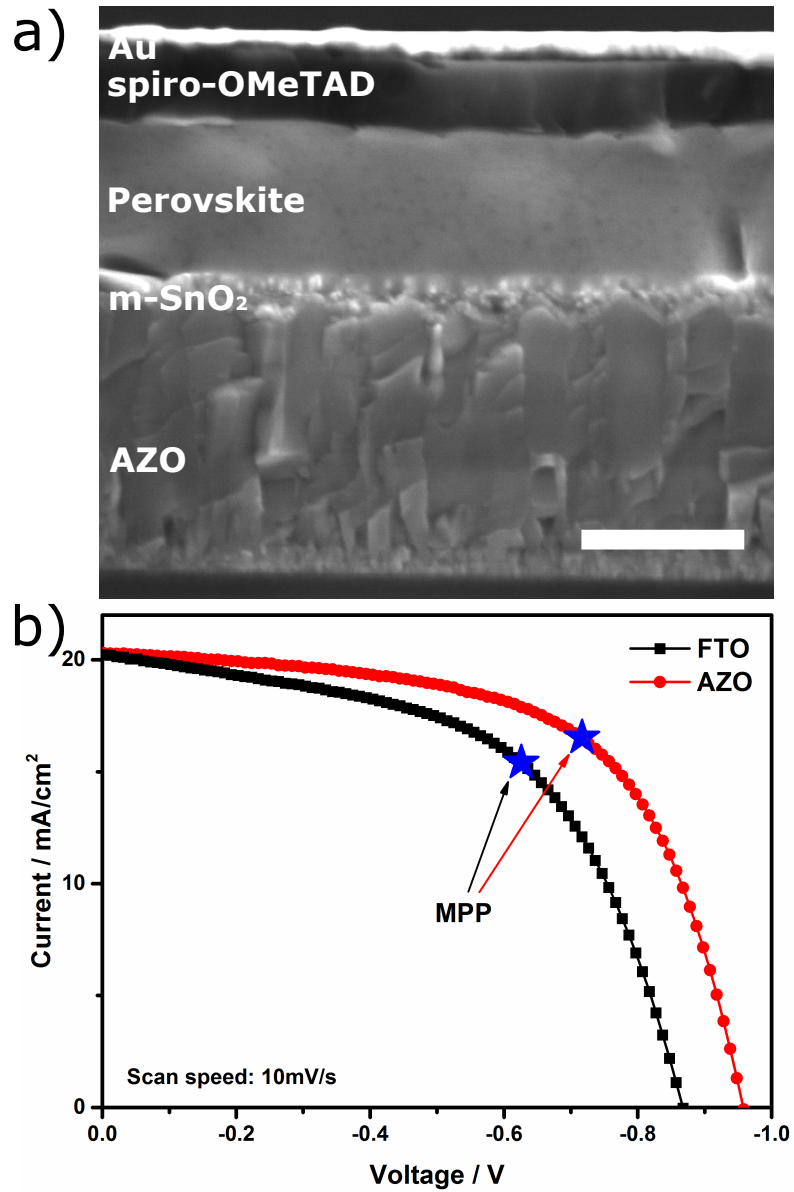


Figure 35: (a) SEM cross-section of a m-SnO₂ based PSC. (b) J - V curves for PSCs employing FTO and AZO as transparent conducting electrodes. Table 4 lists the photovoltaic parameters for the two curves.

TCO	V_{OC} (mV)	J_{SC} (mA/cm ²)	FF (%)	PCE BW (%)	Stab. PCE (after 300s) (%)
FTO average	887 ± 36	19.4 ± 0.9	56 ± 2	9.5 ± 0.8	8.7 ± 1.0
FTO best	945	20.9	58	11.4	9.9
AZO average	965 ± 16	20.2 ± 1.4	60 ± 2	11.6 ± 1.3	11.6 ± 0.7
AZO best	983	21.1	63	13.1	12.5

Table 4: Photovoltaic parameters of m-SnO₂ PSCs: open-circuit voltage (V_{OC}), short circuit current (J_{SC}), fill factor (FF), power conversion efficiency (PCE) extracted from the J - V curves in Figure 35b and stabilized power conversion efficiency (Stab. PCE) after 300 seconds of maximum power point tracking. All values are averages for 8 devices. J - V characteristics were recorded sweeping the voltage from forward bias to short circuit condition at a scan rate of 10 mV/s. Active area: 0.148 cm².

and FF is indicative of improved electron selectivity and reduced recombination at the ESL/perovskite interface, as was shown by IMVS measurements. Therefore, by replacing FTO with AZO it is possible to achieve an effective m-SnO₂ ESL.

7.3.4 Stability of PSCs

Planar SnO₂ and m-TiO₂ electrodes were prepared as previously reported [147], m-SnO₂ electrodes were prepared as described above. PSCs prepared with these electrodes were exposed to AM1.5 simulated solar light (100 mW/cm²) illumination while tracking the maximum power point for 10 hours in a nitrogen atmosphere. UV-induced degradation is a rapid degradation process, manifesting itself in the first 1-2 hours of operation [41, 52, 150], so any UV-induced degradation should be

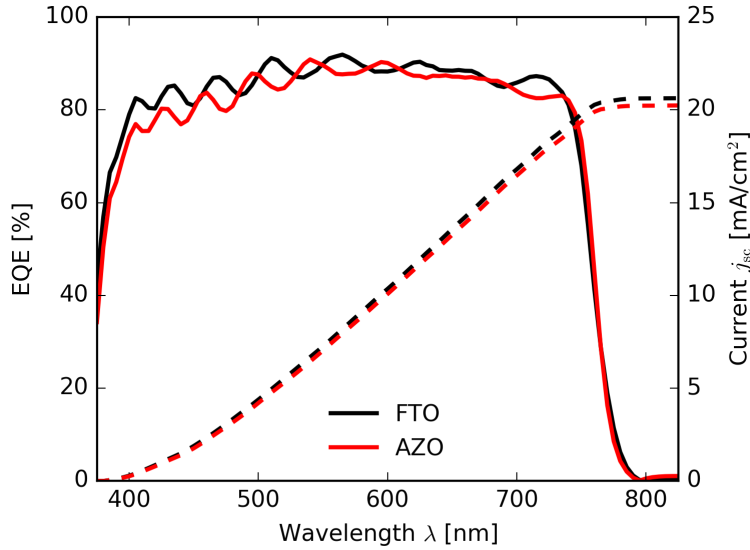


Figure 36: IPCE of FTO and AZO based m-SnO₂ PSCs.

evident in the 10 hour testing period. To exclude an effect from the TCO, all device configurations were fabricated using FTO. The result of this maximum power point tracking is shown in Figure 37a. The SnO₂-based devices show a remarkable increase over the first 1-2 hours. Previous work has shown that this can be attributed to improved electron injection from the absorber into SnO₂, by an increase in the relative density of acceptor states as a result of a CB shift, induced by charging of the SnO₂ and a rearrangement of charge species at the absorber-SnO₂ interface [191]. On the other hand, m-TiO₂ shows a rapid decay during the first hour. It is known that defects in TiO₂ can be passivated by the adsorption of atmospheric oxygen. Under the influence of UV-light oxygen desorbs, leading to a rapid decrease in performance in oxygen free conditions [150], as is observed here. Figure 37a shows that this is not the case for SnO₂-based PSCs, presumably because of the wider bandgap of SnO₂ compared to TiO₂. Another observation is that the

mesoporous device power output reaches a plateau after these initial rapid changes, whereas the planar SnO₂ keeps steadily decreasing. The mesoporous network has been reported to inhibit the degradation or phase segregation of the perovskite by providing mechanical and chemical stability, inhibiting the penetration of harmful substances such as moisture, oxygen [69], or gold [50] into the perovskite layer. A 28 day light-soaking stability test under AM1.5 simulated solar light (100 mW/cm²) illumination (>1000 ppm oxygen) is shown in Figure 37b. Again the same trend is observed, m-TiO₂ and planar SnO₂ based PSCs lose ~50% of the initial performance in the first few days, whereas m-SnO₂ based PSCs lose only ~15%. Overall, Figure 37 shows superior stability for m-SnO₂ under these conditions, combining the UV-stability of SnO₂ with the mechanical and chemical stability of a mesoporous scaffold. This proves the importance of developing efficient m-SnO₂ based PSCs.

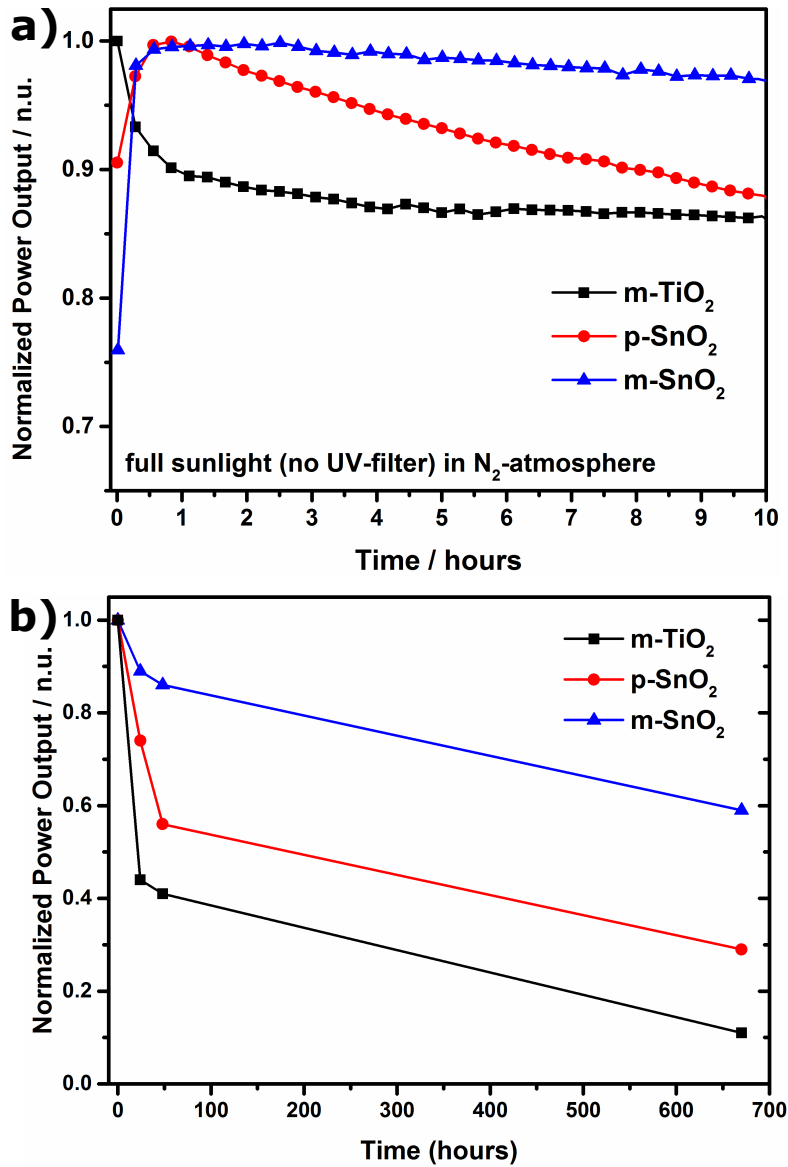


Figure 37: a) Maximum power output normalized to the maximum value for m-SnO₂, m-TiO₂ and planar SnO₂ employing PSCs exposed to AM1.5 simulated solar light (100 mW/cm²) illumination in nitrogen atmosphere. b) Stability of m-SnO₂, m-TiO₂ and planar SnO₂ employing PSCs exposed to AM1.5 simulated solar light (100 mW/cm²) illumination (>1000 ppm oxygen).

7.4 Conclusion

Highly efficient m-SnO₂-based PSCs are shown to be of critical importance to the commercial viability of PSCs, because of their increased stability compared to m-TiO₂ and planar SnO₂ PSCs. Using FTO covered by SnO₂ is however problematic because of the migration of fluorine into the SnO₂ ESL upon heating the assembly to temperatures above 450 °C. This high temperature sintering is especially important for sol-gel derived mesoporous structures, to remove organic residues and crystallise the material. The fluorine migration decreases the electron selectivity of the ESL, as it renders the SnO₂ ESL electronically equivalent to the FTO electrode. This effect was confirmed by cyclic voltammetry and dark current leakage. Cracks or pinholes were excluded as a cause for the bad behaviour of the ESL by SEM. AZO was found to be a viable alternative, circumventing the problem of fluorine migration. Mesoporous SnO₂ electrodes were fabricated through BCP self-assembly assisted sol-gel chemistry. SEM and XRD were used to confirm the formation of a porous SnO₂ electrode. Using AZO as the TCO instead of FTO resulted in a reduced recombination and in higher V_{OC} and FF values, leading to an increase in stabilized PCE from 8.7% to 11.6% (champion 13.1%), an increase of $\sim 25\%$. This is an important step towards UV-stable PSCs.

8 Highly efficient m-SnO₂ PSCs through Gallium doping

Increasing the stability of PSCs is the last remaining challenge for commercialization. It was shown in Chapter 6 that one of the major performance losses occurs upon UV-exposure of state-of-the-art TiO₂-based perovskite solar cells. In Chapter 7 it was shown that this UV instability can be solved by replacing TiO₂ with SnO₂. However, the performance of m-SnO₂ perovskite solar cells has so far not been able to rival the performance of TiO₂ based perovskite solar cells. In Chapter 7 it was shown that this was partly caused by a poor choice of electrode. Although the performance was much enhanced by employing a more suitable electrode (AZO, which is also used in this study), the performance still could not match that of TiO₂ based perovskite solar cells. In this Chapter, high efficiency m-SnO₂ perovskite solar cells were fabricated by doping SnO₂ with gallium, yielding devices that can compete with the performance of TiO₂ based devices. We found that gallium doping strongly decreases the trap state density in SnO₂, leading to a lower recombination rate. This in turn leads to an increased V_{OC} and fill factor, yielding a stabilized power conversion efficiency of 16.4%.

8.1 Introduction

Since the first report in 2009 [22], the PCE of PSCs has rapidly increased to more than 22% [9], owing to the introduction of solid state hole transporting materials [24, 25], optimized perovskite compositions [11, 28, 30] and deposition processes [31–33]. However, to become commercially viable, the long term stability of PSCs has to be greatly improved [10, 50, 174]. One of the major degradation

pathways is the rapid decrease in performance of state-of-the-art m-TiO₂ PSCs upon UV-exposure [41, 52, 150] and alternative electron transporting materials are being investigated [178, 179]. SnO₂ is an especially promising candidate, owing to the large bandgap, making the material less sensitive to UV-radiation [101]. Planar SnO₂ PSCs have rapidly caught up with m-TiO₂ based PSCs, now achieving a PCE of 20.7% [67]. However, planar SnO₂ PSCs were shown to be much less stable than m-SnO₂ PSCs, underlining the importance of highly efficient m-SnO₂ PSCs to achieve UV stability [54]. The increased stability of a mesoporous layer has been ascribed to an increased tolerance towards environmental conditions (oxygen, moisture) [56, 69] and the reduction of the negative effect of ion migration on device performance. So far, the best reported PCE of m-SnO₂ is quite poor, with a stabilized PCE of 12.5% [150]. Higher PCEs have been reached employing SnO₂ nanosheets (16.25% stabilized) [69, 192]. This structure is however very open and holds the middle ground between a planar and a truly mesoporous morphology and the resulting stability has not yet been investigated.

The main reason for the relatively low PCE compared to m-TiO₂-based PSCs is the lower CB energy of SnO₂ compared to TiO₂ [101, 147]. Since the V_{OC} depends on the energy difference between the CB of the electron transporting material and the VB of the hole transporting material, the lower CB energy of SnO₂ implies the obtainable V_{OC} is lower compared to TiO₂. Secondly, SnO₂-based PSCs tend to suffer from high recombination rates, further limiting the V_{OC} and fill factor (FF) [101]. Doping of m-SnO₂ has been shown to be an effective way to increase device performance in DSSCs [101], planar SnO₂ PSCs [193, 194], and nanosheet SnO₂ PSCs [192]. In DSSCs, gallium (Ga) was found to be one of the most promising dopants, showing impressive improvements in both V_{OC} and FF by reducing

recombination [106].

In this chapter the high recombination rate of m-SnO₂ PSCs is addressed by Ga-doping. It shows that Ga-doping greatly reduces the trap state density, leading to reduced recombination and as a result in a large increase of V_{OC} and FF. A stabilized PCE of 16.4% was achieved, rivalling the performance of m-TiO₂ PSCs made in our lab.

8.2 Experimental methods

8.2.1 Material characterization

SEM, XRD, XPS and Mott-Schottky analysis were performed according to Sections 5.1 and 5.2.

8.2.2 Solar cell preparation

PSCs employing SnO₂ and CDT perovskite and DSSCs employing SnO₂ and Z907-dye were prepared according to Section 5.3.

8.2.3 Solar cell characterisation

PSCs were characterised according to Section 5.4, using current-voltage scans, maximum power point tracking and charge extraction. DSSCs were characterised according to Section 5.4, using IMPS and IMVS.

8.3 Results and Discussion

8.3.1 Characterization of Ga-doped SnO₂

X-ray Photoelectron Spectroscopy

The incorporation of Ga was confirmed by (XPS). The full XPS spectrum of Ga-doped SnO₂ can be found in Figure 38a. A close-up of the Ga 2p_{1/2} and Ga 2p_{3/2} is shown in Figure 38b, clearly illustrating the presence of Ga. The Ga concentration was determined to be ~6 %, higher than the amount of Ga in the precursor solution (2.5 %). As XPS is a surface sensitive technique, only the top 1-2 nm of the sample are probed. This suggests that the Ga concentration is higher near the surface than in the bulk.

Crystal Structure

XRD was used to confirm the formation of rutile SnO₂. Figure 39 shows the diffractograms for undoped and 2.5 % Ga doped SnO₂. All peaks can be assigned to SnO₂ and no additional peaks are observed upon doping, indicating that the Ga ions are incorporated into the SnO₂ lattice. Because Ga³⁺ has a slightly smaller ionic radius than Sn⁴⁺ (62 and 69 pm respectively [165]) the crystal lattice is expected to contract on substitutional incorporation of Ga. This would result in a XRD peak shift to larger angles. Lattice parameters *a* and *c* can be determined using the formula for a tetragonal lattice [18] and *a* was found to decrease upon doping from 4.721 Å to 4.706 Å while *c* decreased from 3.175 Å to 3.169 Å, indicating that Ga is substitutionally incorporated in the SnO₂ lattice. The average crystallite size (*D_c*) can be calculated using the Scherrer equation [139]. *D_c* decreases from 15 ± 2 nm to 7 ± 1 nm upon doping. A reduced crystallite size is a frequently observed phenomenon in doping studies [123].

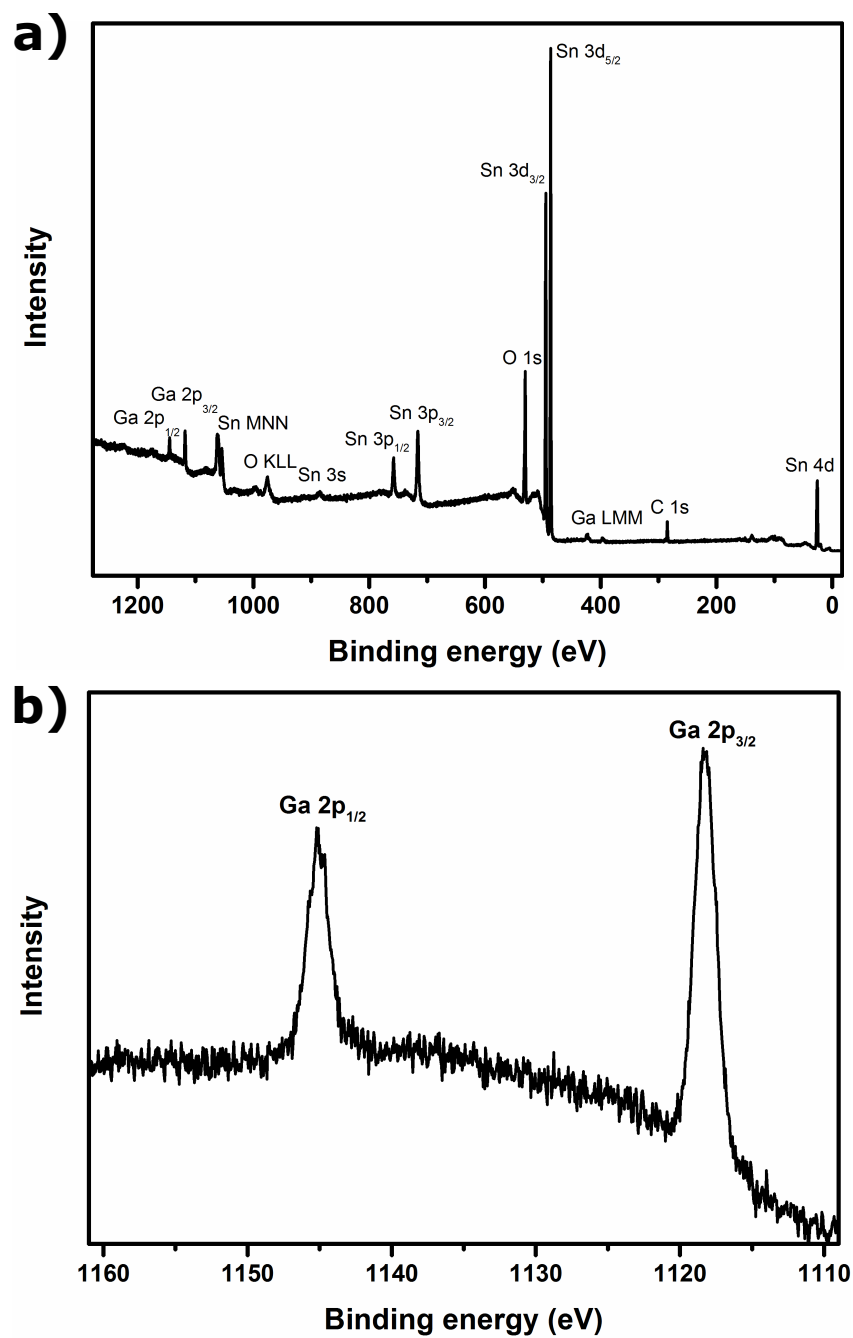


Figure 38: a) full XPS spectrum of Ga-doped SnO₂, showing the characteristic peaks for Ga and Sn. b) Close-up of the Ga 2p_{1/2} and Ga 2p_{2/3} peaks.

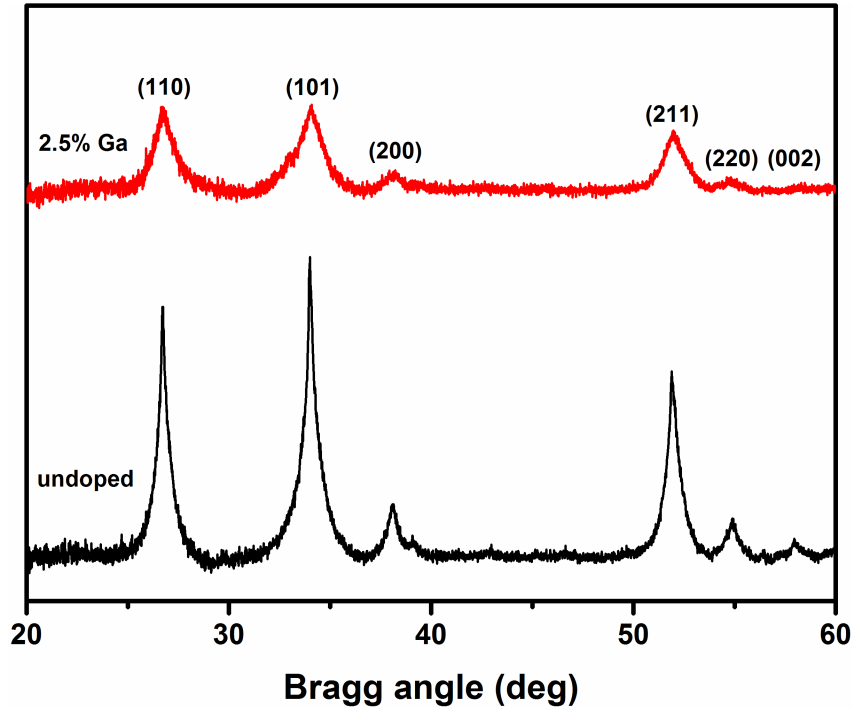


Figure 39: XRD patterns of undoped and 2.5% Ga doped m-SnO₂. All peaks can be assigned to rutile SnO₂ and a slight contraction of the lattice is observed, indicating that Ga is incorporated into the SnO₂ lattice.

Scanning Electron Microscopy

Doping metal oxides can have large effects on the morphology of the electrode [18] and doping can thus affect the metal oxide-perovskite interface area and penetration of the perovskite into the mesoporous metal oxide network. To minimize the influence of morphology on device performance, the self-assembly of the amphiphilic BCP polyisoprene-*block*-polyethyleneoxide (PI-*b*-PEO) was used to control the m-SnO₂ morphology [136,150]. SEM micrographs show mesoporous structures with similar pore sizes for undoped (54 ± 13 nm) and doped (57 ± 12) SnO₂ films (Figure 40a and 40b). The similar pore sizes indicate that the morphology is not changed

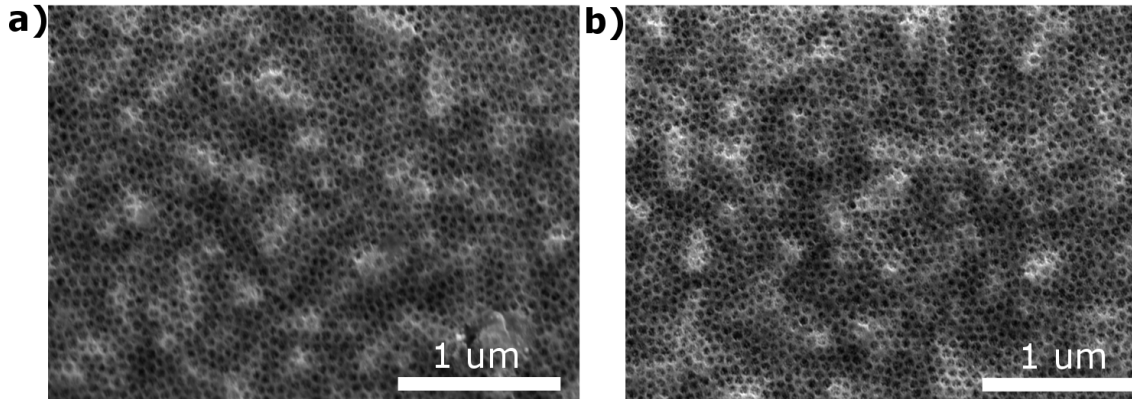


Figure 40: a) SEM micrographs of undoped m-SnO₂ and b) 2.5% Ga-doped m-SnO₂, showing identical morphologies for undoped and doped samples.

by doping and rules out an influence of morphology on device performance.

8.3.2 Solar Cell Characterization

Photovoltaic Performance

PSCs employing Ga-doped m-SnO₂ were fabricated according to literature [30, 54]. The SEM micrograph in Figure 41a shows the cross section of a photovoltaic device employing an AZO transparent conductive electrode, a compact SnO₂ ESL, 100 nm mesoporous SnO₂, a perovskite capping layer, a spiro-OMeTAD hole conducting layer and a gold back contact. The photocurrent-voltage (J - V) curves of the PSCs measured under AM1.5 simulated solar light (100 mW/cm²) illumination are shown in Figure 41b. The photovoltaic parameters extracted from the J - V -curves, the open-circuit potential (V_{OC}), short-circuit current (J_{SC}), fill factor (FF), power conversion efficiency (PCE) and the stabilized power output efficiency after 150 s are shown in Table 5 (average of 7 devices and best device). Because the obtained efficiency in PSCs is dependent on the way the device is measured (preconditioning bias

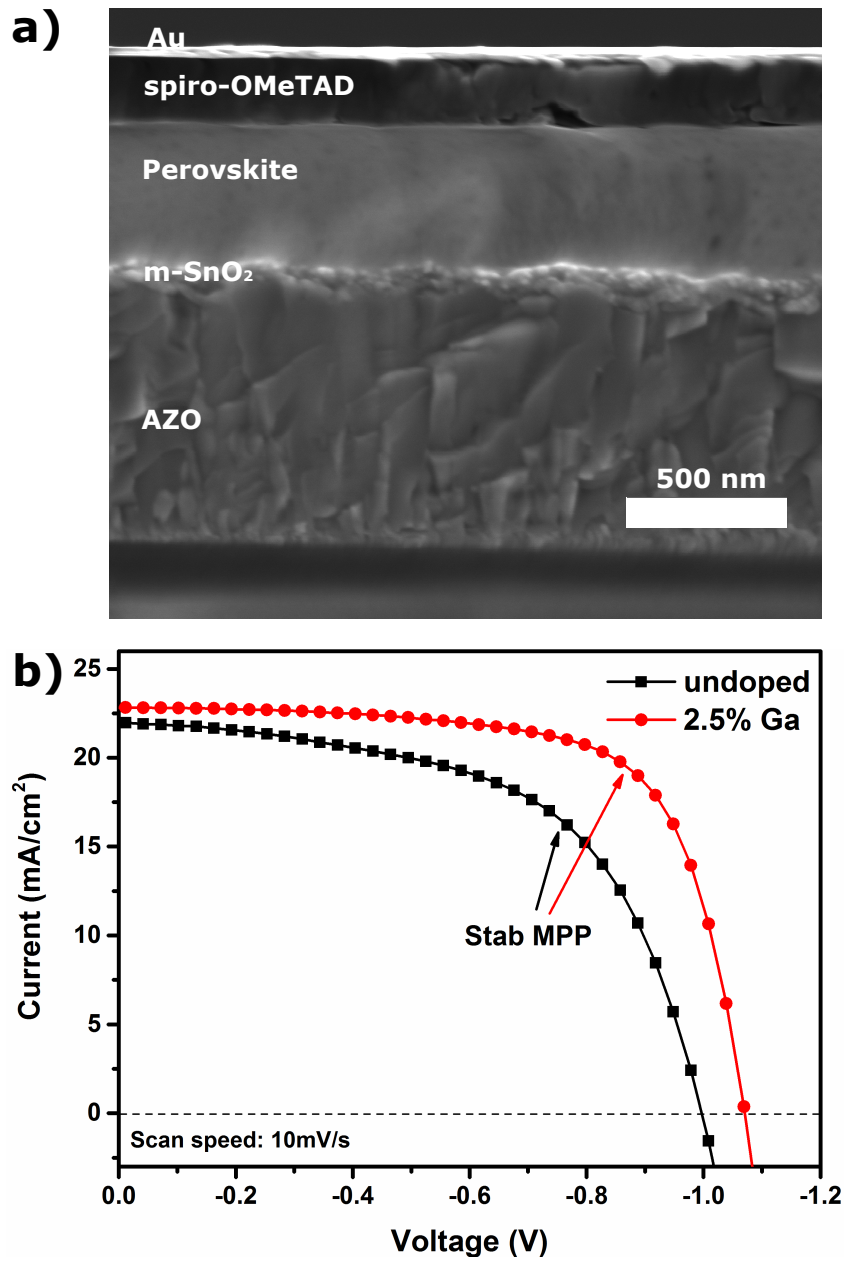


Figure 41: a) SEM cross-section of a m-ceSnO₂-based PSC. b) J - V curves for PSCs employing undoped and 2.5% Ga-doped SnO₂. The stabilized maximum power point (Stab MPP) is indicated with an arrow for each curve.

8 Highly efficient m-SnO₂ PSCs through Gallium doping

Ga (%)	V_{OC} (mV)	J_{SC} (mA/cm ²)	FF (%)	PCE (%)	Stab. PCE (%)
0, average	988 ± 16	21.6 ± 0.3	57 ± 1	12.1 ± 0.3	12.2 ± 0.3
0, best	997	22.0	57	12.5	12.7
2.5, average	1061 ± 10	22.1 ± 0.4	69 ± 1	16.3 ± 0.3	15.8 ± 0.3
2.5, best	1070	22.8	70	17.0	16.4

Table 5: Photovoltaic parameters of Ga-doped SnO₂, average of 7 devices and best performing device: open-circuit voltage (V_{OC}), short circuit current (J_{SC}), fill factor (FF), power conversion efficiency (PCE) extracted from the J - V curves in Figure 41b and stabilized power conversion efficiency (Stab. PCE) after 150 seconds. The J - V characteristics were recorded scanning from forward bias to short circuit conditions at a scan rate of 10 mV/s across a 0.09 cm² aperture active area. The voltage at the maximum power output was extracted from the J - V -curves and devices were then held at this voltage to determine the variation of the power output efficiency with time.

(light and voltage), voltage scan speed and direction) it is necessary to determine the efficiency by an additional method. By determining the maximum power point and keeping the system at the corresponding voltage for extended periods of time, a PCE value can be determined that resembles the PCE of a device under real world working conditions [73]. PCE values show an increase of ~25% upon Ga-doping, which can be attributed mainly to an increase in V_{OC} and FF. To further investigate the origin of this increase in device performance several (opto-)electronic measurements were performed; Mott-Schottky analysis on m-SnO₂ electrodes to investigate the CB energy and density of free charges, charge extraction measurements on com-

plete PSCs to probe trap state density and IMVS and IMPS on DSSCs (because of the overlapping signals of perovskite and the electron transporting material [195]) to find the electron transport lifetime and recombination rate.

Mott-Schottky analysis

Mott-Schottky analysis (Figure 42a) was used to reveal changes in the CB energy. V_{FB} is the external voltage for which no band bending occurs and corresponds to the intersect of the linear part of the curve with the x -axis [145]. As the severity of the band bending depends on the CB position, a V_{FB} shift is indicative of the relative position of the CB. Figure 42a shows that the V_{FB} is not significantly shifted upon doping. The observed ~ 70 mV increase in V_{OC} from J - V device measurements is thus not caused by a CB shift and may be attributed to reduced recombination instead. Because of the small CB shift, the electron injection efficiency from the perovskite absorber into SnO₂ is not expected to change and have an effect on J_{SC} .

The slope of the linear part of the curve in Figure 42a can be used to deduct the number of free electrons (N_e)

$$\text{Slope} = \frac{2}{\varepsilon\varepsilon_0 A^2 e N_e}, \quad (14)$$

where ε is the permittivity of free space, ε_0 the dielectric constant of the material, A the sample area and e the electronic charge. Upon doping, N_e increases from $2.5 \cdot 10^{11} \text{ cm}^{-2}$ to $6.0 \cdot 10^{11} \text{ cm}^{-2}$, which will have an effect on J_{SC} as the conductivity (σ) of the metal oxide is given by

$$\sigma = N_e \mu_e, \quad (15)$$

where μ_e is the mobility of the electrons. If the mobility is unchanged, an increase of N_e results in a higher conductivity and may have a positive effect on J_{SC} . Electron

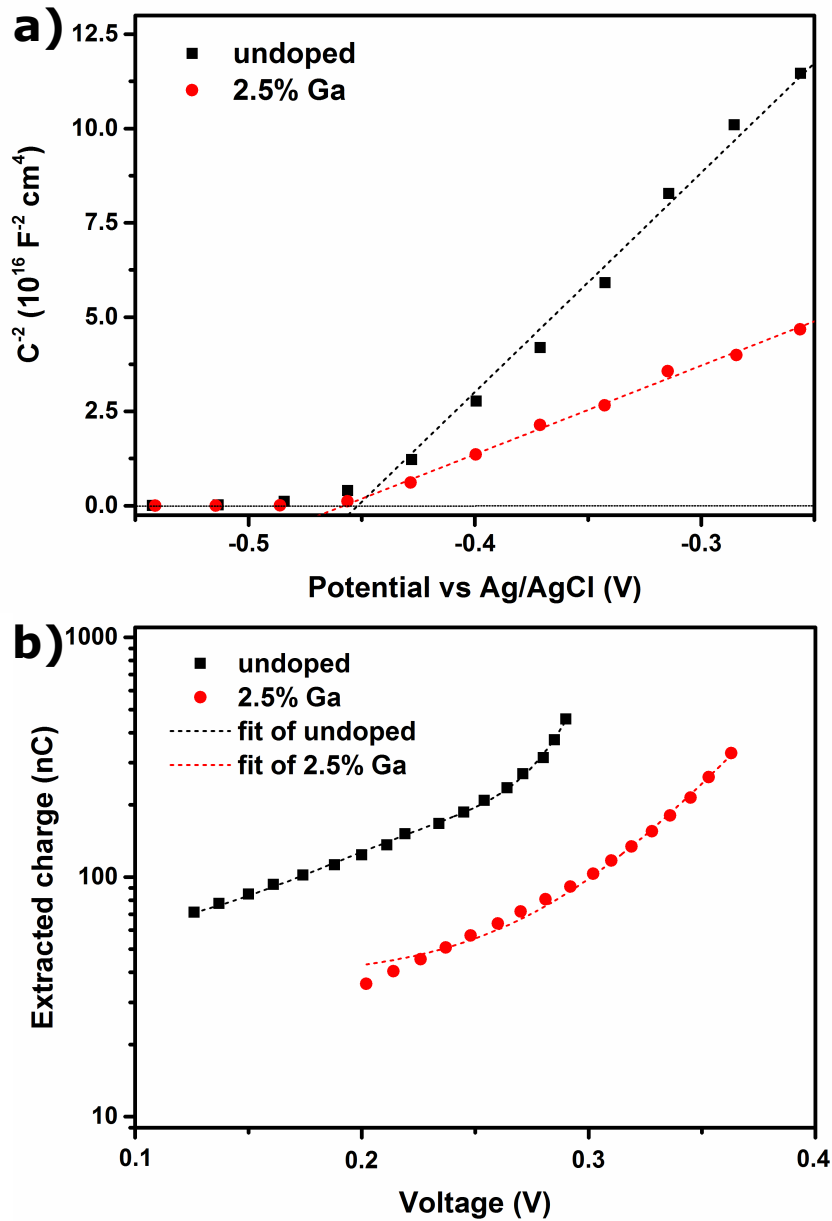


Figure 42: Optoelectronic analysis of undoped and 2.5 % Ga-doped m-SnO₂ devices; a) Mott-Schottky plot; the electrodes were submersed in a 0.5M KCl solution, with a Pt-counter electrode and an Ag/AgCl reference electrode, b) Charge extracted at open circuit as a function of voltage.

mobility is measured using IMPS (see below). The increase in N_e is somewhat unexpected, as Ga³⁺ can donate less valence electrons than Sn⁴⁺ and if Ga³⁺ were to replace Sn⁴⁺ substitutionally N_e would decrease. It is therefore likely that Ga³⁺ preferentially replaces Sn²⁺ defects, resulting in a net increase in N_e .

Charge Extraction

Charge extraction measurements were performed to quantify the trap state density of undoped and doped m-SnO₂ (Figure 42b). The cell was operated under illumination at V_{OC} , after which the illumination was switched off and the V_{OC} was allowed to decay for a set time, after which the cell was switched to short circuit and the remaining charge was collected. The amount of charge left in the cell at a certain voltage is directly proportional to the number of energy states at this voltage [195]. Because these energy states are below the CB they act as electron traps and have a detrimental effect on device performance by acting as recombination centres and slowing down charge transport. Figure 42b clearly illustrates the drastic reduction of trap states upon doping as much less charge is collected for similar voltages below the bandgap. It is therefore likely that recombination is reduced and electron mobility increased.

Intensity Modulated Photovoltage Spectroscopy

Because the observed increase in V_{OC} cannot be exclusively explained by a shift of the CB of SnO₂, IMVS was performed to determine the recombination lifetime of undoped and Ga-doped m-SnO₂ devices (Figure 43a) [154]. Because electron transport and recombination in metal oxides and perovskite have similar lifetimes [195], DSSCs were used for IMPS and IMVS measurements instead. Figure 43a shows an order of magnitude reduced recombination for Ga-doped m-SnO₂ based

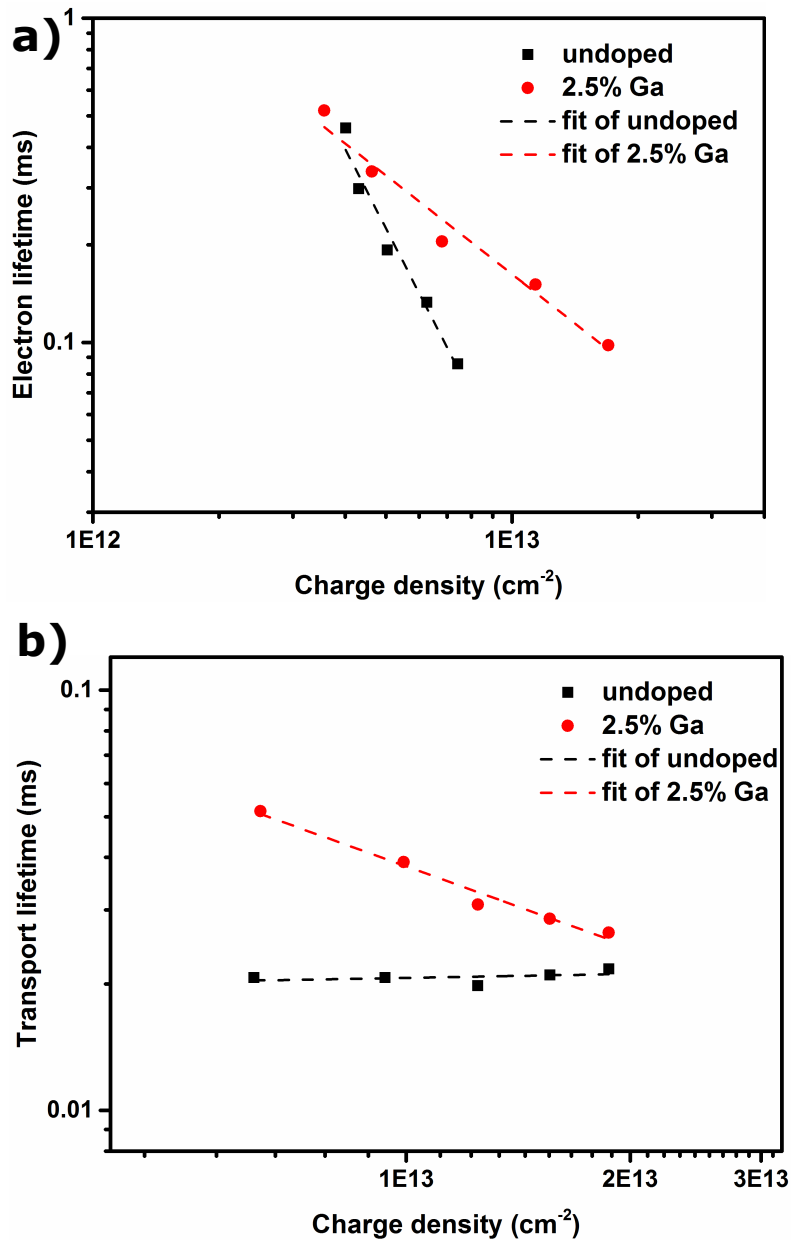


Figure 43: Optoelectronic analysis of undoped and 2.5 % Ga-doped m-SnO₂ DSSCs; a) Electron lifetime as a function of charge density, obtained through IMVS, b) Electron transport lifetimes as a function of charge density, obtained through IMPS. IMPS and IMVS data are well fit by a single exponential function.

DSSCs, which is largely responsible for the observed increase of V_{OC} . Similarly the decreased recombination rate results in a reduced shunt resistance and an increase in FF. The decreased recombination rate is likely to be a result of the lower trap state density in Ga-doped m-SnO₂ devices. A second possibility may be the formation of a thin charge barrier layer at the surface of SnO₂, as XPS data showed a higher concentration of Ga near the surface. Such thin charge barrier layers have been reported to reduce recombination [196]. However, the different slope of the fits of undoped and 2.5% Ga-doped indicate that the recombination is reduced as a result of trap state passivation by Ga-doping [154].

Intensity Modulated Photocurrent Spectroscopy

The charge transport rate was determined by IMPS (Figure 43b). Electron transport is faster for undoped devices at low current densities, which indicates a reduced injection of electrons after incorporation of Ga. This reduced injection may be the result of a charge barrier layer at the surface of SnO₂ [196]. However, the curves are converging at high current densities and electron transport rates are very similar for current densities commonly achieved in PSCs (~ 20 mA/cm²). The increased mobility of electrons in Ga-doped m-SnO₂ at high current density is a result of the reduced deep trap state density compared to undoped m-SnO₂. As the mobility is unchanged upon doping and the number of free electrons increases, the conductivity of Ga-doped SnO₂ is higher than that of undoped SnO₂ (Equation 15), which can contribute to an increase in J_{SC} .

8.4 Conclusion

The self-assembly of a BCP was used to direct the structure of mesoporous Ga-doped SnO₂ electrodes prepared through sol-gel chemistry. SEM and XRD were employed to compare the resulting doped and undoped materials. Although the average crystal size is reduced upon doping, SEM showed the morphology does not significantly change upon doping. XRD and XPS both confirmed the substitutional incorporation of Ga into the SnO₂ lattice. It was found that m-SnO₂ based devices suffer from high recombination rates, limiting V_{OC} and FF. Ga-doping eliminates deep trap states that act as recombination centers, leading to a marked increase in V_{OC} and FF. Ga-doped m-SnO₂ based PSCs were shown to reach a stabilized PCE of 16.4%, compared to 12.7% for undoped m-SnO₂ devices, showing for the first time m-SnO₂ based PSCs that can compete with state-of-the-art m-TiO₂ based PSCs. A further increase in device performance can possibly be achieved by using a dopant that shifts the CB of SnO₂ upwards, leading to a further increase in V_{OC} .

9 Coalescence of perovskite crystals

Perovskite solar cells have recently reached staggering efficiencies through efforts focused on optimizing the morphology of the perovskite films. However, intrinsic phenomena taking place in the perovskite films during storage, thereby affecting device performance, are not well understood. In this chapter we demonstrate that small crystallites within perovskite films spontaneously coalesce into larger crystals, even when complete devices are stored in the dark at room temperature. We show that crystal coalescence significantly improves the performance of state-of-the-art perovskite solar cells. Our results reveal the dynamic nature of the morphology of perovskite films and highlight the crucial role that coalescence plays in producing highly efficient devices.

9.1 Introduction

PSCs have rapidly become one of the most promising prototype technologies for low-cost and efficient harvesting of solar energy [11, 197–201]. Recent reports demonstrated outstanding solar-to-electric power conversion efficiencies (PCEs) above 22% [202]. Since the first demonstrations by Kim *et al.* [25] and Lee *et al.* [24], the main advances have been achieved through engineering the perovskite deposition, with the aim of forming a compact film with homogenous crystalline domains on the micrometre scale [197, 203]. Several reports have indicated that small crystallites present between larger perovskite domains result in suboptimal charge extraction under stabilized working conditions, such as maximum power point tracking, or in larger hysteresis under non-stabilized current-voltage (J - V) scans [180, 204]. Nevertheless, hysteresis is frequently found to decrease several hours to weeks after device preparation and it is often accompanied by an increased

stabilized PCE [40, 147, 205, 206]. Improved performance or self-healing activated by light is well documented and it has been associated with the passivation of defects within the perovskite [207, 208]. However, performance improvements have also been observed in devices stored in the dark at room temperature [204]. This is consistent with the common, and often undisclosed, practice of storing devices for several hours to a few days after the preparation, before measuring the first J - V curve [174]. The absence of any external influence suggests that a spontaneous mechanism is actively improving the devices during storage.

Here, we show that coalescence of small perovskite crystallites into larger crystalline domains takes place in perovskite films stored in dark at room temperature. SEM and XRD were employed to investigate the evolution of the perovskite film morphology. This study demonstrates that small perovskite crystallites in the film decrease in number and the average crystal size increases over the timescale of a few weeks. We have prepared state-of-the-art PSCs and used TCSPC, IMPS and photovoltaic performances to demonstrate that perovskite crystal coalescence is a spontaneous, self-healing mechanism, which is inadvertently exploited to achieve high stabilized efficiencies.

9.2 Experimental methods

9.2.1 Material characterization

SEM, XRD and TCSPC were performed according to Sections 5.1 and 5.2.

9.2.2 Solar cell preparation

PSCs employing a SnO₂ compact layer deposited by ALD and CDT perovskite, were prepared according to Section 5.3.

9.2.3 Solar cell characterisation

PSCs were characterised according to Section 5.4, using current-voltage scans and IMPS.

Days after preparation	Scan direction	V_{OC} (mV)	J_{SC} (ma/cm ²)	FF (%)	PCE (%)
2	FB to SC	1175	22.0	70.3	18.7
	SC to FB	1159	21.9	59.5	15.6
28	FB to SC	1176	22.7	72.5	19.3
	SC to FB	1170	22.7	70.6	18.7

Table 6: Photovoltaic performance parameters: open-circuit voltage (V_{OC}), short circuit current (J_{SC}), fill factor (FF) and maximum power conversion efficiency (PCE) extracted from the J - V curves in Figure 44, from forward bias (FB) to short circuit (SC) and *vice versa*.

9.3 Results and Discussion

9.3.1 Photovoltaic performance

State-of-the-art PSCs were prepared in an inert atmosphere, using a lead-based mixed halide (bromine and iodine) and cation (methylammonium and formamindinium) perovskite in a planar device architecture, as reported in the most recent literature [67]. Figure 44 displays the current density-voltage (J - V) curves of the same PSC collected under identical conditions, 2 days and 28 days after preparation and storage in dry air (below 1% relative humidity) at room temperature in the dark. The corresponding device performance parameters are listed in Table 6. It is evident that hysteresis is reduced and performance has improved with storage. As previously reported, we observed the opposite trend, *i.e.* reduced performances and improved hysteresis, when J - V s were collected every day or when devices were stored in ambient light [202]. Depending on the perovskite composition, device ar-

chitecture and preparation procedure, the PCE can increase by up to 25% after a few days or weeks of storage in the dark. Interestingly, devices with an initial lower PCE show more improvement and they tend to come closer to the highest performing ones. Having eliminated the influences of light, water and applied voltage during storage, oxygen remains the only external agent that may potentially affect

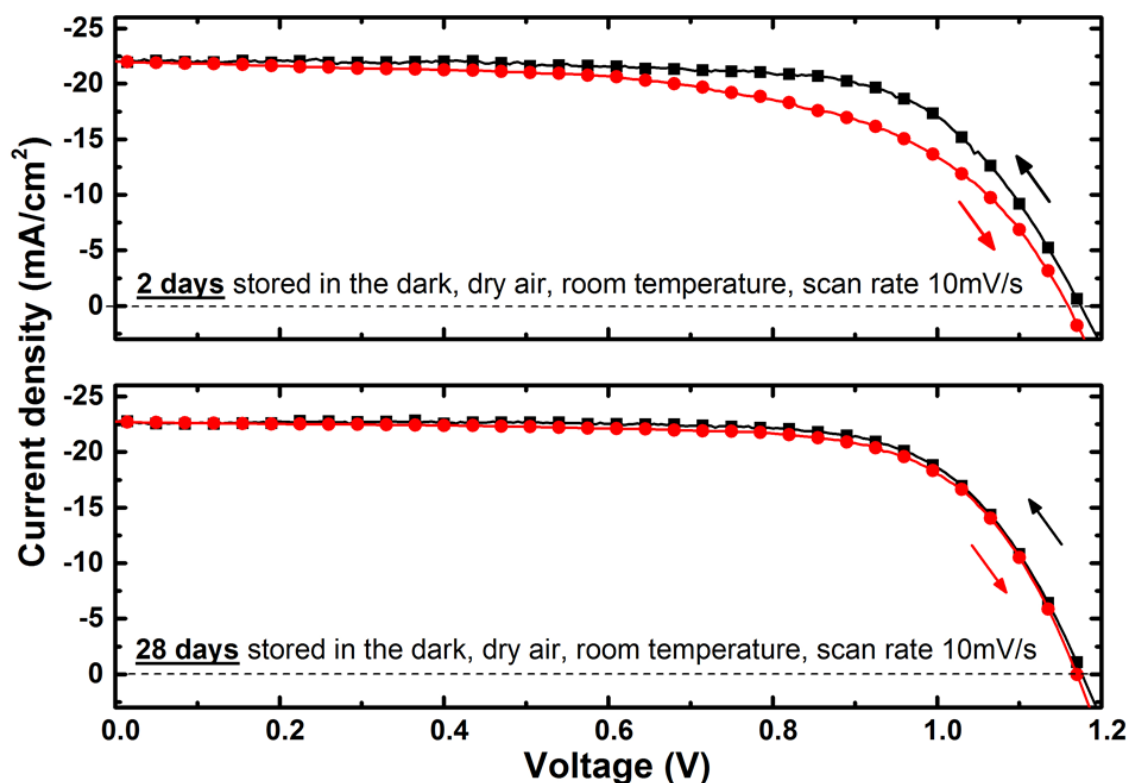


Figure 44: Current density-voltage ($J-V$) curves for PSCs stored for 2 and 28 days after the preparation, in dry air, in the dark at room temperature. The $J-V$ curves were measured at a scan rate of 10 mV/s from forward bias to short circuit condition and *vice versa* under AM1.5 simulated solar light illumination. The device was not preconditioned under light or voltage bias before each $J-V$ scan. The active area was defined by a shadow mask with an aperture of 0.16 cm².

the device performance. Oxygen is known to interact with metal oxides, organic semiconductors and the perovskite employed in these devices and modifies their electronic properties [41, 45, 56, 148, 209]. However, oxygen permeation within the device takes place on the timescale of a few hours and it is likely to saturate before the first J - V curve was collected [45]. Therefore, oxygen can be ruled out, as well as other external stimuli, which may play an important role in the improvement of PCEs during storage in the dark at room temperature.

9.3.2 Optoelectronic Characterization

To shed light on the origin of PCE improvement caused by storage in the dark, we performed IMPS on a complete device. Figure 45a shows the imaginary component frequency spectra of the current response to the light modulated intensity (10% of the stationary value) around 100 mW cm^{-2} , collected from the same device 2 and 28 days after preparation. The spectra show three main features, which have been reported earlier by Correa-Baena *et al.* [204] and Seo *et al.* [180] for similar PSCs. The low frequency feature (10^0 - 10^2 Hz) stems from the resonant frequencies of ion and ion vacancy migration within the perovskite lattice [180, 204, 210]. Here, we note that this feature is shifted towards higher frequencies or faster responses in the spectrum for the 28 day old sample. According to the study of Correa-Baena *et al.* [204], a faster ionic response is indicative of larger crystalline domains within the perovskite film. Moving to higher frequencies, there are two more features that have been assigned to the resonant frequencies of the charges within the perovskite film and the other device components, such as the hole and the electron transporting layers. While the peak at the highest frequency (10^5 Hz) is unaffected, the shoulder at 10^4 KHz is less pronounced after a long period of storage in the dark. Seo *et al.* demonstrated that this behaviour is correlated with a reduced concentration of

small crystallites within the perovskite film, which results in a better device performance [180].

To further investigate the changes in the perovskite film due to storage in the dark, we performed TCSPC measurements. Figure 45b displays decay traces measured 2 and 28 days after preparation of the perovskite film, which was deposited on a microscope slide. An exponential function was fitted to the data between 0.15 and 1.95 μs and the photoluminescence decay time was indeed found to be significantly

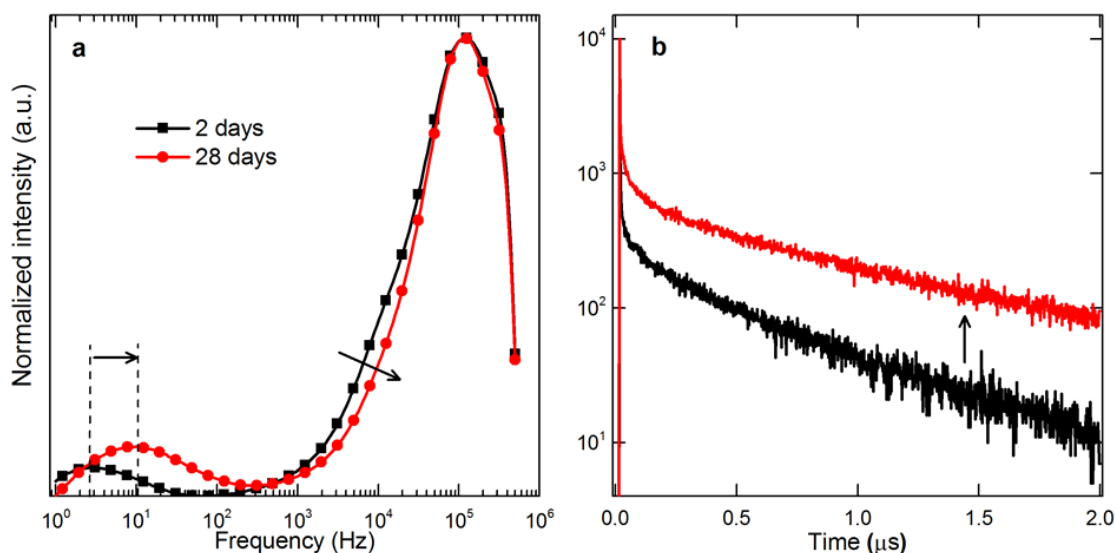


Figure 45: Data collected 2 and 28 days after the sample preparation. The samples were stored in dark and dry air at room temperature. a) Imaginary part of IMPS spectra of a complete PSC. The spectra were normalized to the highest peak at 105Hz. b)TCSPC of a perovskite film deposited on a microscope glass slide. The sample was excited at 480 nm from the perovskite side and the emission from the same side was monitored at 760 nm. The curves were normalised to the maximum signal.

longer after 28 days of storage in the dark and dry air (0.64 μs) compared to that after 2 days (0.45 μs). This points to a reduction in the non-radiative recombination through electronic defects or trap states within the perovskite film [211], as this process is dominant at low excitation densities such as in this study [212]. We have excluded from our experiment any external agent capable of passivating defects, such as water and light [213]. Therefore, the presence of increased crystalline domain sizes, suggested by IMPS, appears to be the most plausible explanation for the increased photoluminescence lifetime. As defects are more numerous at or near grain boundaries [214], the number of trap states is greatly reduced by enlarging the crystalline domains within the perovskite film. Therefore, the optoelectronic characterization suggests that storing the PSCs under dry conditions in the dark for a few weeks results in reduced non-radiative charge recombination and improved charge transport, which may be correlated to morphological changes in the perovskite film.

9.3.3 Film Morphology

The morphological evolution of perovskite films was studied by top view SEM analysis. The images were collected from the same film 2 days (Figure 46a) and 28 days after preparation and storage (Figure 46b) at room temperature in the dark under dry conditions. It seems that two adjacent crystals in the centre of Figure 46a have merged into a larger single crystalline domain in Figure 46b, eliminating one grain boundary. To show the statistical relevance of this effect, the distribution of grain areas (Figure 46c) was extracted from larger SEM top view images (Figure 46d and e). A statistical analysis revealed a significant reduction in the number of small crystallites (*i.e.* $<0.025 \mu\text{m}^2$) by about 66 % per surface area, approximately doubling the average crystal size after long storage.

This observation is attributed to the phenomenon of coalescence, where adjoining crystals fuse to form larger crystals. This phenomenon has been reported to take place in thin films of various materials including metals [215,216] and polymers [217] during processes such as aging and sintering [218]. Solvent annealing [219,220] and Ostwald ripening [221] were systematically exploited to increase the average crystal size and thus the photovoltaic performance in PSCs [197]. Recently, Sheng et

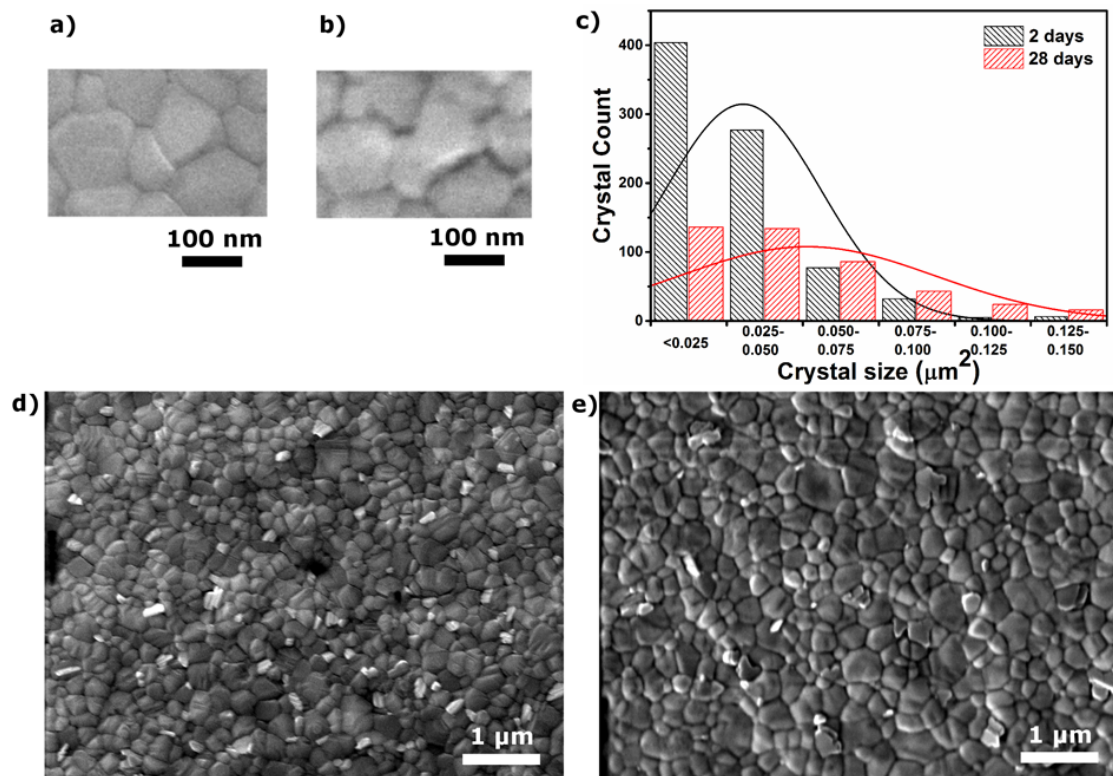


Figure 46: SEM analysis of a perovskite film stored for a) 2 and b) 28 days in dark and dry air at room temperature. c) Statistical distribution of the area of the crystalline domains from the SEM top view in d) 2 days after preparation and e) 28 days after preparation.

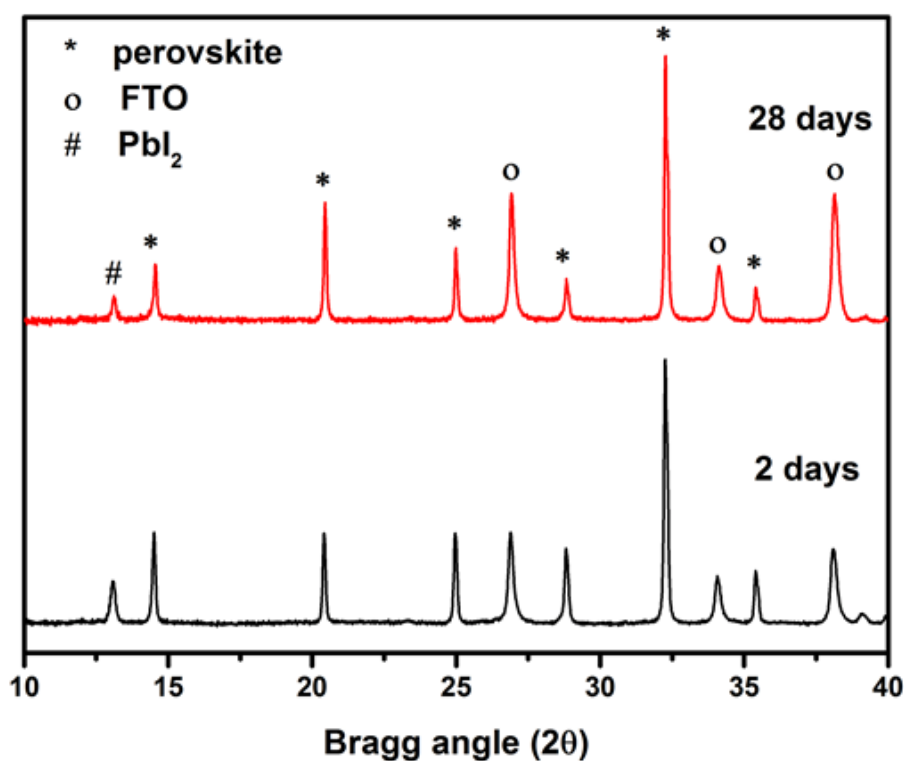


Figure 47: XRD patterns collected 2 and 28 days after perovskite film preparation. The samples were stored in the dark and dry air at room temperature.

al. also reported spontaneous increase of the average crystal size in $\text{CH}_3\text{NH}_3\text{PbBr}_3$ perovskite films stored in the dark at room temperature, but a potential impact on PSCs performance remained unexplored [222].

In order to study the changes in the crystallinity of the film, XRD measurements of the perovskite film 2 and 28 days after preparation, were conducted and are shown in Figure 47. All peaks can be assigned to the tetragonal perovskite structure, PbI_2 excess in the perovskite film and FTO from the substrate [223]. The Miller indices, FWHM values, the relative intensity of the peaks and the extracted crystal sizes are

Angle (θ)	hkl	FWHM	FWHM	Intensity	Intensity	Size	Size
		2 days (θ)	28 days (θ)	2 days	28 days	2 days (nm)	28 days (nm)
14.5	002, 110	0.12	0.11	0.34	0.21	69	74
20.4	112, 020	0.12	0.11	0.34	0.44	72	77
25.0	022	0.13	0.12	0.34	0.27	64	73
28.8	004, 220	0.15	0.15	0.28	0.16	57	57
32.3	114, 222, 130	0.15	0.14	1.00	1.00	57	61
35.4	024, 132	0.16	0.16	0.20	0.12	53	76

Table 7: Miller indices (hkl), full width at half maximum (FWHM), peak intensity normalized to the intensity of the perovskite peak at 32.3 θ and crystal size extracted from the spectra in Figure 47.

given in Table 7. The FWHM of most of the perovskite peaks decreased slightly after storage, which points towards an increase in the average crystal size [139]. The average domain size of perovskite crystals was extracted 2 and 28 days after preparation, using the Scherrer equation [139]. For most of the crystal orientations shown in Table 7, the domain size increased after storage in the dark. Considering the (022) reflection, the corresponding domain size increased by approximately 9 nm, while for most other orientations the increase was about 3-5 nm.

9.3.4 Thermodynamics of Coalescence

The grain-grain orientation is of importance for coalescence, since the surface energy associated with each grain boundary varies based on the crystallographic misorientation between the contacting faces [218]. If the degree of misorientation at the

grain boundary is low, the boundary energy is also low and these crystals preferentially coalesce, as shown in the schematic in Figure 48a and 48c. On the other hand, a high degree of misorientation at the grain boundary, as shown in Figure 48b and 48d, is unfavourable for coalescence. This explains the directional selectivity of coalescence shown in Table 7. On this basis, we distinguish coalescence from the Ostwald ripening phenomena reported in literature [221,224], which also causes the average size of perovskite crystals to increase. Ostwald ripening involves the

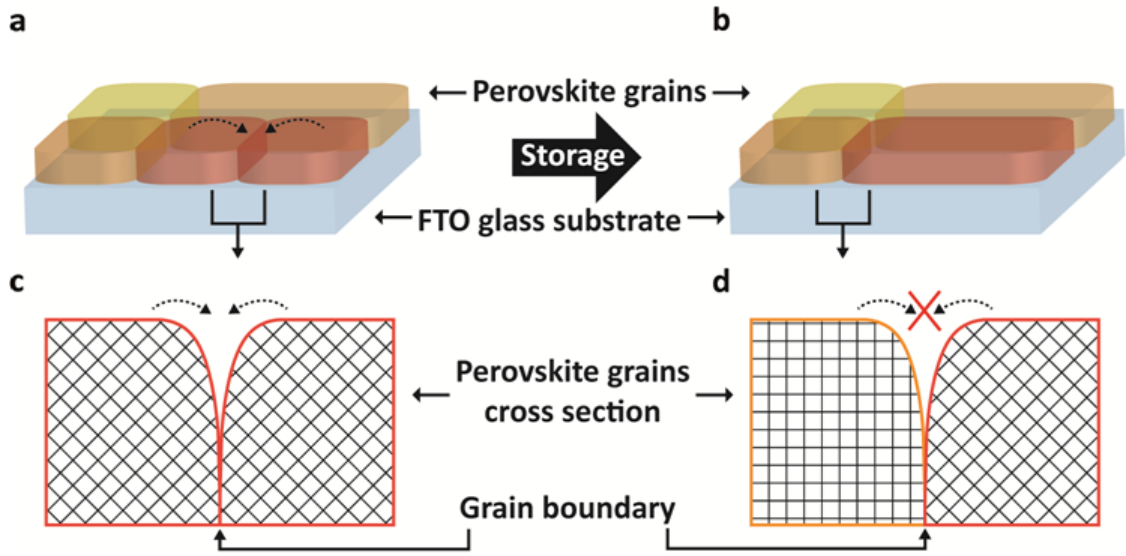


Figure 48: Schematic of crystal coalescence in a perovskite film. a) An as-prepared film of crystals with a small crystallographic misorientation at the grain boundary shown in red. Arrows indicate the grain boundary of interest between these crystals. b) Film after dark storage, showing the coalescence of these crystals. c) Cross sectional view of crystals with a small crystallographic misorientation at the grain boundary which preferentially coalesce. d) Cross sectional view of crystals with a large crystallographic misorientation at the grain boundary which do not coalesce.

transfer of material from the smaller crystals to the larger ones through an external phase which acts as a transfer medium (for instance, 2-propanol solution [221]). In contrast, coalescence involves the selective fusion of adjacent crystals by removing a connecting grain boundary.

9.4 Conclusion

Using XRD and SEM it was shown that perovskite crystals in PSCs stored in dark and dry conditions at room temperature can spontaneously coalesce, indicating that perovskite films within complete devices are highly dynamic. TCSPC indicates that this coalescence brings about a reduction in the number of grain boundaries and the associated trap states, which suppresses non-radiative recombination, resulting in an increased PCE and reduced hysteresis upon storage. Further evidence was provided by IMVS, ion(vacancy)-migration is greatly increased upon ageing of the device, which is indicative of larger grain sizes and has been credited for a less hysteretic behaviour of the device. This self-repair ability, which improves the electronic properties of perovskite films, provides an important insight into the success of perovskites as photovoltaic materials.

10 Conclusions

The aim of this thesis was to explore the influence of the metal oxide on the performance and stability of PSCs and using the gained knowledge to increase the stability of PSCs. Mesoporous metal oxides were synthesized through a block-copolymer templated method, allowing for excellent control over the film morphology. This way morphological considerations could be excluded when comparing different metal oxide compositions.

m-TiO₂ is the ETM of choice in many high efficiency PSCs [11, 28, 30]. However, other studies previously showed a rapid performance loss for TiO₂ based PSCs upon exposure to full spectrum solar light [41, 52], caused by the UV-induced desorption of oxygen, exposing deep trap states. A similar rapid drop in device efficiency was found in *Chapter 6*. By doping TiO₂ with Nd, the resistance of PSCs against UV-induced performance loss can be much improved. It was found that for 0.3% Nd content the stability could significantly be increased. Additionally, the PSC efficiency increased, mainly caused by a higher FF. This was due to a decrease in the deep trap state density, leading to improved electron transport and reduced charge recombination. The better lifetime of the doped devices is attributed to the Nd passivation of oxygen defects in the TiO₂ lattice. Even for an optimized doping concentration, UV-induced performance loss could not be completely prevented, indicating that TiO₂ may not be the ideal candidate for stable PSCs.

Chapter 7 investigated the use of m-SnO₂ as a more stable alternative to m-TiO₂. Due to the larger bandgap, m-SnO₂ does not show any UV-induced degradation. Remarkably, m-SnO₂ based PSCs exhibited a much improved stability compared to

planar SnO₂ based PSCs. The major downside of using m-SnO₂ in devices is the relatively low efficiency that had been achieved in PSCs employing m-SnO₂. *Chapter 7* shows that this is partly due to fluorine migration from the FTO electrode into the SnO₂ ESL, negating the hole blocking qualities of the ESL. This problem was overcome by replacing FTO with AZO, resulting in a marked increase in performance. The work in *Chapter 8* shows that it is possible to further increase the efficiency of m-SnO₂ based PSCs by Ga-doping. The number of deep trap states was drastically reduced upon doping, resulting in lower recombination rates, which in turn resulted in the improved FF and V_{OC} . The efficiency of these Ga-doped m-SnO₂ based PSCs is now comparable to the efficiency of m-TiO₂ based PSCs fabricated in our lab.

An insight into one of the underlying mechanisms for the enormous success of PSCs is given in *Chapter 9*. Upon storing perovskite films in a dark and dry environment at room temperature, perovskite crystal spontaneously coalesce, resulting in a larger average crystal size. As a consequence hysteresis and recombination are reduced, resulting in improved device performance at no extra cost.

11 Outlook

Because m-SnO₂ based PSCs have not reached efficiencies comparable to m-TiO₂ based PSCs, the system has not been studied intensively and many interesting properties remain to be explored.

A good starting point for further studies will be to investigate the influence of processing conditions (temperature, chemical environment) and interactions with light on the structure of SnO₂. As defects in the material have an enormous effect on the material properties, it is key to understand how defects are created during fabrication and operation. One key processing condition is the annealing temperature. m-SnO₂ is typically heated to $\sim 450^\circ\text{C}$ to improve the crystallinity, oxidize SnO₂ precursors and sinter nanoparticles together. However, high efficiencies have also been achieved using low temperature processed SnO₂ [147]. A recent study showed a significant increase in efficiency when tin was not fully oxidized to SnO₂, particularly showing a large increase in obtainable voltage. Another study showed a downward shift of the CB upon annealing of SnO₂ [225]. By annealing SnO₂ films at different temperatures and studying the effect on crystallinity, trap state density, elemental composition, conduction band position, electron transport and electron recombination, it will be possible to link the annealing temperature, material composition and device performance. A second factor that influences the SnO₂ composition is the chemical environment during annealing, since the oxygen content of the surrounding gas determines the degree to which SnO₂ precursors are oxidized. By controlling both temperature and oxygen concentration, SnO₂ can be synthesized with a wide variety of properties.

A second interesting feature of m-SnO₂ based PSCs is a marked increase in efficiency during the first minutes of operation (Figure 37a). This effect has been linked to a rearrangement of charged species or loss of surface oxygen [191]. However, in that study an increase in current was observed, while in this thesis it is mainly the voltage that increases. To further study this effect it will be interesting to measure trap state density and the conduction band position before and after light soaking as well as the electron transport and recombination rates. This may shed more light on the precise mechanism underlying this light induced performance increase.

Lastly, the exact origin of the improved stability of m-SnO₂ over m-TiO₂ and planar SnO₂ remains to be explored. Several explanations have been offered, such as better surface coverage of the perovskite [69], better protection against ingress of degradants [56] or ion (vacancy) migration [172]. To test these hypotheses the surface coverage can be studied using SEM. By tracking the light absorption of the perovskite, while exposing it to humidity and heat, the degradation can be monitored and compared between SnO₂ and TiO₂ and between mesoporous and planar morphologies. Recently, pseudo-mesoporous SnO₂ based PSCs have reached high efficiencies [69, 192], but no stability data was presented in these works. This does however raise the question of how much mesoporosity is required to gain the advantageous stability effects. By studying systems with a different thickness of the mesoporous layer, it should be possible to find the right balance between efficiency and stability.

References

- [1] *Key World Energy Statistics*. International Energy Agency, (2016).
- [2] *Ambient (outdoor) air quality and health*. World Health Organisation, (2016).
- [3] *World Reserves of Fossil Fuels*. BP, (2015).
- [4] *Nuclear Waste*. Greenpeace, (2016).
- [5] *Next Generation Wind and Solar Power*. International Energy Agency, (2016).
- [6] *Technology Roadmap: Solar Photovoltaic Energy*. International Energy Agency, (2014).
- [7] *Solar Energy Revolution: A Massive Opportunity*. P Diamandis, (2014).
- [8] *Understanding the Cost of Solar Energy*. Green Econometrics, (2007).
- [9] http://www.nrel.gov/ncpv/images/efficiency_chart.jpg.
- [10] Bella, F., Griffini, G., Correa-Baena, J.-P., Saracco, G., Grätzel, M., Hagfeldt, A., Turri, S., and Gerbaldi, C. *Science* (2016).
- [11] Saliba, M., Matsui, T., Domanski, K., Seo, J.-Y., Ummadisingu, A., Zakeeruddin, S. M., Correa-Baena, J.-P., Tress, W. R., Abate, A., Hagfeldt, A., and Grätzel, M. *Science* **354**, 206–209 (2016).
- [12] https://sites.google.com/site/chempendix/em_spectrum.
- [13] CC BY-SA 3.0, <https://commons.wikimedia.org/w/index.php?curid=2623187>.
- [14] Nelson, J. *The Physics of Solar Cells*. Imperial College Press, (2003).
- [15] inductiveload - Based on Image:BandGap-Comparison-withfermi-E.PNG by User:S-kei. Modified to read "valence" and "conduction" bands, "band gap" and redrawn to match Image:Energy_band_diagram.svg., CC BY-SA 2.5, <https://commons.wikimedia.org/w/index.php?curid=1149565>.
- [16] Shockley, W. and Queisser, H. J. *Journal of Applied Physics* **32**(3), 510–519 (1961).
- [17] Sbyrnes321 - Own work, Public Domain, <https://commons.wikimedia.org/w/index.php?curid=13252694>.
- [18] Roose, B., Pathak, S., and Steiner, U. *Chem. Soc. Rev.* **44**, 8326–8349 (2015).

References

- [19] Green, M. A., Ho-Baillie, A., and Snaith, H. J. *Nat Photon* **8**(7), 506–514 (2014).
- [20] Møller, C. N. *Nature* **182**(4647), 1436–1436 (1958).
- [21] Weber, D. Z. *Naturforsch.* **33b**, 1443–1445 (1978).
- [22] Kojima, A., Teshima, K., Shirai, Y., and Miyasaka, T. *Journal of the American Chemical Society* **131**(17), 6050–6051 (2009).
- [23] Im, J.-H., Lee, C.-R., Lee, J.-W., Park, S.-W., and Park, N.-G. *Nanoscale* **3**(10), 4088–4093 (2011).
- [24] Lee, M. M., Teuscher, J., Miyasaka, T., Murakami, T. N., and Snaith, H. J. *Science* **338**(6107), 643–647 (2012).
- [25] Kim, H.-S., Lee, C.-R., Im, J.-H., Lee, K.-B., Moehl, T., Marchioro, A., Moon, S.-J., Humphry-Baker, R., Yum, J.-H., Moser, J. E., Grätzel, M., and Park, N.-G. *Sci. Rep.* **2** (2012).
- [26] Etgar, L., Gao, P., Xue, Z., Peng, Q., Chandiran, A. K., Liu, B., Nazeeruddin, M. K., and Grätzel, M. *J. Am. Chem. Soc.* **134**(42), 17396–17399 (2012).
- [27] Heo, J. H., Im, S. H., Noh, J. H., Mandal, T. N., Lim, C.-S., Chang, J. A., Lee, Y. H., Kim, H.-j., Sarkar, A., K., N., Gratzel, M., and Seok, S. I. *Nat Photon* **7**(6), 486–491 (2013).
- [28] Jeon, N. J., Noh, J. H., Yang, W. S., Kim, Y. C., Ryu, S., Seo, J., and Seok, S. I. *Nature* **517**(7535), 476–480 (2015).
- [29] De Marco, N., Zhou, H., Chen, Q., Sun, P., Liu, Z., Meng, L., Yao, E.-P., Liu, Y., Schiffer, A., and Yang, Y. *Nano Letters* **16**(2), 1009–1016 (2016).
- [30] Saliba, M., Matsui, T., Seo, J.-Y., Domanski, K., Correa-Baena, J.-P., Nazeeruddin, M. K., Zakeeruddin, S. M., Tress, W., Abate, A., Hagfeldt, A., and Gratzel, M. *Energy Environ. Sci.* **9**, 1989–1997 (2016).
- [31] Burschka, J., Pellet, N., Moon, S.-J., Humphry-Baker, R., Gao, P., Nazeeruddin, M. K., and Grätzel, M. *Nature* **499**(7458), 316–319 (2013).
- [32] Liu, M., Johnston, M. B., and Snaith, H. J. *Nature* **501**(7467), 395–398 (2013).
- [33] Jeon, N. J., Noh, J. H., Kim, Y. C., Yang, W. S., Ryu, S., and Seok, S. I. *Nat Mater* **13**(9), 897–903 September (2014).

References

- [34] Wang, D., Wright, M., Elumalai, N. K., and Uddin, A. *Solar Energy Materials and Solar Cells* **147**, 255 – 275 (2016).
- [35] Berhe, T. A., Su, W.-N., Chen, C.-H., Pan, C.-J., Cheng, J.-H., Chen, H.-M., Tsai, M.-C., Chen, L.-Y., Dubale, A. A., and Hwang, B.-J. *Energy Environ. Sci.* **9**, 323–356 (2016).
- [36] Li, B., Li, Y., Zheng, C., Gao, D., and Huang, W. *RSC Adv.* **6**, 38079–38091 (2016).
- [37] Babayigit, A., Ethirajan, A., Muller, M., and Conings, B. *Nat Mater* **15**(3), 247–251 (2016).
- [38] Schmidt, T. M., Larsen-Olsen, T. T., Carle, J. E., Angmo, D., and Krebs, F. C. *Advanced Energy Materials* **5**(15), 1500569 (2015).
- [39] <http://energyinformative.org/lifespan-solar-panels/>.
- [40] Noh, J. H., Im, S. H., Heo, J. H., Mandal, T. N., and Seok, S. I. *Nano Letters* **13**(4), 1764–1769 (2013).
- [41] Leijtens, T., Eperon, G. E., Pathak, S., Abate, A., Lee, M. M., and Snaith, H. J. *Nat Commun* **4**(2885) (2013).
- [42] Zheng, L., Chung, Y.-H., Ma, Y., Zhang, L., Xiao, L., Chen, Z., Wang, S., Qu, B., and Gong, Q. *Chem. Commun.* **50**, 11196–11199 (2014).
- [43] Niu, G., Li, W., Meng, F., Wang, L., Dong, H., and Qiu, Y. *J. Mater. Chem. A* **2**, 705–710 (2014).
- [44] Niu, G., Guo, X., and Wang, L. *J. Mater. Chem. A* **3**, 8970–8980 (2015).
- [45] Aristidou, N., Sanchez-Molina, I., Chotchuangchutchaval, T., Brown, M., Martinez, L., Rath, T., and Haque, S. A. *Angewandte Chemie International Edition* **54**(28), 8208–8212 (2015).
- [46] Misra, R. K., Aharon, S., Li, B., Mogilyansky, D., Visoly-Fisher, I., Etgar, L., and Katz, E. A. *The Journal of Physical Chemistry Letters* **6**(3), 326–330 (2015).
- [47] Leong, W. L., Ooi, Z.-E., Sabba, D., Yi, C., Zakeeruddin, S. M., Graetzel, M., Gordon, J. M., Katz, E. A., and Mathews, N. *Advanced Materials* **28**(12), 2439–2445 (2016).
- [48] Ito, S., Tanaka, S., Manabe, K., and Nishino, H. *The Journal of Physical Chemistry C* **118**(30), 16995–17000 (2014).

References

- [49] Guarnera, S., Abate, A., Zhang, W., Foster, J. M., Richardson, G., Petrozza, A., and Snaith, H. J. *The Journal of Physical Chemistry Letters* **6**(3), 432–437 (2015).
- [50] Domanski, K., Correa-Baena, J.-P., Mine, N., Nazeeruddin, M. K., Abate, A., Saliba, M., Tress, W., Hagfeldt, A., and Grätzel, M. *ACS Nano* **10**(6), 6306–6314 (2016).
- [51] Matteocci, F., Cina, L., Lamanna, E., Cacovich, S., Divitini, G., Midgley, P. A., Ducati, C., and Carlo, A. D. *Nano Energy* **30**, 162 – 172 (2016).
- [52] Pathak, S. K., Abate, A., Ruckdeschel, P., Roose, B., Gödel, K. C., Vaynzof, Y., Santhala, A., Watanabe, S.-I., Hollman, D. J., Noel, N., Sepe, A., Wiesner, U., Friend, R., Snaith, H. J., and Steiner, U. *Advanced Functional Materials* **24**(38), 6046–6055 (2014).
- [53] Maeda, K. *Journal of Photochemistry and Photobiology C: Photochemistry Reviews* **12**(4), 237–268 (2011).
- [54] Roose, B., Baena, J.-P. C., Gödel, K. C., Graetzel, M., Hagfeldt, A., Steiner, U., and Abate, A. *Nano Energy* **30**, 517–522 (2016).
- [55] Fakharuddin, A., Giacomo, F. D., Ahmed, I., Wali, Q., Brown, T. M., and Jose, R. *Journal of Power Sources* **283**, 61 – 67 (2015).
- [56] O’Mahony, F. T. F., Lee, Y. H., Jellet, C., Dmitrov, S., Bryant, D. T. J., Durrant, J. R., O’Regan, B. C., Graetzel, M., Nazeeruddin, M. K., and Haque, S. A. *J. Mater. Chem. A* **3**, 7219–7223 (2015).
- [57] Chen, Y., Chen, T., and Dai, L. *Advanced Materials* **27**(6), 1053–1059 (2015).
- [58] Chen, Y., Li, B., Huang, W., Gao, D., and Liang, Z. *Chem. Commun.* **51**, 11997–11999 (2015).
- [59] Nguyen, W. H., Bailie, C. D., Unger, E. L., and McGehee, M. D. *Journal of the American Chemical Society* **136**(31), 10996–11001 (2014).
- [60] Xu, B., Huang, J., Ågren, H., Kloo, L., Hagfeldt, A., and Sun, L. *ChemSusChem* **7**(12), 3252–3256 (2014).
- [61] Xiao, J., Shi, J., Liu, H., Xu, Y., Lv, S., Luo, Y., Li, D., Meng, Q., and Li, Y. *Advanced Energy Materials* **5**(8), 1401943 (2015).

References

- [62] Liu, J., Wu, Y., Qin, C., Yang, X., Yasuda, T., Islam, A., Zhang, K., Peng, W., Chen, W., and Han, L. *Energy Environ. Sci.* **7**, 2963–2967 (2014).
- [63] Christians, J. A., Fung, R. C. M., and Kamat, P. V. *Journal of the American Chemical Society* **136**(2), 758–764 (2014).
- [64] Gholipour, S., Correa-Baena, J.-P., Domanski, K., Matsui, T., Steier, L., Giordano, F., Tajabadi, F., Tress, W., Saliba, M., Abate, A., Morteza Ali, A., Taghavinia, N., Grätzel, M., and Hagfeldt, A. *Advanced Energy Materials* **6**(20), 1601116 (2016).
- [65] Park, N.-G. *Materials Today* **18**(2), 65 – 72 (2015).
- [66] Hsiao, Y.-C., Wu, T., Li, M., Liu, Q., Qin, W., and Hu, B. *J. Mater. Chem. A* **3**, 15372–15385 (2015).
- [67] Anaraki, E. H., Kermanpur, A., Steier, L., Domanski, K., Matsui, T., Tress, W., Saliba, M., Abate, A., Gratzel, M., Hagfeldt, A., and Correa-Baena, J.-P. *Energy Environ. Sci.* **9**, 3128–3134 (2016).
- [68] Edri, E., Kirmayzer, S., Henning, A., Mukhopadhyay, S., K., G., Rosenwanks, Y., Hodes, G., and Cahen, D. *Nano Letters* **14**(2), 1000–1004 (2014).
- [69] Liu, Q., Qin, M.-C., Ke, W.-J., Zheng, X.-L., Chen, Z., Qin, P.-L., Xiong, L.-B., Lei, H.-W., Wan, J.-W., Wen, J., Yang, G., Ma, J.-J., Zhang, Z.-Y., and Fang, G.-J. *Advanced Functional Materials* **26**(33), 6069–6075 (2016).
- [70] Chen, B., M., Y., Priya, S., and Zhu, K. *The Journal of Physical Chemistry Letters* **7**(5), 905–917 (2016).
- [71] Eames, C., Frost, J. M., Barnes, P. R. F., O’Regan, B. C., Walsh, A., and Islam, M. S. *Nature Communications* **6**, 7497 (2015).
- [72] Calado, P., Telford, A. M., Bryant, D., Li, X., Nelson, J., O’Regan, B. C., and Barnes, P. R. *Nature Communications* **7**, 13831 (2016).
- [73] Snaith, H. J., Abate, A., Ball, J. M., Eperon, G. E., Leijtens, T., Noel, N. K., Stranks, S. D., Wang, J. T.-W., Wojciechowski, K., and Zhang, W. *The Journal of Physical Chemistry Letters* **5**(9), 1511–1515 (2014).

References

- [74] Leung, D., Fu, X., Wang, C., Ni, M., Leung, M., Wang, X., and Fu, X. *ChemSusChem* **3**(6), 681–694 (2010).
- [75] Rauf, M., Meetani, M., and Hisaindee, S. *Desalination* **276**(1&2), 13 – 27 (2011).
- [76] Park, H., Park, Y., Kim, W., and Choi, W. *Journal of Photochemistry and Photobiology C: Photochemistry Reviews* **15**(0), 1 – 20 (2013).
- [77] Chen, X. and Mao, S. S. *Chemical Reviews* **107**(7), 2891–2959 (2007).
- [78] Nah, Y.-C., Paramasivam, I., and Schmuki, P. *ChemPhysChem* **11**(13), 2698–2713 (2010).
- [79] Banerjee, A. N. *Nanotechnology, Science and Applications* **4**, 35–65 (2011).
- [80] Li, G., Richter, C. P., Milot, R. L., Cai, L., Schmuttenmaer, C. A., Crabtree, R. H., Brudvig, G. W., and Batista, V. S. *Dalton Trans.* , 10078–10085 (2009).
- [81] Kim, B.-M., Rho, S.-G., and Kang, C.-H. *Journal of Nanoscience and Nanotechnology* **11**(2), 1515–1517 (2011).
- [82] Scanlon, D. O., Dunnill, C. W., Buckeridge, J., Shevlin, S. A., Logsdail, A. J., Woodley, S. M., Catlow, C. R. A., Powell, M. J., Palgrave, R. G., Parkin, I. P., Watson, G. W., Keal, T. W., Sherwood, P., Walsh, A., and Sokol, A. A. *Nat Mater* **12**(9), 798–801 (2013).
- [83] Park, N.-G., van de Lagemaat, J., and Frank, A. J. *The Journal of Physical Chemistry B* **104**(38), 8989–8994 (2000).
- [84] Li, J., Yang, X., Yu, X., Xu, L., Kang, W., Yan, W., Gao, H., Liu, Z., and Guo, Y. *Applied Surface Science* **255**(6), 3731 – 3738 (2009).
- [85] Kim, H.-S., Lee, J.-W., Yantara, N., Boix, P. P., Kulkarni, S. A., Mhaisalkar, S., Grätzel, M., and Park, N.-G. *Nano Letters* **13**(6), 2412–2417 (2013).
- [86] Ardakani, H. *Thin Solid Films* **248**(2), 234 – 239 (1994).
- [87] Zukalova, M., Zukal, A., Kavan, L., Nazeeruddin, M. K., Liska, P., and Grätzel, M. *Nano Letters* **5**(9), 1789–1792 (2005).
- [88] Asahi, R., Taga, Y., Mannstadt, W., and Freeman, A. *Phys. Rev. B* **61**, 7459–7465 Mar (2000).
- [89] Snaith, H. J. and Schmidt-Mende, L. *Advanced Materials* **19**(20), 3187–3200 (2007).

References

- [90] Paxton, A. and Thien-Nga, L. *Physical Review B (Condensed Matter and Materials Physics)* **57**(3), 1579–1584 (1998).
- [91] Sivaram, V., Crossland, E. J. W., Leijtens, T., Noel, N. K., Alexander-Webber, J., Docampo, P., and Snaith, H. J. *The Journal of Physical Chemistry C* **118**(4), 1821–1827 (2014).
- [92] Pathak, S. K., Abate, A., Leijtens, T., Hollman, D. J., Teuscher, J., Pazos, L., Docampo, P., Steiner, U., and Snaith, H. J. *Advanced Energy Materials* **4**(8), 1301667 (2014).
- [93] Bisquert, J. *The Journal of Physical Chemistry B* **108**(7), 2323–2332 (2004).
- [94] Adachi, M., Murata, Y., Takao, J., Jiu, J., Sakamoto, M., and Wang, F. *Journal of the American Chemical Society* **126**(45), 14943–14949 (2004).
- [95] Schlichthörl, G., Park, N. G., and Frank, A. J. *The Journal of Physical Chemistry B* **103**(5), 782–791 (1999).
- [96] Franco, G., Gehring, J., Peter, L. M., Ponomarev, E. A., and Uhlendorf, I. *The Journal of Physical Chemistry B* **103**(4), 692–698 (1999).
- [97] Kopidakis, N., Neale, N. R., Zhu, K., van de Lagemaat, J., and Frank, A. J. *Applied Physics Letters* **87**(20), – (2005).
- [98] Bisquert, J. and Vikhrenko, V. S. *The Journal of Physical Chemistry B* **108**(7), 2313–2322 (2004).
- [99] Docampo, P., Guldin, S., Steiner, U., and Snaith, H. J. *The Journal of Physical Chemistry Letters* **4**(5), 698–703 (2013).
- [100] Radecka, M., Rekas, M., Trenczek-Zajac, A., and Zakrzewska, K. *Journal of Power Sources* **181**(1), 46 – 55 (2008).
- [101] Wali, Q., Fakhruddin, A., and Jose, R. *Journal of Power Sources* **293**, 1039 – 1052 (2015).
- [102] Kay, A. and Grätzel, M. *Chemistry of Materials* **14**(7), 2930–2935 (2002).
- [103] Park, N.-G., Kang, M. G., Ryu, K. S., Kim, K. M., and Chang, S. H. *Journal of Photochemistry and Photobiology A: Chemistry* **161**(2), 105 – 110 (2004).
- [104] Duan, Y., Zheng, J., Xu, M., Song, X., Fu, N., Fang, Y., Zhou, X., Lin, Y., and Pan, F. *J. Mater. Chem. A* **3**, 5692–5700 (2015).

References

- [105] Pang, H., Yang, H., Guo, C. X., and Li, C. M. *ACS Applied Materials & Interfaces* **4**(11), 6161–6265 (2012).
- [106] Teh, J. J., L., T. S., Leong, K. C., Li, J., and Chen, P. *ACS Applied Materials & Interfaces* **5**(21), 11377–11382 (2013).
- [107] Dou, X., Sabba, D., Mathews, N., Wong, L. H., Lam, Y. M., and Mhaisalkar, S. *Chemistry of Materials* **23**(17), 3938–3945 (2011).
- [108] Kim, M.-H. and Kwon, Y.-U. *The Journal of Physical Chemistry* **115**(46), 23120–23125 (2011).
- [109] Baur, W. H. *Acta Crystallographica* **9**, 515–520 (1956).
- [110] Zhou, W., Liu, Y., Yang, Y., and Wu, P. *The Journal of Physical Chemistry C* **118**(12), 6448–6453 (2014).
- [111] Maki-Jaskari, M. A. and Rantala, T. T. *Physical Review B* **64**, 075407 (2001).
- [112] King, P. D. C., Lichti, R. L., Celebi, Y. G., Gil, J. M., Vilão, R. C., Alberto, H. V., Piroto Duarte, J., Payne, D. J., Egdell, R. G., McKenzie, I., McConville, C. F., Cox, S. F. J., and Veal, T. D. *Phys. Rev. B* **80**, 081201 (2009).
- [113] Godinho, K. G., Walsh, A., and Watson, G. W. *The Journal of Physical Chemistry C* **113**(1), 439–448 (2009).
- [114] Tjong, S.-C., editor. *Nanocrystalline Materials: Their Synthesis-Structure-Property Relationships and Applications*. Elsevier, (2013).
- [115] Bates, F. S. and Fredrickson, G. H. *Physics Today* **52**(2), 32–38 (1999).
- [116] <http://research.cems.umn.edu/bates/research.html>.
- [117] Matsen, M. W. and Bates, F. S. *Macromolecules* **29**(4), 1091–1098 (1996).
- [118] Mai, Y. and Eisenberg, A. *Chem. Soc. Rev.* **41**, 5969–5985 (2012).
- [119] Alexandridis, P. and Lindman, B. *Amphiphilic Block Copolymers: Self-Assembly and Applications*. Elsevier, Amsterdam, (2000).
- [120] Cameron, N. S., Corbierre, M. K., and Eisenberg, A. *Canadian Journal of Chemistry* **77**(8), 1311–1326 (1999).

References

- [121] Kakihana, M. *Journal of Sol-Gel Science and Technology* **6**(1), 7–55 (1996).
- [122] Danks, A. E., Hall, S. R., and Schnepf, Z. *Mater. Horiz.* **3**, 91–112 (2016).
- [123] Brinker, C. J. and Scherer, G. W. *Sol-gel science, the physics and chemistry of sol-gel processing*. Academic Press, Boston, (1990).
- [124] Flory, P. J. *Faraday Discuss. Chem. Soc.* **57**, 7–18 (1974).
- [125] Smokefoot - Own work, CC BY-SA 3.0, <https://commons.wikimedia.org/w/index.php?curid=25698603>.
- [126] Hanaor, D. A. H., Chironi, I., Karatchevtseva, I., Triani, G., and Sorrell, C. C. *Advances in Applied Ceramics* **111**(3), 149–158 (2012).
- [127] Kresge, C. T., Leonowicz, M. E., Roth, W. J., Vartuli, J. C., and Beck, J. S. *Nature* **359**(6397), 710–712 (1992).
- [128] Templin, M., Franck, A., Du Chesne, A., Leist, H., Zhang, Y., Ulrich, R., Schädler, V., and Wiesner, U. *Science* **278**(5344), 1795–1798 (1997).
- [129] Simon, P. F. W., Ulrich, R., Spiess, H. W., and Wiesner, U. *Chemistry of Materials* **13**(10), 3464–3486 (2001).
- [130] Warren, S. C., DiSalvo, F. J., and Wiesner, U. *Nat Mater* **6**(2), 156–161 (2007).
- [131] Stefik, M., Wang, S., Hovden, R., Sai, H., Tate, M. W., Muller, D. A., Steiner, U., Gruner, S. M., and Wiesner, U. *J. Mater. Chem.* **22**, 1078–1087 (2012).
- [132] Stefik, M., Song, J., Sai, H., Guldin, S., Boldrighini, P., Orilall, M. C., Steiner, U., Gruner, S. M., and Wiesner, U. *J. Mater. Chem. A* **3**, 11478–11492 (2015).
- [133] Garcia, B. C., Kamperman, M., Ulrich, R., Jain, A., Gruner, S. M., and Wiesner, U. *Chemistry of Materials* **21**(22), 5397–5405 (2009).
- [134] Crossland, E. J. W., Nedelcu, M., Ducati, C., Ludwigs, S., Hillmyer, A., Steiner, U., and Snaith, H. J. *Nano Letters* **9**(8), 2813–2819 (2009).
- [135] Docampo, P., Guldin, S., Stefik, M., Tiwana, P., Orilall, M. C., HÄttner, S., Sai, H., Wiesner, U., Steiner, U., and Snaith, H. J. *Advanced Functional Materials* **20**(11), 1787–1796 (2010).

References

- [136] Guldin, S., Docampo, P., Stefik, M., Kamita, G., Wiesner, U., Snaith, H. J., and Steiner, U. *Small* **8**(3), 432–440 (2012).
- [137] Rietveld, H. M. *Journal of Applied Crystallography* **2**(2), 65–71 (1969).
- [138] Scherrer, P. *Göttinger Nachrichten Gesell.* **2**, 98 (1918).
- [139] Patterson, A. *Phys. Rev.* **56**, 978–982 Nov (1939).
- [140] Bragg, W. L. *Proceedings of the Cambridge Philosophical Society* **17**, 43–57 (1913).
- [141] Yacoubi, B., Samet, L., Bennaceur, J., Lamouchi, A., and Chtourou, R. *Materials Science in Semiconductor Processing* **30**(0), 361 – 367 (2015).
- [142] Kavan, L., Tetreault, N., Moehl, T., and Grätzel, M. *The Journal of Physical Chemistry C* **118**(30), 16408–16418 (2014).
- [143] Gödel, K. C., Choi, Y. C., Roose, B., Sadhanala, A., Snaith, H. J., Seok, S. I., Steiner, U., and Pathak, S. K. *Chem. Commun.* **51**, 8640–8643 (2015).
- [144] Sadhanala, A., Deschler, F., Thomas, T. H., Dutton, S. E., Goedel, K. C., Hanusch, F. C., Lai, M. L., Steiner, U., Bein, T., Docampo, P., Cahen, D., and Friend, R. H. *The Journal of Physical Chemistry Letters* **5**(15), 2501–2505 (2014).
- [145] Gelderman, K., Lee, L., and Donne, S. W. *Journal of Chemical Education* **84**(4), 685 (2007).
- [146] Tiwana, P., Docampo, P., Johnston, M. B., Snaith, H. J., and Herz, L. M. *ACS Nano* **5**(6), 5158–5166 (2011).
- [147] Correa Baena, J. P., Steier, L., Tress, W., Saliba, M., Neutzner, S., Matsui, T., Giordano, F., Jacobsson, T. J., Srimath Kandada, A. R., Zakeeruddin, S. M., Petrozza, A., Abate, A., Nazeeruddin, M. K., Gratzel, M., and Hagfeldt, A. *Energy Environ. Sci.* **8**, 2928–2934 (2015).
- [148] Abate, A., Leijtens, T., Pathak, S., Teuscher, J., Avolio, R., Errico, M. E., Kirkpatrick, J., Ball, J. M., Docampo, P., McPherson, I., and Snaith, H. J. *Phys. Chem. Chem. Phys.* **15**, 2572–2579 (2013).
- [149] Abate, A., Staff, D. R., Hollman, D. J., Snaith, H. J., and Walker, A. B. *Phys. Chem. Chem. Phys.* **16**, 1132–1138 (2014).

References

- [150] Roose, B., Gödel, K. C., Pathak, S., Sadhanala, A., Baena, J. P. C., Wilts, B. D., Snaith, H. J., Wiesner, U., Grätzel, M., Steiner, U., and Abate, A. *Advanced Energy Materials* **6**(2), 1501868–n/a (2016). 1501868.
- [151] Tsao, H. N., Yiâ, C., Moehl, T., Yum, J.-H., Zakeeruddin, S. M., Nazeeruddin, M. K., and Grätzel, M. *ChemSusChem* **4**(5), 591–594 (2011).
- [152] Peter, L. M., Ponomarev, E. A., and Fermin, D. J. *Journal of Electroanalytical Chemistry* **427**, 79–96 (1997).
- [153] Halme, J., Miettunen, K., and Lund, P. *The Journal of Physical Chemistry C* **112**(51), 20491–20504 (2008).
- [154] Barnes, P. R. F., Miettunen, K., Li, X., Anderson, A. Y., Bessho, T., Grätzel, M., and O'Regan, B. C. *Advanced Materials* **25**(13), 1881–1922 (2013).
- [155] O'Regan, B. and Grätzel, M. *Nature* **353**(6346), 737–740 (1991).
- [156] Malinkiewicz, O., Roldán-Carmona, C., Soriano, A., Bandiello, E., Camacho, L., Nazeeruddin, M. K., and Bolink, H. J. *Advanced Energy Materials* **4**, 1400345 (2014).
- [157] Wang, Y., Wu, D., Fu, L.-M., Ai, X.-C., Xu, D., and Zhang, J.-P. *ChemPhysChem* **16**(10), 2253–2259 (2015).
- [158] Ko, K. H., Lee, Y. C., and Jung, Y. J. *Journal of Colloid and Interface Science* **283**(2), 482–487 (2005).
- [159] Liu, J., Duan, Y., Zhou, X., and Lin, Y. *Applied Surface Science* **277**(0), 231 – 236 (2013).
- [160] Choudhury, B., Borah, B., and Choudhury, A. *Materials Science and Engineering: B* **178**(4), 239 – 247 (2013).
- [161] Wang, M., Bai, S., Chen, A., Duan, Y., Liu, Q., Li, D., and Lin, Y. *Electrochimica Acta* **77**(0), 54–59 (2012).
- [162] Zhang, C., Chen, S., Mo, L., Huang, Y., Tian, H., Hu, L., Huo, Z., Dai, S., Kong, F., and Pan, X. *The Journal of Physical Chemistry C* **115**(33), 16418–16424 (2011).
- [163] Nagaoka, H., Ma, F., deQuilettes, D. W., Vorpahl, S. M., Glaz, M. S., Colbert, A. E., Ziffer, M. E., and Ginger, D. S. *The Journal of Physical Chemistry Letters* **6**(4), 669–675 (2015).

References

- [164] Yao, Q., Liu, J., Peng, Q., Wang, X., and Li, Y. *Chemistry – An Asian Journal* **1**(5), 737–741 (2006).
- [165] Shannon, R. *Acta Crystallographica Section A* **32**(5), 751–767 (1976).
- [166] Burns, A., Hayes, G., Li, W., Hirvonen, J., Demaree, J. D., and Shah, S. I. *Materials Science and Engineering: B* **111**(2–3), 150–155 (2004).
- [167] Bialkowski, S. E. *Photothermal Spectroscopy Methods for Chemical Analysis*. John Wiley & Sons, Hoboken, NJ, USA, (1996).
- [168] Wang, N., Jiang, W., Xu, X., Si, Z., Bai, H., and Tian, C. *Analytical sciences : the international journal of the Japan Society for Analytical Chemistry* **18**(5), 591–594 May (2002).
- [169] Huang, S. H. *Journal of the American Ceramic Society* **96**(10), 3108–3113 (2013).
- [170] Redmond, G., Fitzmaurice, D., and Graetzel, M. *The Journal of Physical Chemistry* **97**(27), 6951–6954 (1993).
- [171] Boschloo, G., , and Fitzmaurice, D. *The Journal of Physical Chemistry B* **103**(12), 2228–2231 (1999).
- [172] Domanski, K., Roose, B., Matsui, T., Saliba, M., Turren-Cruz, S.-H., Correa-Baena, J.-P., Carmona, C. R., Richardson, G., Foster, J. M., De Angelis, F., Ball, J. M., Petrozza, A., Mine, N., Nazeeruddin, M. K., Tress, W., Grätzel, M., Steiner, U., Hagfeldt, A., and Abate, A. *Energy Environ. Sci.* **9** (2017).
- [173] Cao, F., Oskam, G., Meyer, G. J., and Searson, P. C. *The Journal of Physical Chemistry* **100**(42), 17021–17027 (1996).
- [174] Abate, A., Paek, S., Giordano, F., Correa-Baena, J.-P., Saliba, M., Gao, P., Matsui, T., Ko, J., Zakeeruddin, S. M., Dahmen, K. H., Hagfeldt, A., Grätzel, M., and Nazeeruddin, M. K. *Energy Environ. Sci.* **8**, 2946–2953 (2015).
- [175] Kim, Y. H., Mueller-Meskamp, L., Zakhidov, A. A., Sachse, C., Meiss, J., Bikova, J., Cook, A., Zakhidov, A. A., and Leo, K. *Solar Energy Materials and Solar Cells* **96**(1), 244–250 (2012). Times Cited: 0.

References

- [176] Docampo, P., Tiwana, P., Sakai, N., Miura, H., Herz, L., Murakami, T., and Snaith, H. J. *The Journal of Physical Chemistry C* **116**(43), 22840–22846 (2012).
- [177] Lee, J.-W., Kim, D.-H., Kim, H.-S., Seo, S.-W., Cho, S. M., and Park, N.-G. *Advanced Energy Materials* **5**(20), 1501310 (2015). 1501310.
- [178] You, J., Meng, L., Song, T.-B., Guo, T.-F., Yang, Y. M., Chang, W.-H., Hong, Z., Chen, H., Zhou, H., Chen, Q., Liu, Y., De Marco, N., and Yang, Y. *Nat Nano* **11**(1), 75–81 (2016).
- [179] Chen, W., Wu, Y., Yue, Y., Liu, J., Zhang, W., Yang, X., Chen, H., Bi, E., Ashraful, I., Grätzel, M., and Han, L. *Science* **350**(6263), 944–948 (2015).
- [180] Seo, J.-Y., Matsui, T., Luo, J., Correa-Baena, J.-P., Giordano, F., Saliba, M., Schenk, K., Ummadisingu, A., Domanski, K., Hadadian, M., Hagfeldt, A., Zakeeruddin, S. M., Steiner, U., Grätzel, M., and Abate, A. *Advanced Energy Materials* **6**(20), 1600767 (2016).
- [181] Xu, L. and He, J. *ACS Applied Materials & Interfaces* **4**(6), 3293–3299 (2012).
- [182] Bao, X., Wang, Y., Zhu, Q., Wang, N., Zhu, D., Wang, J., Yang, A., and Yang, R. *Journal of Power Sources* **297**, 53 – 58 (2015).
- [183] Li, Y., Zhu, J., Huang, Y., Liu, F., Lv, M., Chen, S., Hu, L., Tang, J., Yao, J., and Dai, S. *RSC Adv.* **5**, 28424–28429 (2015).
- [184] Han, G. S., Chung, H. S., Kim, D. H., Kim, B. J., Lee, J.-W., Park, N.-G., Cho, I. S., Lee, J.-K., Lee, S., and Jung, H. S. *Nanoscale* **7**, 15284–15290 (2015).
- [185] Akkad, F. E. and Joseph, S. *Journal of Applied Physics* **112**(2) (2012).
- [186] Zhao, X., Shen, H., Zhang, Z., Li, X., Zhao, X., Tai, M., Li, J., Li, J., and Lin, H. *ACS Applied Materials & Interfaces* **8**(12), 7826–7833 (2016).
- [187] Basu, K., Benetti, D., Zhao, H., Jin, L., Vetrone, F., Vomiero, A., and Rosei, F. *Scientific Reports* **6**, 23312 (2016).
- [188] Chen, D., Zhang, C., Wang, Z., Zhang, J., Tang, S., Wei, W., Sun, L., and Hao, Y. *Applied Physics Letters* **104**(24) (2014).
- [189] Sidoti, D., Khurxhi, S., Kujofsa, T., Cheruku, S., Correa, J. P., Bertoli, B., Rago, P. B., Suarez, E. N., Jain, F. C., and Ayers, J. E. *Journal of Applied Physics* **109**(2) (2011).

References

- [190] Correa-Baena, J.-P., Kriz, D. A., Giotto, M., Suib, S. L., and Agrios, A. G. *RSC Adv.* **6**, 21326–21331 (2016).
- [191] Tiwana, P., Docampo, P., Johnston, M. B., Herz, L. M., and Snaith, H. J. *Energy Environ. Sci.* **5**, 9566–9573 (2012).
- [192] Yang, G., Lei, H., Tao, H., Zheng, X., Ma, J., Liu, Q., Ke, W., Chen, Z., Xiong, L., Qin, P., Chen, Z., Qin, M., Lu, X., Yan, Y., and Fang, G. *Small* (2016).
- [193] Bai, Y., Fang, Y., Deng, Y., Wang, Q., Zhao, J., Zheng, X., Zhang, Y., and Huang, J. *ChemSusChem* **9**(18), 2686–2691 (2016).
- [194] Park, M., Kim, J.-Y., Son, H. J., Lee, C.-H., Jang, S. S., and Ko, M. J. *Nano Energy* **26**, 208 – 215 (2016).
- [195] Giordano, F., Abate, A., Correa Baena, J. P., Saliba, M., Matsui, T., Im, S. H., Zakeeruddin, S. M., Nazeeruddin, M. K., Hagfeldt, A., and Graetzel, M. *Nature Communications* **7**, 10379 (2016).
- [196] Chandiran, A. K., Nazeeruddin, M. K., and Grätzel, M. *Advanced Functional Materials* **24**(11), 1615–1623 (2014).
- [197] Nie, W., Tsai, H., Asadpour, R., Blancon, J.-C., Neukirch, A. J., Gupta, G., Crochet, J. J., Chhowalla, M., Tretiak, S., Alam, M. A., Wang, H.-L., and Mohite, A. D. *Science* **347**(6221), 522–525 (2015).
- [198] Sessolo, M. and Bolink, H. J. *Science* **350**(6263), 917 (2015).
- [199] Pazos-Outon, L. M., Szumilo, M., Lamboll, R., Richter, J. M., Crespo-Quesada, M., Abdi-Jalebi, M., Beeson, H. J., Vrucinic, M., Alsari, M., Snaith, H. J., Ehrler, B., Friend, R. H., and Deschler, F. *Science* **351**(6280), 1430–1433 (2016).
- [200] McMeekin, D. P., Sadoughi, G., Rehman, W., Eperon, G. E., Saliba, M., Hörantner, M. T., Haghighirad, A., Sakai, N., Korte, L., Rech, B., Johnston, M. B., Herz, L. M., and Snaith, H. J. *Science* **351**(6269), 151–155 (2016).
- [201] Eperon, G. E., Leijtens, T., Bush, K. A., Prasanna, R., Green, T., Wang, J. T.-W., McMeekin, D. P., Volonakis, G., Milot, R. L., May, R., Palmstrom, A., Slotcavage, D. J.,

References

- Belisle, R. A., Patel, J. B., Parrott, E. S., Sutton, R. J., Ma, W., Moghadam, F., Conings, B., Babayigit, A., Boyen, H.-G., Bent, S., Giustino, F., Herz, L. M., Johnston, M. B., McGehee, M. D., and Snaith, H. J. *Science* (2016).
- [202] Park, N.-G., Grätzel, M., Miyasaka, T., Zhu, K., and Emery, K. *Nature Energy* **1**, 16152 (2016).
- [203] Noel, N. K., Habisreutinger, S. N., Wenger, B., Klug, M. T., Horantner, M. T., Johnston, M. B., Nicholas, R. J., Moore, D. T., and Snaith, H. J. *Energy Environ. Sci.* (2017).
- [204] Correa-Baena, J.-P., Anaya, M., Lozano, G., Tress, W., Domanski, K., Saliba, M., Matsui, T., Jacobsson, T. J., Calvo, M. E., Abate, A., Grätzel, M., Miguez, H., and Hagfeldt, A. *Adv. Mater.* **28**(25), 5031–5037 (2016).
- [205] Kim, M.-C., Kim, B. J., Son, D.-Y., Park, N.-G., Jung, H. S., and Choi, M. *Nano Letters* **16**(9), 5756–5763 (2016).
- [206] Song, J., Zheng, E., Bian, J., Wang, X.-F., Tian, W., Sanehira, Y., and Miyasaka, T. *J. Mater. Chem. A* **3**, 10837–10844 (2015).
- [207] deQuilettes, D. W., Zhang, W., Burlakov, V. M., Graham, D. J., Leijtens, T., Osherov, A., Bulovic, V., Snaith, H. J., Ginger, D. S., and Stranks, S. D. *Nature Communications* **7**, 11683 (2016).
- [208] Zhao, C., Chen, B., Qiao, X., Luan, L., Lu, K., and Hu, B. *Advanced Energy Materials* **5**(14), 1500279 (2015).
- [209] Sheikh, A. D., Bera, A., Haque, M. A., Rakhi, R. B., Gobbo, S. D., Alshareef, H. N., and Wu, T. *Solar Energy Materials and Solar Cells* **137**, 6–14 (2015).
- [210] Contreras, L., Idigoras, J., Todinova, A., Salado, M., Kazim, S., Ahmad, S., and Anta, J. A. *Phys. Chem. Chem. Phys.* **18**, 31033–31042 (2016).
- [211] Li, X., Bi, D., Yi, C., Décoppet, J.-D., Luo, J., Zakeeruddin, S. M., Hagfeldt, A., and Grätzel, M. *Science* (2016).
- [212] Leijtens, T., Eperon, G. E., Barker, A. J., Grancini, G., Zhang, W., Ball, J. M., Kandada, A. R. S., Snaith, H. J., and Petrozza, A. *Energy Environ. Sci.* **9**, 3472–3481 (2016).

References

- [213] Noel, N. K., Abate, A., Stranks, S. D., Parrott, E. S., Burlakov, V. M., G. A., and Snaith, H. J. *ACS Nano* **8**(10), 9815–9821 (2014).
- [214] de Quilletes, D. W., Vorpahl, S. M., Stranks, S. D., Nagaoka, H., Eperon, G. E., Ziffer, M. E., Snaith, H. J., and Ginger, D. S. *Science* **348**(6235), 683–686 (2015).
- [215] Pattabi, M., Suresh, N., Chaudhari, S., Banerjee, A., Phase, D., Gupta, A., and Rao, K. M. *Thin Solid Films* **322**(1-2), 340 – 343 (1998).
- [216] Paulson, G. and Friedberg, A. *Thin Solid Films* **5**(1), 47–52 (1970).
- [217] Goudy, A., Gee, M. L., Biggs, S., and Underwood, S. *Langmuir* **11**(11), 4454–4459 (1995).
- [218] German, R. *Sintering: From Empirical Observations to Scientific Principles*. Elsevier, (2014).
- [219] Liu, D., Wu, L., Li, C., Ren, S., Zhang, J., Li, W., and Feng, L. *ACS Applied Materials & Interfaces* (30), 16330–16337 (2015).
- [220] Liu, J., Gao, C., He, X., Ye, Q., Ouyang, L., Zhuang, D., Liao, C., Mei, J., and Lau, W. *ACS Applied Materials & Interfaces* **7**(43), 24008–24015 (2015).
- [221] Yang, M., Zhang, T., Schulz, P., Li, Z., Li, G., Kim, D. H., Guo, N., Berry, J. J., Zhu, K., and Zhao, Y. *Nature Communications* **7**, 12305 (2016).
- [222] Sheng, R., Wen, X., Huang, S., Hao, X., Chen, S., Jiang, Y., Deng, X., Green, M. A., and Ho-Baillie, A. W. Y. *Nanoscale* **8**, 1926–1931 (2016).
- [223] Jacobsson, T. J., Schwan, L. J., Ottosson, M., Hagfeldt, A., and Edvinsson, T. *Inorganic Chemistry* **54**(22), 10678–10685 (2015).
- [224] Cao, D. H., Stoumpos, C. C., Malliakas, C. D., Katz, M. J., Farha, O. K., Hupp, J. T., and Kanatzidis, M. G. *APL Mater.* **2**(9) (2014).
- [225] Kavan, L., Steier, L., and Grätzel, M. *The Journal of Physical Chemistry C* **121**(1), 342–350 (2017).

12 Curriculum Vitae

Contact information

E-mail: bart.roose@unifr.ch, bardtroose@gmail.com

Website: www.researchgate.net/profile/Bart_Roose

Personal details

Date of Birth: November 24, 1988

Place of Birth: Terneuzen (The Netherlands)

Citizenship: Dutch

Education and positions

2014-2017: PhD Student, Soft Matter Physics, Adolphe Merkle Institute, University of Fribourg

2013-2014: Research Assistant, Thin Films and Interfaces, University of Cambridge

2010-2013: Msc. Chemistry, Radboud University Nijmegen

2007-2010: Bsc. Chemistry, Radboud University Nijmegen

Supervision experience

2016: Christian Johansen, NCCR Summer Internship

Conferences

Challenges in Chemical Renewable Energy (ISACS12), Cambridge, 2013

Solution Processed Semiconductor Solar Cells Conference (SSSC14), Oxford, 2014

Hybrid and Organic Photovoltaics (HOPV15), Rome, 2015

Perovskite Solar Cells and Optoelectronics (PSCO15), Lausanne, 2015

Perovskite Solar Cells and Optoelectronics (PSCO16), Genoa, 2016

13 Related Publications

B. Roose, C. M. Johansen, T. Jaouen, P. Aebi, U. Steiner, A. Abate: *Highly efficient m-SnO₂ perovskite solar cells through Ga-doping*, in preparation

B. Roose, A. Ummadisingu, J. P. Correa-Baena, M. Saliba, A. Hagfeldt, M. Grätzel, U. Steiner, A. Abate: *Coalescence in perovskite crystals and effects on photovoltaic performance*, submitted

J. Brauer, S. Sanchez, D. Tsokkou, B. Roose, F. De Angelis, U. Steiner, A. Abate, N. Banerji: *Better than the sum of its parts: Origin of the superior photovoltaic performance of mixed halide/mixed cation perovskites*, submitted

A. Abate, R. Dehmel, A. Sepe, N. L. Nguyen, B. Roose, N. Marzari, J. Hong, J. Hook, U. Steiner, C. Neto: *Halogen-Bond Driven Self-Assembly of Perfluorocarbon Monolayers*, submitted

J.-P. Correa-Baena, W. Tress, K. Domanski, E. Halvani, S. Turren, B. Roose, P. P. Boix, M. Grätzel, M. Saliba, A. Abate, A. Hagfeldt: *Identifying and suppressing interfacial recombination in highly efficient perovskite solar cells*, Energy Environ. Sci., **2017**

R. Grisorio, B. Roose, G. P. Suranna, A. Abate: *Molecular Tailoring of Phenothiazine-Based Hole-Transporting Materials for Highly Performing Perovskite Solar Cells*, ACS Energy Lett., **2017**, *2*, 1029

G. Nasti, S. Sanchez Alonso, I. Gunkel, S. Balog, B. Roose, J. Teuscher, G. Gentile, P. Ceruti, V. Ambrogi, C. Carfagna, U. Steiner, A. Abate: *Patterning of perovskite-polymer films by wrinkling instabilities*, Soft Matter, **2017**, *13*, 1654

K. C. Gödel, B. Roose, A. Sadhanala, Y. Vaynzof, S. Pathak, U. Steiner: *Partial oxidation of the absorber layer reduces charge carrier recombination in antimony sulfide solar cells*, Physical Chemistry Chemical Physics, **2017**, *19*, 1425-1430

K. Domanski, B. Roose, T. Matsui, M. Saliba, S.-H. Turren-Cruz, J.-P. Correa-Baena, C. Roldan Carmona, G. Richardson, J. Foster, F. De Angelis, J. Ball, A. Petrozza, N. Mine, M. K. Nazeeruddin, W. Tress, M. Grätzel, U. Steiner, A. Hagfeldt, A. Abate: *Migration of cations induces reversible performance losses over day/night cycling in perovskite solar cells*, Energy & Environmental Science **2017**, *9*

B. Roose, J. P. Correa-Baena, K. C. Gödel, M. Grätzel, A. Hagfeldt, U. Steiner, A. Abate: *Mesoporous SnO₂ electron selective contact enables UV-stable perovskite solar cells*, Nano Energy, **2016**, *30*, 517-522

B. Roose, K. C. Gödel, S. Pathak, A. Sadhanala, J. P. Correa-Baena, B. D. Wilts, H. J. Snaith, U. Wiesner, M. Grätzel, U. Steiner, A. Abate: *Enhanced Efficiency and Stability of Perovskite Solar Cells Through Nd-Doping of Mesostructured TiO₂*, Advanced Energy Materials, **2016**, *6*, 1501868.

M. Anaya, J. P. Correa-Baena, G. Lozano, M. Saliba, P. Anguita, B. Roose, A. Abate, U. Steiner, M. Grätzel, M. E. Calvo, A. Hagfeldt, H. Miguez: *Optical analysis of CH₃NH₃Sn_xPb_{1-x}I₃ absorbers: a roadmap for perovskite-on-perovskite tandem solar cells*, Journal of Materials Chemistry A, **2016**, *4*, 11214-11221

B. Roose, S. Pathak, U. Steiner: *Doping of TiO₂ for Sensitized Solar Cells*, Chemical Society Reviews, **2015**, *44*, 8326-8349

K. C. Gödel, Y. C. Choi, B. Roose, A. Sadhanala, H. J. Snaith, S. I. Seok, U. Steiner, S. K. Pathak: *Efficient room temperature aqueous Sb₂S₃ synthesis for inorganic-organic sensitized solar cells with 5.1% efficiencies*, Chemical Communications, **2015**, *51*, 8640-8643

S. K. Pathak, A. Abate, P. Ruckdeschel, B. Roose, K. C. Gödel, Y. Vaynzof, A. Santhala, S.-I. Watanabe, D. J. Hollman, N. Noel, A. Sepe, U. Wiesner, R. Friend, H. J. Snaith, U. Steiner: *Performance and Stability Enhancement of Dye-Sensitized and Perovskite Solar Cells by Al Doping of TiO₂*, Advanced Functional Materials, **2014**, *24*, 6046-6055

